

2019-07-10

Enhancing Tribological Properties of Metallic Sliding Surfaces through Micro Multi-texturing Techniques

Reséndiz-Pérez, Jaime De Jesús

Reséndiz-Pérez, J. D. J. (2019). Enhancing Tribological Properties of Metallic Sliding Surfaces through Micro Multi-texturing Techniques (Doctoral thesis, University of Calgary, Calgary, Canada). Retrieved from <https://prism.ucalgary.ca>.

<http://hdl.handle.net/1880/110625>

Downloaded from PRISM Repository, University of Calgary

UNIVERSITY OF CALGARY

Enhancing Tribological Properties of Metallic Sliding Surfaces through Micro
Multi-texturing Techniques

by

Jaime de Jesús Reséndiz Pérez

A THESIS

SUBMITTED TO THE FACULTY OF GRADUATE STUDIES

IN PARTIAL FULFILMENT OF THE REQUIREMENTS FOR THE

DEGREE OF DOCTOR OF PHILOSOPHY

GRADUATE PROGRAM IN MECHANICAL AND MANUFACTURING ENGINEERING

CALGARY, ALBERTA

JULY, 2019

© Jaime de Jesús Reséndiz Pérez 2019

ABSTRACT

Friction reduction is important for minimizing energy loss and improving the life of sliding components. Surface texturing is considered an effective way to control the wear and friction on these components. In this research, textured surfaces were created on aluminium workpieces using the tilted micro end milling technique. A flat end mill was used to generate asymmetric dimples. A different series of symmetric dimpled surfaces were also machined using a single crystal diamond cutter. Cutting forces were modelled and compared with the experimental results. On the symmetric dimpled surface, a multi-scale texture process was carried out on the dimples to create a smaller scale roughness through a High-Velocity Abrasive Machining process. A reciprocating tribometer, based on a piezoelectric table dynamometer and a hemispherical ruby counter surface, was used to evaluate friction coefficients under both dry and lubricated sliding conditions. Asymmetric dimples exhibited directional friction effects. For multi-scale textured surfaces, it has been observed a greater reduction in the friction coefficient under lubricated conditions when compared with symmetrical dimples. To gain insight into the mechanism of friction reduction for these surfaces, a series of 2D simulations were performed. These simulations showed that the mechanism of friction reduction is attributed to the ability of dimples to increase the pressure of the lubricant in the contact region resulting from the fluid flow between the sliding surfaces. Moreover, a substantial decrease in the depth of the dimples on worn surfaces was observed, suggesting that entrapment of wear particles within the surface texture features may also influence the measured friction coefficient. Analysis of the wear track depth showed that surface texturing also has a beneficial influence on the calculated Archard wear coefficient.

ACKNOWLEDGEMENTS

This work would not have been possible without the guidance of both Dr. Simon Park and Dr. Philip Egberts, who have been supportive in this research. I would like to thank the supervisory committee members, Dr. Alejandro Ramirez-Serrano and Dr. Frank Cheng, internal examiner, Dr. Nashaat Nassar, and external examiner, Dr. Alison C. Dunn from the University of Illinois at Urbana-Champaign for taking the time to review this thesis.

I would like to acknowledge to Consejo Nacional de Ciencia y Tecnologia (CONACYT) México, and the Natural Sciences and Engineering Research Council (NSERC) of Canada for providing funds to support the study. I would like to express my gratitude to my colleagues at the Micro Engineering Dynamics and Automation Lab (MEDAL) for their assistance and friendship.

My deepest gratitude to my beloved parents for all their unconditional love and support.

I would like to show my sincere acknowledge to Victoria and Isaac and mention that I have missed both of you so much during all this time.

To God, who gave me the patience and knowledge to successfully finish this journey.

Success derives from failure, failure derives from initial attempt.

3.1.3	Flat End Mills	52
3.1.4	Single Crystal Diamond Cutter	53
3.2	Dimple Cutting Force Model.....	55
3.2.1	Modeling of Cutting Dimple Forces	55
3.3	Cutting Forces Simulation vs. Measured Cutting Forces	60
3.4	Profile of Dimpled Surfaces Produced with Flat end Mill	63
3.5	Profile of Dimpled Surfaces Produced with Single Crystal Diamond Cutter ..	64
3.6	Profile of Multi-scaled Textured Dimpled Surfaces through a High-Velocity Abrasive Machining Process	66
3.7	Summary.....	68
CHAPTER 4. HIGH VELOCITY ABRASIVE MACHINING		70
4.1	Wetting Effects on Multi-textured Surfaces.....	70
4.2	Roughness Effects on Hydrophobic and Hydrophilic Surfaces	71
4.3	Creation of multi-textured surfaces	73
4.4	Contact Angle (CA) and Contact Angle Hysteresis (CAH).....	78
4.5	Erosion Rate	82
4.6	Summary.....	84
CHAPTER 5. TRIBOLOGICAL MODELLING		85
5.1	Theoretical	85
5.2	Two-dimensional results	89
5.3	Summary.....	98

CHAPTER 6. TRIBOLOGICAL TESTING AND ANALYSIS OF TEXTURED SURFACES.....	99
6.1 Contact Mechanics on Textured Surfaces	100
6.2 Tribological Mechanics and Experimental Setup.....	103
6.3 Symmetrical Dimpled Surfaces	106
6.3.1 Effects of Roughness.....	114
6.4 Asymmetrical Dimpled Surfaces.....	115
6.5 Wear Analysis	117
6.6 Summary.....	120
CHAPTER 7. CONCLUSIONS.....	121
7.1 Summary of the Research.....	121
7.2 Limitations and Assumptions	124
7.3 Future Work.....	128
REFERENCES.....	130
LIST OF PUBLICATIONS	143

LIST OF FIGURES

Figure 2.1. <i>Representation of a typical Stribeck curve (Mansot et al. 2009).</i>	21
Figure 2.2. <i>Schematic representation of contact asperities between two plane surfaces at microscale level.</i>	24
Figure 2.3. <i>The principle of plasma assisted electron beam evaporation (Bewilogua et al. 2009).</i>	32
Figure 2.4. <i>Arrangement used in the excimer laser ablation study (Prina Mello, Bari, and Prendergast 2002).</i>	37
Figure 2.5. <i>Lithography process: six-phase scheme (Prina Mello, Bari, and Prendergast 2002).</i>	39
Figure 2.6. <i>Appearance of micro-dimples produced by AJM and LBM, both of which exhibited characteristic profiles (Wakuda et al. 2003).</i>	43
Figure 3.1. <i>Dimpled surface schematic drawing.</i>	49
Figure 3.2. <i>Schematic of the machining system used.</i>	51
Figure 3.3. <i>Picture of Flat End Mill.</i>	53
Figure 3.4. <i>Picture of Single Crystal Diamond cutter.</i>	54
Figure 3.5. <i>Analytic model of a flat end mill.</i>	57
Figure 3.6. <i>Machining forces resolved in the (a) x-, (b) y- and (c) z-axes for inclined flat end milling of the Al6061 workpiece.</i>	60
Figure 3.7. <i>Machining forces in the (a) x-, (b) y- and (c) z-axes for a single crystal diamond cutter of the Al6061 workpiece.</i>	62
Figure 3.8. <i>Three-dimensional topographic image of the dimpled surfaces produced on the AL6061 workpiece using a flat end milling.</i>	63

Figure 3.9. <i>Three-dimensional topographic image of the dimpled surfaces produced on the AL6061 workpiece using a single diamond cutter.</i>	65
Figure 3.10. <i>Plan view optical microscopy image of the dimpled surface.</i>	67
Figure 3.11. <i>Plan view optical microscopy image of the dimpled surface after shot blasting.</i>	68
Figure 4.1. <i>Schematic representation of roughness profiles for skewness (R_{sk}) and kurtosis (R_{ku}) (Gadelmawla et al. 2002).</i>	72
Figure 4.2. <i>Schematic of the shot blasting process.</i>	74
Figure 4.3. <i>Microscopic picture of the micro abrasive powder.</i>	75
Figure 4.4. <i>Optical profilometry of textured surfaces showing their R_{sk} and R_{ku}.</i>	77
Figure 4.5. <i>Contact angle of a blasted flat surface using different grain sizes, angle nozzle inclinations and blasting time.</i>	79
Figure 4.6. <i>Schematic of the calculation of contact angle hysteresis.</i>	80
Figure 4.7. <i>Contact angle acquired with a SmartDrop device.</i>	81
Figure 4.8. <i>Erosion rate of Aluminium 6061-T6 by 50 μm and 10 μm aluminium oxide micro particles.</i>	83
Figure 5.1. <i>Tribosystem for the mathematical model proposed for Profito et al. (Profito, Zachariadis, and Tomanik 2011).</i>	87
Figure 5.2. <i>A schematic of the tribological simulation.</i>	900
Figure 5.3. <i>Dimples profiles and hydrodynamic pressures.</i>	92
Figure 5.4. <i>Profiles of the surfaces used during simulations.</i>	933
Figure 5.5. <i>Hydrodynamic pressure profile determined from VTL simulations.</i>	94
Figure 5.6. <i>Measured hydrodynamic area under the curve for (a) a shot blasted flat surface, (b) a dimple surface, and (c) a shot blasted dimple surface.</i>	95

Figure 5.7. <i>Effect of erosion on a multi texture dimple.....</i>	96
Figure 5.8. <i>Stribeck curve determined from VTL simulations.</i>	97
Figure 6.1. <i>Schematic of contact between the ruby sphere and the workpiece.....</i>	100
Figure 6.2. <i>Photograph of friction measurement apparatus / tribometer.....</i>	104
Figure 6.3. <i>Measured friction coefficient versus cycle number for a flat, oil-lubricated surface...</i>	106
Figure 6.4. <i>Schematic of the tilted spindle technique.</i>	107
Figure 6.5. <i>Measured friction coefficient versus cycle number.</i>	108
Figure 6.6. <i>Simulated hydrodynamic pressure and friction force over a symmetrical dimple...109</i>	
Figure 6.7. <i>Stribeck curve of a flat and textured surfaces.</i>	110
Figure 6.8. <i>Stribeck curve comparing acquired experimental data and simulated results of flat and textured surface.....</i>	112
Figure 6.9. <i>Simulated Stribeck curve for a flat surface, and different shot blasted surfaces, under lubricated sliding conditions.....</i>	114
Figure 6.10. <i>Average friction coefficient versus normal load measured for flat and dimpled surface under lubricated and unlubricated sliding conditions..</i>	116
Figure 6.11. <i>Friction coefficient measured during reciprocating motion for a lubricated flat surface, and a lubricated dimpled surface.....</i>	116
Figure 6.12. <i>Optical images of the worn surface on flat surface, a dimpled surface, and a shot blasted dimpled surface after a tribological test.</i>	118
Figure 6.13. <i>Comparison of average wear versus applied load for the flat surface, sandblasted flat surface, dimple surface, and sandblasted dimple surface).....</i>	119

LIST OF TABLES

Table 3.1. <i>Machining parameters used to create dimples.</i>	61
Table 4.1. <i>HVAM texturing parameters used in this research.</i>	74
Table 6.1. <i>Hertz contact mechanics to estimate the maximum pressure.</i>	102
Table 6.2. <i>Results of the determination of the contact pressures using Hertzian analysis.</i>	102
Table 6.3. <i>Maximum values of film thickness.</i>	113

LIST OF SYMBOLS AND ABBREVIATIONS

AJM	Abrasive Jet Machining
CA	Contact Angle
CAH	Contact Angle Hysteresis
CFD	Computational Fluids Dynamics
CNC	Computer Numerical Control
cSt	Centistokes
DMT	Derjagui, Muller and Toporov contact theory
EHL	Elastohydrodynamic lubrication
FDS	Finite Difference Scheme
HSS	High Speed Steel
HVAM	High Velocity Abrasive Machining
JKR	Johnson, Kendall and Roberts contact theory
LBM	Laser Beam Machining
LST	Laser Surface Texturing
MEMS	Micro-electrical mechanical systems
SOR	Successive Over-Relaxation
UV	Ultra Violet light
VTL	Virtual Tribology Laboratory

a	Contact radius	μm
A_d	Dimple area	mm^2
A_w	Total workpiece area	mm^2
D	Density of dimples	$dimples/mm^2$
d	Cutting depth	μm
d_r	Spacing between rows of dimples	μm
E'	Effective Young's modulus	Pa
E	Elastic modulus	Pa
E^*	Reduced Young's modulus	Pa
f	feed rate	mm
F_a	Axial cutting force	N
F_n	Applied load	N
F_r	Radial cutting force	N
f_t	Feed rate	$mm/flute$
F_t	Tangential cutting force	N
F_x	Cutting force in x axis	N
F_y	Cutting force in y axis	N

F_z	Cutting force in z axis	N
h	Film thickness	μm
H	Material hardness	Pa
h_c	Chip thickness	mm
h_d	Deflection of the flat surface	μm
h_{min}	Minimum oil film thickness	μm
k	Wear coefficient	$\mu m^3/Nm$
l	Sliding distance	mm
n	Spindle speed	RPM
N	Number of flutes in the micro tool	$\#$
η	Lubricant viscosity	cSt
n^*	Dynamic lubricant viscosity	cSt
P_{ASP}	Asperity pressure	Pa
P_H		Pa
P_{max}	Maximum Hertzian contact pressure	Pa
R	Micro-tool radius	μm
R_f	Roughness factor	<i>dimensionless</i>
s_d	Spacing between adjacent dimples	μm
U	Rolling velocity	mm/s
V	Speed	mm/s
ν	Poisson's ratio	<i>dimensionless</i>
x_{pitch}	Linear dimple pitch in the feed direction	<i>dimples/mm</i>
ϕ	Micro-tool rotation angle	$^\circ$
θ	Static contact angle for a rough surface	$^\circ$
θ_{adv}	Advancing contact angle	$^\circ$
θ_{rec}	Advancing contact angle	$^\circ$
μ	Friction coefficient	<i>dimensionless</i>
ρ	Pressure	Pa
τ	Shear stress	Pa
γ	Micro-tool inclination angle	$^\circ$

CHAPTER 1. INTRODUCTION

Friction is present in all sliding surfaces; in some cases, such as in brakes, tires, or shoes, friction has a positive effect. On the other hand, friction can be an undesirable effect because it produces wear - reducing the life of mechanical components - and consumes energy. Friction reduction is imperative for the longevity of components. For this reason, many moving contacts are lubricated for the sake of reducing friction and wear, resulting in energy efficiency and component durability. According to Nakada (Nakada 1994), in an internal combustion engine, about 40% of the total energy loss is due to friction, while Priest *et al.*, (Priest and Taylor 2000) mentioned that a 10% reduction in mechanical loss would lead a 1.5% reduction in fuel consumption. Energy is a key resource for our society today and will be crucial for our sustainability in the future. A considerable amount of energy is consumed to overcome friction, especially in the transportation, industrial, and power generation sectors, and major economic losses are also due to wear of products and components and their replacement. One-fifth of all energy produced worldwide is used to overcome friction, about 100 million terajoules a year (Holmberg and Erdemir 2015). The largest quantities of energy are used by industry (29 %) and transportation (27 %), and according to recent studies, it is possible to save as much as 17.5% of the energy used in road transports in the short term (5 – 9 years) by effective implementation of new tribological solutions (Holmberg and Erdemir 2015).

For this reason, researchers and industries have been investigating different solutions to reduce friction: development of better lubricants, improvement of low friction materials, hard coatings, and development of optimal engineering surfaces by creating microtextures. The last

method is also called surface patterning or surface texturing, and it has gained significance due to modern micromachining techniques. Gropper *et al.*, (Gropper, Wang, and Harvey 2016) defined surface texturing as the intentional introduction of well-defined identical features on surfaces (dimples or grooves), which act as lubricant reservoirs, providing lubricant to the contact in cases of starved lubrication, and capture wear debris, thereby minimizing third-body abrasion. Thus, surface engineering is considered an effective way to reduce friction and wear. In this way, Ryk *et al.* (Ryk and Etsion 2006) reported that under certain conditions, micro dimples fabricated onto the face of piston rings can result in up to a 25% friction reduction with lubricant. However, Costa *et al.*, (H. Costa and Hutchings 2015) mentioned that the effectivity of surface texturing can change between different applications or conditions, such as: dry sliding, solid lubrication, and oil lubrication. However, a negative effect of the dimples was an increase in the contact pressure between the sliding components due to the decrease of the area of contact. Thus, a micro dimple density of 15% to 30% was recommended (Uehara et al. 2004).

Lubrication is essential to reduce friction, and it consists of four different regimes (Hydrodynamic, Elastohydrodynamic, Mixed, and Boundary). Hydrodynamic lubrication consists of two surfaces that are fully separated by a fluid film, thus lowering the friction between surfaces; this results in higher efficiency and improves the longevity of mechanical components. In Elastohydrodynamic lubrication (EHL) the hydrodynamic film formation is enhanced by surface elastic deformation and by the increase of lubricant viscosity due to high pressure. In mixed lubrication, two surfaces are partially separated by a film, but contact between protruding asperities can occur. The final regime is boundary lubrication, in which two surfaces are in contact with each other. This increases the friction and reduces the life of the components. Friction in these regimes

depends on many factors, such as : the speed that one component moves compared to the other, the applied load, deflections on the surfaces, and surface topography.

According to Coblas *et al.* (Coblas et al. 2014), the lubrication regime plays an imperative role in helping textured surfaces accomplish three fundamental roles: lubricant reservoir, micro hydrodynamic bearing and as debris trap especially in dry conditions and in the boundary region, helping to decrease wear, increasing components life and improving fretting fatigue resistance (Borghini et al. 2008; Dumitru et al. 2003). The parameters that affect fretting fatigue are the contact pressure, slip amplitude, and frictional forces at the contact interface. With a given pressure applied to the surfaces, the real area of contact is constant (Waterhouse and Trowsdale 1992). With a smooth surface, the real area tends to be large, whereas with a textured surface the real area is divided up into many small areas (Nowell and Hills 1990).

In the cases of the boundary and the mixed lubrication regimes , surface textures can act like micro-reservoirs and thus provide lubricant during the operating period (Pawlus et al. 2009; Pettersson and Jacobson 2003; Vilhena et al. 2009). When acting as micro hydrodynamic bearings, textured surfaces can create an extra level of hydrodynamic pressure in addition to the pressure generated by surface roughness, waviness, eccentric rotation, or squeeze.

In this study, specific dimple size and low oil viscosity were used to generate a micro-hydrodynamic lift, as indicated by Braun *et al.*, (Braun et al. 2014). This hydrodynamic lubrication consisted of the addition of fluid at the contact interface of the surfaces. The presence of this fluid aided the relative movement of the surfaces by creating a pressure field that balanced the external loads, thus forming a lubricating film.

Several techniques to create micro dimples have been studied and applied by many researchers. Among the various manufacturing techniques, the Micro-Milling Tilted Spindle technique offered excellent characteristics for machining micro dimples (fast processing time, clean to the environment, no need of a vacuum, good and easy control of the shape and size of the micro-textures), and thus it was used to pattern aluminium surfaces into regular arrays of micro dimples. In addition, an extra texturing level to reduce friction and wear could be added by a High-Velocity Abrasive Machining Process, which results in multitextured surfaces.

A series of experiments were performed using a reciprocating sliding tribometer to measure the average coefficient of friction and wear on textured surfaces. The effect of directional friction under lubricated and dry conditions on asymmetrical dimples was studied, showing that asymmetrically shaped dimples have a sliding direction dependent response (in terms of the measured friction forces and friction coefficient) in comparison with flat surfaces.

Regarding the multi-texture scale dimples, the combined influence of shot blasting and dimple surface textures had a synergistic influence on the friction coefficient, suggesting that the surface roughness of surfaces is a mechanism to further improve the friction and wear performance of textured surfaces. However, abrasive particles can cause a negative effect on the textured surface. Thus, the erosion effects caused by different particle sizes and exposure time on textured surfaces must be studied.

1.1 Objectives

1.1.1 Fabrication of Multi Scaled Dimple Surfaces

The main objective was to determine the tribological benefits of both dry and lubricated sliding textured surfaces through multi-scaled dimples, in regard to friction and wear reduction.

To accomplish this objective, an innovative technique consisting of inclined micro-milling combined with a high-velocity abrasive machining process was used. This technique allowed rapid fabrication of textured surfaces by creating rows of dimples through a fast translation of the workpiece with a high material removal rate, producing a variety of textures with only slight changes to the cutting micro tool geometry (Fleischer and Kotschenreuther 2006; J. Yan et al. 2010).

Micro-Milling Tilted Spindle offered several advantages when compared with other texturing techniques. For example, special facilities having complex systems were not necessary; neither was a chemical mask. Also, different workpiece materials could be used. However, special attention needed to be taken when machining using micro tools, because important features of machined dimples (such as: shape, size, density, and depth) can be affected by factors like: oscillations of cutters while rotating, cutting tool wear or breakage, tool deflections, non-uniformity of cutting conditions, a varying rigidity of the workpiece or clamping system, side pileups, and abrupt movements of the workpiece while texturing. To detect and reduce these disadvantages, predictive modelling of the machining forces will be completed.

In addition, a second layer of textured roughness was added to symmetric dimpled surfaces to mimic hydrophobic surfaces present in nature (such as a lotus leaf), in order to increment the contact angle between the surface and the liquid. The desired result was to enhance the lubrication and thus decrease the friction between the sliding surfaces. A series of simulations together with experimental tests were conducted to acquire the friction coefficient values and Stribeck curves of the multi-textured surfaces. After this, interferometry was used to characterize the multi-textured surfaces and determine the wear through the Archard's equation.

1.1.2 Tribological Modeling of Dimpled Surfaces and Tribological Tests

After machining multi-scaled dimpled surfaces, 2-D numerical simulations were used in order to determine the texturing parameters that significantly contributed to the frictional forces, and eventually, the friction coefficient. To accomplish this objective, the Virtual Tribology Laboratory (VTL) software was used. First, analytical equations were used to show that there was a certain real area of contact at which the friction force acts. Then, the one-dimensional transient Reynolds equation and factors such as the hydrodynamic pressure, the lubricant dynamic viscosity, the slide velocity, and the minimum oil film thickness were considered.

Simulations were performed, replicating the sliding experimental conditions and considering the final textured surface of the workpiece. To summarize the results obtained for the various applied loads and speeds on the different surfaces, several Stribeck curves were created, showing the changes of the friction coefficient. The obtained results through simulation were compared with the experimental results generated via tribological tests. Finally, microscopic pictures of the tested samples were taken to measure the loss of volume and quantify the reduction of wear suffered on the textured surfaces compared with a flat surface using the Archard's wear equation.

1.2 Thesis Organization

Chapter 2 presents an overview of existing knowledge regarding tribology, lubrication regimes, contact mechanics, modelling techniques of textured surfaces, machining textured surfaces, friction reduction on textured surfaces, machining forces modelling, and erosion. In Chapter 3, the micro machining technique is presented. In addition, a dimple cutting force model is developed to predict issues such as uniform cutting, oscillations in the cutter, or tool wear. Model

and experimental results using a carbide tool having two flutes and a single diamond cutter are also compared in this section. A dimple profile shape comparison is shown, as well. The experimental setup to create shot blasted surfaces and the wetting implication of roughness on surfaces are discussed in Chapter 4. Chapter 5 deals with the tribological modelling and analytical results on different textured surfaces. Chapter 6 shows the tribological analysis of run experiments on the textured surfaces. In Chapter 7, conclusions and recommendations are given.

CHAPTER 2. LITERATURE SURVEY

Understanding the frictional behaviour of micro textured sliding surfaces is based on the fundamental knowledge of previous studies on untextured sliding surfaces done by Richard Stribeck (Stribeck 1902). In this chapter, literature forming the fundamental basis of studies proposed in this study is introduced.

Functional micropatterned surfaces have been recognized for their vital roles in a wide range of advanced applications. Surface textures are commonly used in micro-electrical mechanical systems (MEMS), magnetic hard discs, machining tools and automotive components in order to decrease friction by decreasing the contact area and storing oil (Wakuda et al. 2003). In addition, wear debris generated during the friction in sliding components can become embedded between two surfaces, forming a wedge to scratch the surface and increasing friction (Dubrujeaud, Vardavoulias, and Jeandin 1994). Micro dimples can trap those debris, reducing the chance of wedge formation and thus decreasing the wear rate between sliding surfaces (Galda, Pawlus, and Sep 2009).

2.1 Textured Surfaces

It has been found that surface texturing has great a potential for improving the tribological performance in terms of reducing the wear and friction on sliding surfaces (Kovalchenko et al. 2005a; Meng et al. 2010; H. L. Costa and Hutchings 2007; Tang et al. 2013). Also, the tribological effectiveness of the textured surface can be influenced by a combination of different texture parameters, such as: size, density, depth, micro texture shape, and orientation of the dimples. It is important to consider that depending on the machining parameters, dimples can have positive or

negative effects on friction (Uehara et al. 2004). Effects can include increasing wear of the texture surfaces (Ramesh et al. 2013; Qiu and Khonsari 2011), increasing friction (Pettersson and Jacobson 2003; Vilhena et al. 2009; Parreira, Gallo, and Costa 2012), and a leak of lubricant supply caused by excessive depth of dimples, leading to a higher friction coefficient compared with an untextured surface Ryk *et al.* (Ryk, Kligerman, and Etsion 2002).

Thus, the effectiveness of textured surfaces depends largely on the size and density of micro dimples, but a thin film of oil is also necessary. As dimples act as oil reservoirs, the oil inside them counteracts the effect of increasing the contact pressure. Hence, using an oil with lower viscosity is beneficial for the system (Lu and Khonsari 2007).

2.2 Fundamentals of Tribology

In tribology, speed-dependent film formation and changes in the frictional properties are portrayed through a Stribeck curve. The Stribeck curve is a non-linear function between the friction coefficient of the contact load (F_n), the lubricant viscosity (η) and the lubricant entrainment speed (V), which define the Hersey number. Depending on the type of intervening film and its thickness, it is possible to get different regimes of lubrication. Figure 2.1 presents a schematic of such a curve as an overall view of friction variation in the entire range of lubrication as a function of the Hersey number. The four lubrication regimes (hydrodynamic, elastohydrodynamic, mixed, and boundary) can be clearly presented in the Stribeck curve. The solid line shows how the friction coefficient varies with sliding velocity, lubricant viscosity, and applied load, while the dotted line shows the variation of the lubricant thickness with those three variables. The lubrication regimes are indicated on the graph, with their boundaries marked by vertical lines.

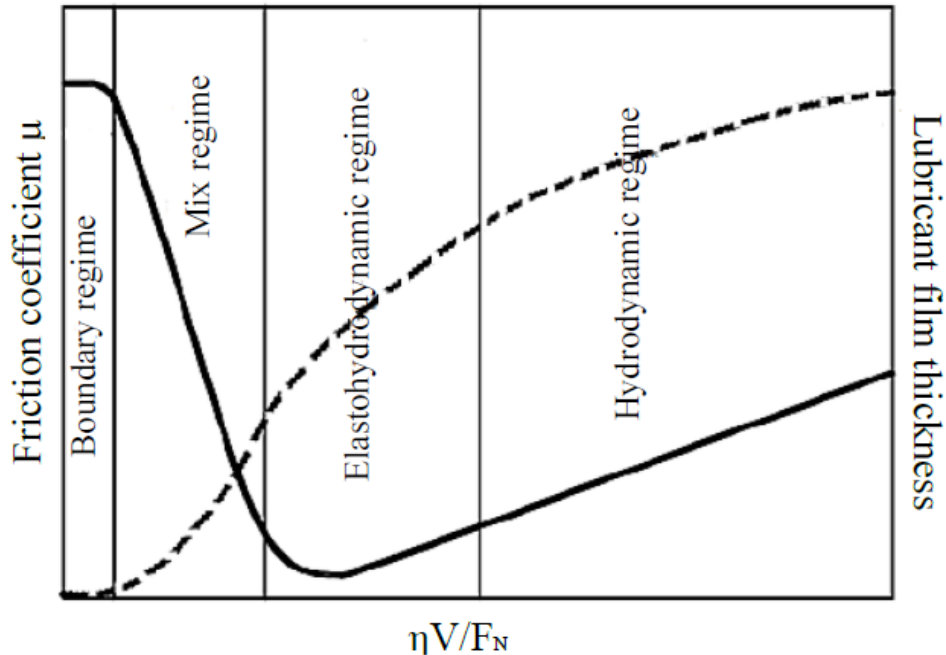


Figure 2.1. Representation of a typical Stribeck curve (Mansot et al. 2009).

The boundary lubrication regime is present at low speeds and high applied loads. In this condition the fluid film is negligible and direct contact will occur between the surface asperities. High friction coefficients and high wear rates will then prevail unless the surfaces are protected by a suitable lubricant. The mixed lubrication regime deals with conditions like low speed, high load, or temperatures sufficiently large enough to significantly reduce lubricant viscosity. When any of these conditions occur, the tallest asperities of the bounding surfaces will protrude through the film and occasionally come in contact. Hydrodynamic or full film lubrication is for when the load carrying surfaces are separated by a relatively thick film of lubricant. This is a stable regime of lubrication, and metal-to-metal contact does not occur during the steady state operation of the bearing. The lubricant pressure is self-generated by the moving surfaces drawing the lubricant into the wedge formed by the bonding surfaces at a high enough velocity to generate the pressure to completely separate the surfaces and support the applied load.

The concept of lubrication regimes shown in a Stribeck curve is often applied for the study of frictional characteristics of materials in rubbing and the understanding of a tribological process. Variations of the Hersey number in a wide range offers a broad view of the tribological interface under investigation. Consequently, The Stribeck curve is an effective way to summarize the transition from elasto-hydrodynamic to hydrodynamic to mixed and boundary lubrication regimes. Therefore, researchers use the Stribeck curve to predict and analyze the regime transition at which a particular contact operates (Gelinck and Schipper 2000). For example, in Galda's work (Galda, Pawlus, and Sep 2009), researchers studied the influence of geometrical characteristics of the surface texture on the Stribeck curve in lubricating sliding surfaces, and concluded that with the proper configuration of shape, dimensions, and area density of oil pockets, the friction coefficient of the sliding pairs decreased by about 15% in comparison to non-textured surfaces; a similar result was achieved by Lu *et al.* (Lu and Khonsari 2007). By means of Stribeck curves, Braun *et al.* (Braun et al. 2014) found that for the 40 μm diameter dimples at 500 mm/s sliding speed a friction reduction of up to 80% was possible. To achieve this, an oil flow inside the dimples was established, in order to generate a micro-hydrodynamic lift. If the dimples diameter increased, the oil viscosity must increase too.

In addition, oils and additives used to lubricate machinery may have many different purposes, such as reducing friction and avoiding the excessive wear from dry surfaces rubbing together (Lim and Ashby 1987). Reducing the friction between the moving parts directly results in lower wear and thus, a decrease in energy and operating costs. Machine element geometry also plays an important role in lubrication. For example, journal bearings under the same average pressure but having different bearing structures and supports may experience different surface deformation and wear, which in turn affects the lubricant film thickness and friction. In some cases,

the difference can be large enough to cause a shift in their lubrication status (Y. Wang, Dhong, and Frechette 2015).

Wear is another relevant topic in tribology. It can be defined as the progressive damage and material loss which occurs on the surface of a component as a result of its motion relative to the adjacent working parts. It has far-reaching economic consequences which involve not only the costs of replacement, but also the expenses involved in machine downtime and lost production (Williams 1999). In a similar mode for the case of reducing the friction coefficient, textured surfaces have been shown to help suppress deterioration of the moving surfaces and involved parts. In their research, Borghi *et al.* (Borghi et al. 2008) found that debris, caused by tribological tests, filled the micro holes on textured surfaces, thus decreasing friction coefficient and wear. However, when those micro-holes were filled with debris, a high instability of the friction coefficient curve occurred.

2.3 Contact Mechanics

Many researchers have investigated the factors that influence adhesion on friction force (Bhushan and Nosonovsky 2003), indicating that the adhesion force is affected by the real area of contact which is a function of the normal load, surface roughness, and mechanical properties. The adhesion component of friction results from the junctions which are formed due to the surface structure (Baney, Butt, and Kappl 2010).

When two nominally plane and parallel surfaces are brought gently together, contact will initially occur at only a few points, as shown in Figure 2.3. As the normal load is increased, the surfaces move closer together and a larger number of the higher asperities on the two surfaces will come into contact. Since these asperities provide the only points at which the surfaces touch, they

are responsible for supporting the normal load on the surface and for generating any frictional forces which act between them. An understanding of the way in which the asperities of two surfaces interact under varying loads is therefore essential to any study of friction and wear (Hutchings 2001).

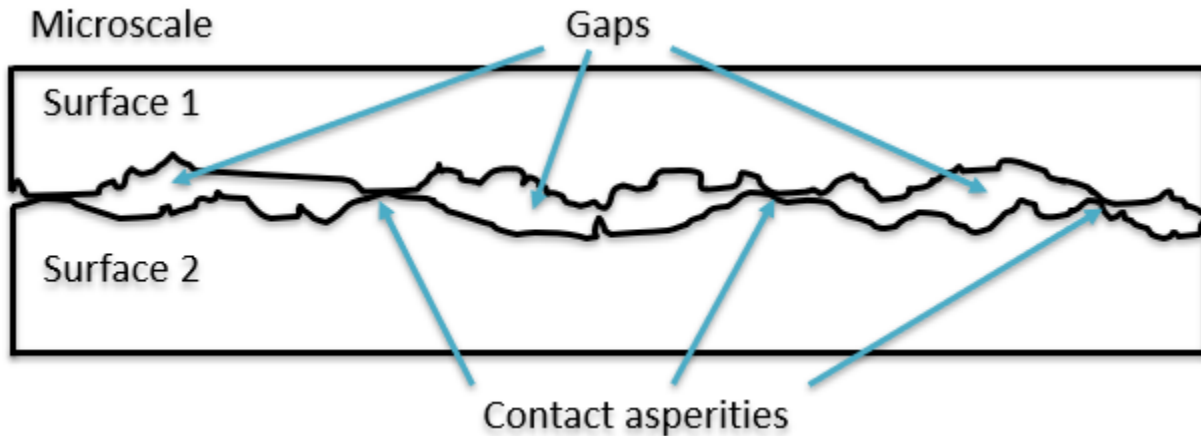


Figure 2.2. *Schematic representation of contact asperities between two plane surfaces at microscale level.*

The contact between solids is limited by surface roughness. Only a small portion of the apparent (or nominal) contact area interacts, and it must withstand the external loads acting on the solids. The roughness in these cases corresponds to the highest asperity heights located above the median reference plane of the topographies that make up the contact interface.

Geometrical effects on local elastic deformation properties have been considered as early as 1880 with the Hertzian Theory of Elastic Deformation (Hertz 1882). This theory relates the circular contact area of a sphere with a plane (or more generally, between two spheres) to the elastic deformation properties of the materials. In the theory, any surface interactions such as near contact Van der Waals interactions or other adhesive interactions are neglected.

2.4 Texture Modelling Techniques

Modelling can be helpful to reflect the creation of an additional hydrodynamic lift that can lead to a certain increase in load carrying capacity of the contact in cases of mixed and hydrodynamic lubrication (Gropper, Wang, and Harvey 2016). In addition, lubricant properties can be analyzed before tribological tests, saving time and helping to understand how dimple parameters and lubricant properties affect the practical results. But, finding optimal texturing parameters is still very challenging due to the large number of variables involved and the complexity of governing equations based on different forms of the Reynolds equations or Navier–Stokes equations. These equations are used in lubrication theory to analyze the pressure distribution on a thin viscous fluid film and motion for fluid flow, respectively. However, several studies were based on experimental approaches only, of which the most commonly used are pin-on-disc (Kovalchenko et al. 2004; Podgornik et al. 2012; Scaraggi et al. 2013, 2014; Braun et al. 2014; H. Zhang et al. 2014) and ball-on-disc (Amanov et al. 2012) setups as well as reciprocating sliding tests (H. L. Costa and Hutchings 2007). On the other hand, some studies were conducted on real components, such as: journal bearings (Lu and Khonsari 2007), thrust bearings (I. Etsion et al. 2004; Qiu and Khonsari 2011; Henry, Bouyer, and Fillon 2014) and seals (Bai and Bai 2014; Izhak Etsion 2004; X. Q. Yu, He, and Cai 2002). Tønder (Tønder 1996, 2004) suggested that the introduction of roughness at the inlet of a parallel sliding bearing provides a step-like configuration similar to a Rayleigh step bearing. It was also found that more lubricant is available in the pressure build-up zone, as the roughness at the inlet could prevent leakage.

Another set of explanations for a disturbed pressure distribution over single textures are inertia-related effects, which were first studied by Arghir *et al.*, (Arghir et al. 2003). As the simplified models based on the Reynolds equation or Stokes equations do not consider inertia

effects, they solved the full Navier–Stokes equations for different macro-roughness cells and showed that inertia effects could provide a load carrying capacity for flows with higher Reynolds numbers. However, the considered dimple geometries had very large aspect ratios (λ) that are quite different from the ones typically studied in lubrication theory, leading to pronounced inertia effects. Etsion's group (I. Etsion et al. 2014) found that partial texturing can improve the tribological performance by a so-called collective dimple effect, similar to the concept proposed by Tønder (Tønder 1996, 2004), showing that the textured inlet has a larger average film thickness than the non-textured outlet, and therefore partially textured contacts behave similarly to a Rayleigh step bearing. However, surface deformations and the effect of surface roughness were not considered (Gropper, Wang, and Harvey 2016).

Computational Fluid Dynamics (CFD) simulations have been also presented, for example, Sahlin (Sahlin et al. 2005) presented a CFD simulation in which by introducing a micro-groove on one of two parallel walls, a net pressure rise in the fluid domain was reached. Thus, a maximum load carrying capacity could be achieved with a dimple depth close to the depth at which a vortex (a flow recirculation within the dimple) appears. This flow recirculation produces a load carrying capacity on the walls, which is primarily a result of fluid inertia (Han et al. 2010, 2011), they also concluded that suitable geometric parameters would benefit lubrication. However, unsuitable geometric parameters will deteriorate lubrication properties. A completely contrary results were presented by Dobrica and Fillonin (Dobrica and Fillon 2009). They studied the validity of the Reynolds equation for a two-dimensional textured parallel slider configurations and concluded that inertia in general has a negative effect on the load carrying capacity.

Meanwhile, Yong *et al.*, (Yong and Balendra 2009) presented a CFD simulation on the lubrication behavior of journal bearing with dimples, concluding that the introduction of dimples

on surfaces is beneficial to lubrication performance in terms of friction force, compared to the smooth plate sliding, and the semi-spherical dimple is more efficient in reducing the friction.

Thus, tribological modelling of surfaces is of great interest in the contact mechanics area. Several factors (such as: lubricant conditions, contact parameters, and pressure forces) must be considered. CFD is an important tool used to solve and understand fluid flow behavior and has been used in numerous studies (Almqvist, Almqvist, and Larsson 2004; Elements, n.d.; Almqvist and Larsson 2002; Ohue and Tanaka 2013; Q. J. Wang et al. 2008; Zhu and Hu 2001). However, these are only considering the Reynolds equations to modelling of contacts as an Elastohydrodynamic lubrication region. Hu et al. (Y.-Z. Hu and Zhu 2000), proposed to divide the contact zone in two areas: the asperity contact region, and the hydrodynamic region. The modelling equations for both the hydrodynamic region and the contact regions are:

$$\frac{\partial}{\partial x} \left(\frac{\rho}{12n^*} h^3 \frac{\partial \rho}{\partial x} \right) + \frac{\partial}{\partial y} \left(\frac{\rho}{12n^*} h^3 \frac{\partial \rho}{\partial y} \right) = U \frac{\partial(\rho h)}{\partial x} + \frac{\partial(\rho h)}{\partial t} \quad (2.1)$$

where x must coincide with the movement direction, ρ is the pressure, n^* is the lubricant dynamic viscosity, h is the film thickness and U is rolling velocity.

The physical interpretation of Reynolds Eq. (2.1) is the equilibrium of fluid flow. The left-hand side of the equation represents the lubricant flow due to the hydrodynamic pressure, while the two terms on the right-hand side stand for the lubricant flow caused by surface motion in both tangential and normal directions (Zhu and Hu 2001).

The film thickness can be calculated as:

$$h = h_0(t) + B_x x^2 + B_y y^2 + V(x, y, t) + \delta_1(x, y, t) + \delta_2(x, y, t) \quad (2.2)$$

where h_0 is the average film thickness, B_x and B_y are constants related to the original geometry of contacting bodies (radii of curvature in the x and y directions), δ_1 and δ_2 represent the roughness amplitude of the surfaces, V is the surface deformation represented by a Boussinesq integral:

$$V(x, y, t) = \frac{2}{\pi E'} \iint \frac{\rho(\varepsilon, \varsigma) + \rho_c(\varepsilon, \varsigma)}{\sqrt{(x - \varepsilon)^2 + (y - \varsigma)^2}} d\varepsilon d\varsigma \quad (2.3)$$

where ρ is the pressure, ρ_c is the asperity contact pressure and E' effective Young's modulus.

Hu et al (Y.-Z. Hu and Zhu 2000), proposed using the same equations in the contact regions because as the film thickness becomes zero, the pressure flow vanishes, and the Reynolds Equation is reduced to the following form:

$$u \frac{\partial h}{\partial x} + \frac{\partial h}{\partial t} = 0 \quad (2.4)$$

Now, it is possible to solve the equations system without any extra information about the contact borders and boundary conditions through the same iteration loop. In order to describe the non-Newtonian lubricant properties, a viscosity term, n^* , was introduced in Eq. (2.1) and can be calculated by Eq. (2.5), considering possible shear thinning effects describe by Yang et al (Peiran and Shizhu 1990).

$$\frac{1}{n^*} = \frac{1}{n} \frac{\tau_0}{\tau_1} \sin h \frac{\tau_1}{\tau_0} \quad (2.5)$$

where $\tau_0 = 18$ MPa is the shear stress for mineral oil, τ_1 is the shear stress present on the lower surface and n is the limiting viscosity at low shear rate.

On the other hand, Wang *et al.* (Q. J. Wang et al. 2008) notes that their model does not take into account the effect of heat transfer, but it provides a consistent numerical platform for the evaluation and comparison of the performance of engineered surfaces. Meanwhile, Virtual Tribology Laboratory (VTL) is a software developed by Profito *et al.* (Profito, Zachariadis, and Tomanik 2011); in this software lubrication flow depends on motion, texture geometry, applied load and mechanical characteristics of the material. A deeper insight into tribological modelling using VTL will be provided in Chapter 5.

2.5 Machining Textured Surfaces

Nowadays, micro dimples can be fabricated on various types of materials using different manufacturing methods. Coblas *et al.* (Coblas et al. 2014), and Costa *et al.* (H. Costa and Hutchings 2015), classified the fabrication techniques into 4 technologies or methods, depending on the way that the workpiece is manipulated to create the textured surface:

- a) **Adding material technologies:** texture is obtained using chemical or physical deposition processes.
- b) **Removing material technologies:** creation of micro dimples by removing substrate material resulting in nano or microstructures with various shapes.
- c) **Material displacement technologies:** the substrate is plastically deformed and redistributed from a location to another, changing the surface structure.
- d) **Self-forming methods:** texture results after a succession of specific processes, implying a longer fabrication time. Wear-resistant regions are firstly formed on the substrate so that during the run-in period surface wear leads to texture development. More precisely, the wear resistant zones, which are not affected during the run-in period, rest positioned above the surrounding material which is worn out, creating a pattern.

Due the diversity of methods and techniques to create textured surfaces, most of them have not been deeply studied yet; for this reason Costa *et al.* (H. Costa and Hutchings 2015), recommends choosing a texturing method based on the simplicity of the texturing technique, commercial availability, equipment cost, texturing speed, and limitations in terms of the material, shape, and size to be textured. In the next paragraphs, surface texturing techniques are discussed, showing their main characteristics and limitations.

a) Adding material technologies

According to Costa *et al.* (H. Costa and Hutchings 2015), adding material technologies can be divided into chemical or physical deposition methods. The chemical processes are based on chemical reactions between the substrate and the deposited particles (reactants), while physical deposition methods are based on processes such as aggregation, solidification, evaporation, and sputtering. Chemical conversion methods are passive methods used to produce very thin layers composed of chromates (Chromatizing), phosphates (Phospating), or oxides (Oxidation) through galvanic or electroless recipes, i.e., aqueous bath or acidic attacks that induce spontaneous formation of an anti-corrosive film. Pattern formation is due to the use of a mask shield that usually consists of growth or adhesion inhibitors deposited on the substrate by micro contact printing technique or stamping. The main advantage of this process is its flexibility in terms of texture geometry, as continuous and discontinuous micropillars/microholes with various shapes can be obtained. Textures have heights ranging between tens of nm and a few mm and lateral dimensions limited at no less than a few micrometers. Equally, the method is suitable for both planar and cylindrical substrates, its resolution being somehow dependent on the masking process. The main disadvantage is given by the exhaustive chemistry knowledge required for the selection of inhibitors, deposited materials, and substrate materials. Even for compatible components, texture

height is limited and dependent on the substrate material. Another inconvenience results from the reaction chamber that imposes limited workpiece dimensions. Only small and medium substrates can be textured (<500 μm), while the process can be defined as environmentally unfriendly as it requires the use of toxic gases.

Inkjet printing is a good example of a physical deposition method; this technique implies the deposition of solid particles (conducting polymers, structural polymers, ceramics, and metals) to form wear-resistant reliefs. Solid particles are transported to the substrate through liquid precursors (colloidal solutions, sol-gel) and form various microstructures after precursor evaporation and/or solidification. The main advantage of inkjet printing is the use of point by point deposition which offers good precision in the final structures. Micro feature dimensions range between 5 and 900 μm heights and 20 and 200 μm lateral dimensions. Printing resolution depends on the ink jet printer resolution, particle diameter, and material characteristics. Some researchers (Bruzzone et al. 2008), have pointed out that this method is suitable only for flat substrates with reduced dimensions. However, a system composed of multiple parallel nozzles (guiding the fluid to the substrate) should increase method's efficacy, decreasing texturing time, and making it appropriate for the processing of larger substrates.

Applying the inkjet printing technique, researchers (Tay, Minn, and Sinha 2011; Beng, Minn, and Sinha 2011) have investigated the behavior of textured substrates in ball-on-flat and flat-on-flat sliding tests in the presence of a nano-lubricant (fluorinated lubricant) and concluded that both friction coefficient and wear are reduced in comparison with flat untextured specimens. According to those researchers, the improved tribological performances may be due to both reduced contact area and the nano-lubricant presence.

Inkjet printing can be used to create super hydrophobic surfaces by growing zinc oxide (ZnO) microstructures on patterned glass substrates (Bewilogua et al. 2009), as shown in Figure 2.4, or very high micropillars through successive deposition of ink (deposition of piezoelectric ceramics or titanium dioxide particles on substrates of same materials). Using this technique, a good compatibility and stacking of the successively deposited layers, a good densification rate, and a high mechanical strength of the ceramic microstructures (Xing et al. 2013) have been reported. Insufficient crystallization time between successive drop depositions can sometimes lead to the formation of texture defects (J. Park et al. 2006).

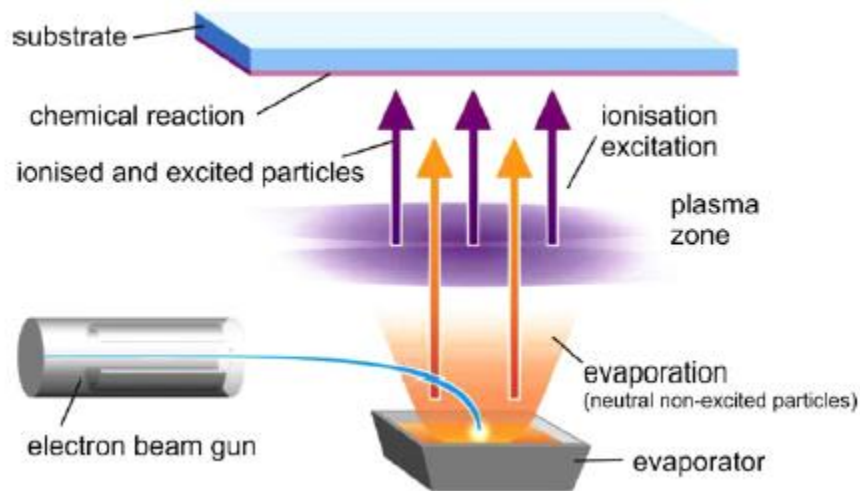


Figure 2.3. *The principle of plasma assisted electron beam evaporation (Bewilogua et al. 2009).*

Disadvantages of the Inkjet printing method include the lack of details about the method applicability on metallic surfaces and their behavior in mechanical components. High temperatures that are sometimes required for sintering (thermal curing) can represent a problem depending on the substrate material (plastic materials). The method's precision is not very good and seems dependent on contact time between the stamp and the substrate: a short contact period can lead to

poorly condensed patterns while a long contact period may result in blurred patterns. (Coblas et al. 2014).

b) Moving material technologies

In this case, the change in the surface structure is attributable to plastic deformation and redistribution of material from some parts of the surface to others (H. Costa and Hutchings 2015). This method can use a single-shaped indenter, a patterned tool, or a patterned roller (in which case it is called vibro-rolling), the patterning mechanism is based on the transfer of the tool shape onto the workpiece surface by plastic deformation. Indentation tools are generally covered by a thin layer of hard and very abrasive material (like diamond powder) and by being pressed into the substrate (Coblas et al. 2014). The vibro-rolling technique is used to create regular texture patterns on a surface through the plastic deformation of the substrate, rather than cutting as in the case of polishing, grinding, and honing. Plastic deformation occurs when the yield strength of the material is smaller than the contact stress imprinted by the tool surface. It can be used to create various patterns on cylindrical surfaces, plane surfaces, and other complex geometries, as shown by Schneider (Schneider 1984), and it is preferred to turning, grinding, and polishing methods, improving fretting resistance and wear of metal surfaces (Bulatov, Krasny, and Schneider 1997).

Another surface technique included within the present category is burnishing. This method can be used to reduce roughness (similar to polishing or lapping), but it can also be used to create specific patterns on slide bearing sleeves (eccentric burnishing) in which case an improved lubrication and frictional behavior. The method is appropriate for the texturing of a plane and cylindrical surfaces as shown by some researchers (Koszela et al. 2012; Galda, Koszela, and Pawlus 2007). Similar to honing and grinding, burnishing is a low-priced manufacturing method (Coblas et al. 2014).

Another technique that is part of this texturing method is called chemical-induced material displacement. In this case, the molecular migration mechanism can be used to create nano textures on substrates coated with azobenzene-based polymeric films. The method is based on the polymer chain migration from laser beam photoirradiation induced movements (Coblas et al. 2014). Textures with depths and widths from tens of nanometers to almost 500 nm have been already produced (Fiorini et al. 2000; Leblond et al. 2009). Surface wrinkles, i.e., nano and micro undulations, can be obtained by different multi-step processes, such as oxidation of PDMS substrates by plasma oxidation or using UV-Ozone to create a stiff silica layer on substrate's surface, step succeeded by thermally or mechanically induced substrate stretching or compression. These methods allow the formation of disordered wavy structures and unidirectional undulations (due to uniaxial stretching or compression) with dimensions between tens of nanometers to a few micrometers (Coblas et al. 2014). Equally, the use of pre-patterned substrates allows the formation of complex patterns with controlled shape and orientation (Schweikart et al. 2010). The main limitations of both texturing technologies are the substrate materials which are not commonly used within tribological systems (i.e., azobenzene-based polymers, PDMS, and silica) as well as texture fragility, and surface cracks (Coblas et al. 2014).

c) Self forming technologies

For this case, wear-resistant regions are formed on a surface so that a texture develops through wear of the surface, with the wear-resistant regions being left standing above the surrounding material (H. Costa and Hutchings 2015). An example of this technique is thermal implantation; this method is based on the implantation of hard, wear-resistant regions into a substrate so that during use, the substrate (less resistant) wears out and a pattern is formed from the hard implanted phases (which can support higher contact pressures) (Coblas et al. 2014). A

thermal implant of TiC into a steel substrate showed a 100% increase in hardness (Fletcher et al. 2000), which could be beneficial for some applications. However, this technique needs special facilities and texture fabrication time is high.

d) Removing material technologies

With this technique, textures are created by removal of material from the surface, creating small depressions (H. Costa and Hutchings 2015). In their research, Coblas *et al.* (Coblas *et al.* 2014), divided removing material technologies into processes which imply high temperatures during texturing process (laser technologies, electrical discharge methods, electron beam or ion beam methods); chemical reactions (etching), and mechanical process (grinding, honing, ultrasonic machining and blasting). Another moving material method that is commonly used was presented by Wakuda *et al.* (Wakuda et al. 2003). In this case, two different texturing techniques were used to create micro dimples on a ceramic surface; abrasive jet machining and laser beam machining. Abrasive technique is a cheap method to create textured surfaces, but laser beams usually have high energy consumption.

(1) Laser Surface Texturing (LST)

Laser surface texturing (LST) is the most common method used today to texture surfaces in engineering applications (Izhak Etsion 2005). This technique has been used to texture a wide range of materials, from polymers to metals and ceramics (H. Costa and Hutchings 2015). Also, this technique allows for the production of patterns with small features. For example, feature depths of 200 nm and diameters of 20 mm could be obtained in steel samples by using a femtosecond pulse laser. Another approach, based on laser-induced periodic surface structuring, used a femtosecond laser to produce an array of dimples with diameters of 1 mm. However, the use of LT presents limitations. First, the ablation mechanism often leads to the formation of raised

features around the pockets, which originate from the ejected molten material. These lateral rims are normally hard due to the microstructural changes caused by the process and can cause severe abrasive wear of the countersurface and therefore need to be removed, either by mechanical polishing or by laser polishing. The second issue for LST is the texturing speed. The process involves ablation, which changes the material state directly from solid to vapor in a very short period, with little metallurgical surface damage. The ablation fluence threshold for materials varies from soft metals to glasses and hard composites. If the laser system has a sufficiently high maximum pulse energy, a micro dimple can be produced through laser ablation using a stationary laser spot with a size comparable to the dimple. Furthermore, as long as the laser fluence (pulse energy/laser spot area) can at least exceed the ablation threshold fluence for the target material, this can be done without the need for laser spot scanning; the depth of the dimple will depend on the number of pulses. The use of high pulse energies, small spot diameters, and (ultra)short pulse durations has allowed material removal by ablation to be achieved for a wide range of materials at increasing texturing speeds.

However, since the features are normally produced in a serial sequence, the texturing time for larger components can still be long, in particular for cheaper LST facilities that use long pulse durations and large spot sizes. Many components that could have their performance increased by surface texturing are cheap, so they might require cheaper texturing methods in order for the increase in tribological performance achieved through texturing to be cost-effective. An alternative LST technique that is substantially faster is laser interference texturing. In this technique, interference fields produced by several coherent high-power laser beams can produce periodic patterns composed of line-nets or dot-like features. The interference pattern covers a size corresponding to the beam diameter, which increases texturing speed substantially, but the

maximum sizes of the individual features can be too small for some lubricated tribological applications (up to around 3 mm in width and 1 mm in depth). Therefore, such features might be desirable for applications involving EHL, but too small for hydrodynamic lubrication or starved lubrication. Another possible problem is that the process changes the topography of the whole surface, instead of only creating localized ablated features.

Another group (Prina Mello, Bari, and Prendergast 2002) has worked using excimer or exciplex lasers. In this method, the laser beam is guided, focused, and concentrated through a system of lens. The mask allows the creation of various shaped microfeatures (circles, squares, triangles, etc.). The technique is flexible and fast, with very good accuracy and resolution. Process resolution depends on laser wavelength, texture dimensions depend on the spot size (given by the optics of the system), and texture depth is given by the number of pulses and their duration. However, the production cost of the mask is a big disadvantage of this method. Figure 2.5 shows the schematic for this technique.

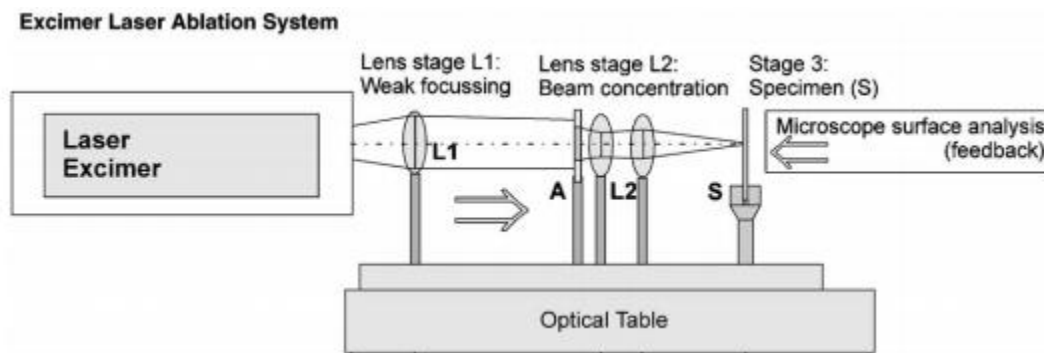


Figure 2.4. Arrangement used in the excimer laser ablation study (Prina Mello, Bari, and Prendergast 2002).

The influence of laser surface texturing (LST) on mechanical systems performance is given by various parameters, such as operating conditions (load, pressure, sliding speed, temperature), lubricant properties, and texture geometric parameters such as; shape, depth,

diameter, lateral dimensions, area ratio, (total dimple area over total surface area), distance between dimples and aspect ratio (dimple depth over dimple diameter). (Izhak Etsion 2005a). Another important aspect in LST is the thermal effect of the laser beam on the substrate. The substrate can be affected by the laser beam heat and thus changes of its metallurgical property can occur. Laser texturing process requires expensive equipment, a laborious and very costly post-processing step (CNC programming is expensive, especially for cylindrical workpieces), and high operating energy during the texturing process. However, the manufacturing costs strictly depend on several parameters: (i) the texturing system (laser source, displacement control, focusing lens); (ii) the substrate material; (iii) texture dimensions; and (iv) the number of workpieces which are to be machined—prototyping or series production (for high volumes of treated pieces the cost can be substantially reduced).

(2) *Chemical based Manufacturing.*

In this method chemical reagents are selectively applied to a surface to remove material in specific regions, in order to produce a textured surface (Bruzzone et al. 2008). The material is removed from selected areas by immersing it in a chemical etchant. Etching only in selected areas can be achieved either by masking or by self-assembling of solid particles and/or liquids to form a mask. Material removal results from a microscopic electrochemical cell action exposed to ultraviolet light (UV), equivalent to that responsible for corrosion or chemical dissolution of a metal. The resolution of the features that compose the texture depends strongly on the method used to mask the surface. Depending on the printing method, texturing can also be applied to surfaces with irregular shapes. Also, there are few restrictions related to the shape and distribution of the features that compose the surface texture. The overall speed of these methods is restricted by the speed of both the printing method and etching process. Normally, these methods change the

surface topography, but they do not change the mechanical properties of the textured region. This process can be divided into 4 steps; (i) resist deposition on substratum, (ii) resist exposure to ultra violet light (UV), (iii) resist development, and (iv) baking of the resist onto the substratum, and resist removing or striping . A schematic of this proces is shown in Figure 2.5.

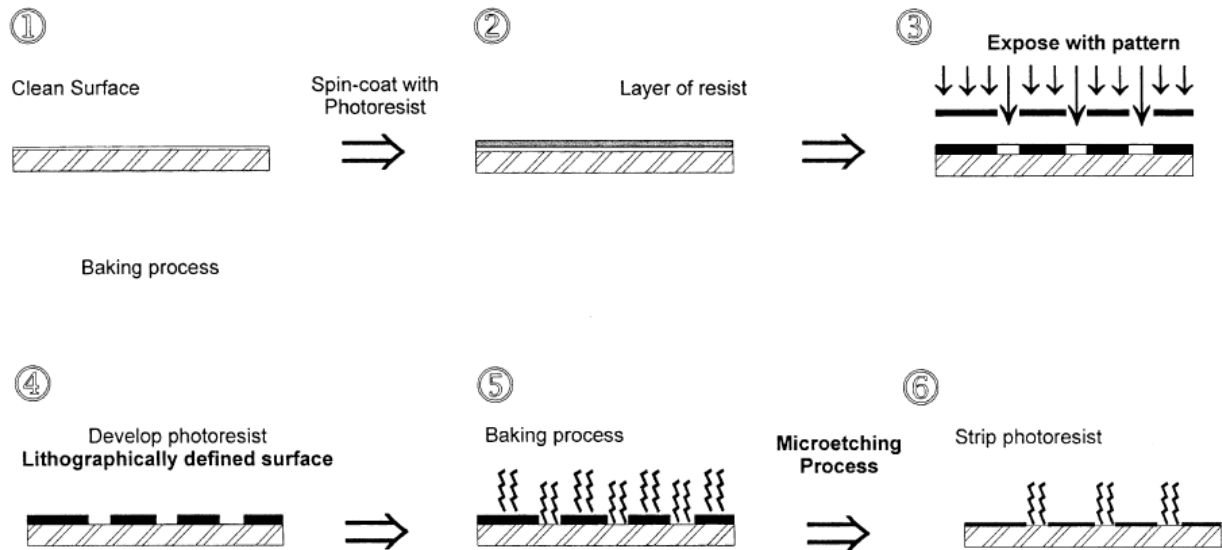


Figure 2.5. *Lithography process: six-phase scheme (Prina Mello, Bari, and Prendergast 2002).*

Wet etching can be isotropic (material etched at the same rate in all directions) or anisotropic (etching rate depends on the crystal planes); therefore, various shapes of 3D textures can be obtained. Another key advantage is that the treatment can be applied also to irregular shape substrates and complex geometries. Texturing process speeds depend on both printing method (mask creation) and etching speed, while its accuracy depends directly on the method used to create the masking shield. For this technique, the main equipment costs are related to the printing method. On the other hand, etching provides an efficient control of material removal. Wet etching is a low-cost method as it requires only chemical solution baths to etch the unprotected substrate

regions. On the contrary, dry etching methods require the use of expensive equipment (vacuum chambers) and is more difficult to implement. This technique has been used to analyze the influence of micro dimples on the silicon carbide surface in water (X. Wang et al. 2003).

In dry etching, a normal laboratory bench can be used, in order to greatly reduce the complexity and costs of the process in comparison to using a clean room. However, to extend this technique to an industrial environment, a clean workspace environment with controlled yellow illumination would be needed, since the photoresist resin is not sensitive to light of this wavelength. This technique was used to study the effects of the surface texturing of coated silicon under boundary and dry sliding conditions (Pettersson and Jacobson 2003).

(3) Inclined Micro-milling

Dimpled surfaces have been realized through ball end milling (Eldon Graham, Park, and Park 2013; Pratap and Patra 2018). Advantages of micro-milling producing micro textured surfaces include: high material removal rates, accurate surface finishes, and few restrictions on workpiece materials (Fleischer and Kotschenreuther 2006). Micro-milling has been used to produce a variety of different surface structures by altering the cutting technique (J. Yan et al. 2010), or changing the micro tool geometry (Matsumura and Takahashi 2011).

Compared to the previous surface texturing methods, inclined micro-milling is an efficient method to fabricate micro-dimples because of the ability to machining several features in a single setup. Thus, the micro-milling technique significantly reduces the time needed to fabricate dimpled surfaces by creating a row of dimples in a single pass of the cutter (Pratap and Patra 2016; Resendiz et al. 2015). Also, the inclined micro-milling is a cost-effective technique because complex systems are not necessary, nor a different etchant for different materials and a mask is not required.

In addition, inclined micro-milling is very precise due to computer control of the cutting tool (Pratap and Patra 2018; Eldon Graham, Park, and Park 2013).

Micro-milling thus represents a very flexible method, and with the right combination of cutting technique and tool geometry, a wide variety of surface structures can be developed. However, care must be taken when using micro milling to pattern surfaces, since in machining patterns, various things can detrimentally influence the resulting surface structure, such as oscillations of cutters while rotating, cutting tool wear or breakage, tool deflections, non-uniformity of cutting conditions, varying rigidity of the workpiece or clamping system, and abrupt movements of the workpiece (Dimov et al. 2004).

In conclusion, this review suggests that the choice of a texturing method is mainly based on the following criteria: simplicity of the texturing technique, commercial availability, equipment cost, texturing cost, texturing speed, minimum size of the individual features that compose the texture pattern, minimum and maximum depth of the features, and limitations in terms of the substrates to be textured(material, shape, and size) (H. Costa and Hutchings 2015). Compared to other surface texturing methods (such as wet or dry etchings, abrasive jet machining, and laser processes) inclined micro-milling is a fast and effective method to fabricate micro-dimples.

2.6 Micro Machining Force Modeling

Force modelling of machining operations is central to understanding how to improve both longevity and efficiency in micro tools (E Graham, Park, and Park 2013). Similarly, tool geometry and cutting technique have significant effects on cutting forces and surface finishes (Fontaine et al. 2007). Conventional cutting force models for flat end mills can be modified to predict forces for inclined flat end milling. The force components on the milling cutter must be considered to

account for the effects of spindle inclination. Inclined cutting of dimples with a flat end mill is periodic and not continuous as in upright milling, and each flute enters the work piece surface with a certain frequency. Since the tool geometry of a flat end mill allows for uniquely shaped dimple geometries, an investigation into how cutting forces are affected is warranted (E Graham, Park, and Park 2013). As mentioned before, the inclined ball end milling technique significantly reduces the time needed to fabricate dimpled surfaces by creating a row of dimples in a single pass of the cutter. Many other machining methods are not efficient by comparison as individual dimples are made through repeating horizontal and vertical movements of the cutting tool. While a tilted ball end mill can reduce machining time, there are limitations to the maximum depth of cut that can be specified. Excessive cutting forces in micro end milling can cause severe deflection, which can lead to tool breakage and excessive tool wear (Chae, Park, and Freiheit 2006). Many of these problems can be monitored and avoided through measuring cutting forces and comparing to analytical models.

2.7 Friction Reduction Due to Textured Surfaces

Most of the researchers who work on issues related to textured surfaces have done so in the experimental area using laser systems. In their research (Kovalchenko *et al.* 2005), dimpled surfaces were created with different densities using a laser surface technique, tribological experiments were conducted with a pin-on-disk apparatus at sliding speeds in the range of 0.015–0.75 m/s, and nominal contact pressures that ranged from 0.16 to 1.6 MPa. Two oils with different viscosities (54.8 and 124.7 cSt at 40° C) were used as lubricants. The test results showed that laser texturing expanded the contact parameters in terms of load and speed for hydrodynamic lubrication, as indicated by friction transitions on the Stribeck curve. The beneficial effects of laser surface texturing are more pronounced at higher speeds and loads and with higher viscosity oil. A

lower area dimple density is more beneficial for lubrication regime transitions. Also, dimples serve as pockets for wear particles embedment, preventing debris from further damaging the substrate surface via ploughing (Meng *et al.* 2010).

In a similar way, M. Wakuda *et al.*, (Wakuda *et al.* 2003) conducted a study to clarify the potential of textured micro-dimples on a silicon nitride ceramic plate mated with cylindrical-shaped steel elements. The effect of surface texturing with a variety of dimensions and density of micro-dimples was evaluated to optimize the dimple pattern. Two dimples geometries were produced for this research, one by Abrasive Jet Machining (AJM) and another one by Laser Beam Machining (LBM). Figure 2.7 shows a topographic picture of both dimple geometries, indicating a spherical morphology, while the LBM process led to a rather angular dimple. The dimple size was set at 40, 80, or 120 μm in diameter and area densities of 7.5, 15, and 30 percent.

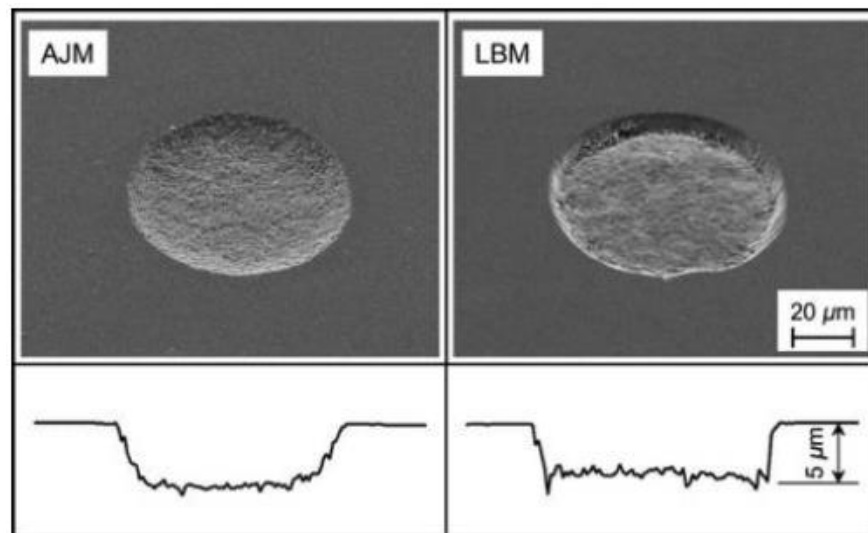


Figure 2.6. Appearance of micro-dimples produced by AJM and LBM, both of which exhibited characteristic profiles (Wakuda *et al.* 2003).

The friction coefficient was studied using a pin-on-disk machine and compared to a smooth surface without texturing. Some samples successfully realized reductions in friction coefficient from 0.12 to 0.10. It was found that the tribological characteristics depended greatly on the size and density of the micro-dimples, while the dimple shape did not significantly affect the friction coefficient, regardless of rounded or angular profiles. A dimple size of approximately 100 μm at a density of 5-20 percent was recommended. Also, Li *et al.*, (Li *et al.* 2010) studied the relevance of the surface texturing as an effective tool in improving the tribological performance of contacting surfaces and the significance of the development of self-lubricating composites which can resist wear at high temperatures. LST was performed on the nickel-based composites by a Nd:YAG pulse laser to form the regularly-arranged dimples with diameters of 150 μm . The tribological properties of the textured and nickel-based composites were investigated by carrying out sliding wear tests against an alumina ball as a counter face using a high-temperature ball-on-disk tribometer. Powder of MoS_2 (20 μm) was smeared on the textured sample. Tests were conducted at a sliding speed of 0.4 m/s and at normal loads ranging from 20 to 100 N and temperatures ranging from room temperature to 600 $^\circ\text{C}$. The friction coefficient of the nickel-based composite textured and smeared with molybdenum disulfide was found to decrease from 0.18 to 0.1 at the temperature range from 200 to 400 $^\circ\text{C}$. To gain a deeper insight into the lubrication mechanisms of textured surfaces, some researchers have used both experimental and numerical models. For example, Tang *et al.*, (Tang *et al.* 2013) investigated the effect of surface texture to reduce the friction and wear of a steel surface. A numerical model of the load carrying capacity of multi-dimples was developed to analyze the mechanism responsible for reducing friction and wear by surface texturing, and the effect of surface texturing with several dimple area fractions was evaluated to determine the optimal dimple pattern. Three dimple area fractions (2, 5

and 10 percent) were varied by changing the diameter of each dimple. The results indicated that 5 percent optimal dimple area fractions had generated the greatest hydrodynamic pressure compared to other fractions, and reduced friction and wear up to 38 and 72 percent, respectively.

2.8 Summary

According to previous literature, micro dimples are an effective way to improve tribological performance in mechanical components. Most of the studies analyzed in this review used a laser beam machining technique (Wakuda *et al.* 2003) or a Reactive Ion Etching method to create dimples (X. Wang *et al.* 2003). However, in those techniques a complex system or special facility were necessary. Compared with those surface texturing methods, inclined micro-milling offers some advantages, such as: a reduction in time to create micro dimples, high material removal rates, controlling the depth density and dimpled area, accurate surface finishes, and few restrictions on workpiece materials (Fleischer and Kotschenreuther 2006).

In addition, micro dimples play an important role in the lubrication regime. In the elasto/hydrodynamic lubrication regime dimples create a lift-up pressure effect (Samuel Cupillard, Michael J. Cervantes 2008). In the boundary lubrication mode, dimples can act as an oil reservoir, thus providing a continuous lubricant supply to the contact interface, helping to decrease surface to surface contact (I Etsion 2004). Also, dimples act as traps for wear debris, which decreases ploughing effect (Kovalchenko *et al.* 2005).

Fluctuations in film thickness and pressure are important factors to consider because they govern most surface failures, such as: excessive wear, pitting, and scuffing (L. Chang 1995). Boundary films increase the overall lubrication film thickness and move the transition between EHD or mixed lubrication and boundary lubrication towards more severe operating conditions.

One of the parameters that greatly influences the friction under certain conditions is surface roughness (Galda, Pawlus, and Sep 2009), and film thickness is affected by surface roughness. Surfaces of metals are actually rough, and asperities representing the roughness of the surface exist in the surfaces of metals (Sahin, Çetinarslan, and Akata 2007). Thin viscous boundary films formed on rubbing surfaces can reduce asperities' interactions of rubbing surfaces under very thin film conditions. In addition, surface texturing could help to increase the separation of rubbing surfaces under mixed lubrication conditions if the depth of micro-features is properly designed (Křupka and Hartl 2007; Křupka, Vrbka, and Hartl 2008; Křupka and Hartl 2007).

In this research, the friction of asymmetrical and symmetrical dimples on sliding surfaces is analyzed and the effect of multi-textured dimples is proposed. In this way, it is planned to generate a double texturing on the dimpled workpiece to further reduce friction coefficient.

CHAPTER 3. FABRICATION AND MODELLING OF DIMPLES USING END MILLING TECHNIQUE

There are many methods to generate micro dimples, but they are limited by factors such as the material to be used and the micro-dimple geometry required to create the dimples. Some others such as wet or dry etchings, and laser processes are expensive or need special facilities. The inclined end milling technique (Kogusu and Ishimatsu 2008; J. Yan *et al.* 2010; Eldon Graham, Park, and Park 2013; Resendiz *et al.* 2015; Pratap and Patra 2018) is an efficient and cost-effective method to fabricate micro dimples, because complex systems are not necessary. Inclined micro-milling significantly reduces the time needed to fabricate dimpled surfaces by creating a row of dimples in a single pass of the cutter, does not have a high energy consumption, and a mask is not required. However, due to its small size, special attention must be given to using micro tools. Parameters such as cutting depth, workpiece material, feed rate, RPM and number of flutes can affect its efficiency and lifetime. Thus, a cutting force modelling technique to detect oscillations of cutters while rotating, cutting tool wear or breakage, tool deflections, and non-uniformity of cutting conditions is presented in this chapter.

3.1 Fabrication of Textured Surfaces

Micro milling has become available for fabricating micro textured surfaces. With the right adjustments, the spindle speed and feed rate can be set so that the flutes of the cutter create periodic dimpled patterns onto a workpiece surface. Tool breakage or deflections are common while machining dimples, affecting the final texture. An effective method to avoid this is to model the cutting forces. Comparison of measured machining forces with those predicted by the model can

be used to identify issues with patterning the surface, such as; uniform cutting, oscillations in the cutter, or tool wear (Chae, Park, and Freiheit 2006). The performance of textured surfaces depends upon the geometry of the surface patterns. It is, therefore, essential to understanding how different machining parameters affect the resulting topographic structure. Thus, the components of cutting forces in each axis (F_x , F_y , and F_z) as shown in Figure 3.5 can be predicted and the cutting parameters can be corrected.

3.1.1 Dimple Geometry

The shape of each dimple is a function of the tool geometry, depth of cut, feed rate, and spindle speed. The spacing between adjacent dimples, s_d (as shown in Figure 3.1), is also a function of these process parameters which can be obtained as:

$$s_d = \frac{60f}{nN} \quad (3.1)$$

where f is the feed rate in mm/s, n is the spindle speed in RPM, and N is the number of flutes.

The linear pitch (dimples/mm) in the feed direction for each row is inversely related to the spacing:

$$x_{pitch} = \frac{1}{s_d} \quad (3.2)$$

By increasing the feed rate or decreasing the spindle speed, the tooth passing rate becomes smaller and the spacing between dimples becomes larger, resulting in fewer dimples per row. In contrast, decreasing the feed and increasing the spindle speed will result in more closely packed dimples.

The spacing between rows of dimples, d_r , is a process parameter directly controlled by the operator during machining. The in-row offset between dimples in adjacent rows, d_o , is also controlled during the machining process. Figure 3.1 represents a dimpled surface schematic showing the aforementioned variables. Dimples can have different sizes and shapes, such as; square, triangular, semi-circular, chevron and drop shape which depends on the texturing technique and tool used.

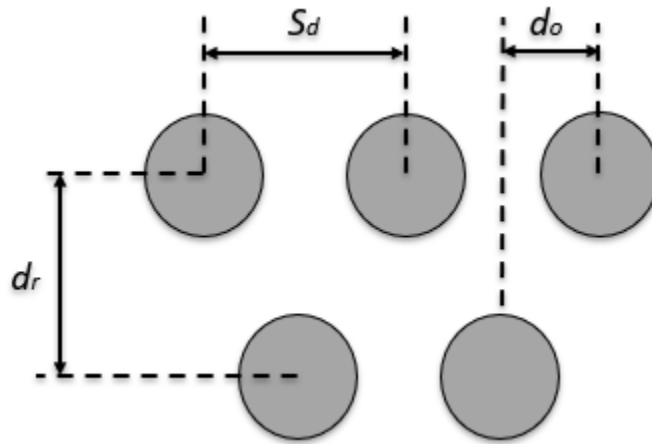


Figure 3.1. *Dimpled surface schematic drawing.*

If the spacing between each row of dimples, d_r , and the total flat surface area of the workpiece to be machined, A_w , are known, the total number of dimples, N_d , can be estimated by Equation 3.3. Thus, the density of dimples, D , (dimples/mm²) can then be found by Equation 3.4:

$$N_d = S_d * l_{row} * \#_{rows} \quad (3.3)$$

where l_{row} is the length of a row in mm and $\#_{rows}$ are the total number of rows machined.

$$D = \frac{N_d}{A_w} \quad (3.4)$$

Higher spindle speeds and lower feed rates will result in a higher density of dimples, while lower spindle speeds and higher feeds will have the opposite effect. Equation 3.4 assumes that density is related only to the feed rate and spindle speed, when in reality, density is also indirectly related to dimple size. With a larger depth, more of the cutting tool will be immersed into the material surface and result in larger sized dimples.

3.1.2 *Machining of Patterned Surfaces*

Flat and dimpled surfaces were machined using a computer numerical control (CNC) micro-milling system. Using the inclined micro-milling process, dimples with different characteristics (such as density, patterns, shape, and depth of cuts) can be machined.

This system is graphically depicted in Figure 3.2(a) and photographed in Figure 3.2(b). The CNC was mounted and secured on a vibration isolation table to insulate the machining system from the ground. An electric spindle (NSK Astro-E 800Z) was mounted onto a bracket that allowed the spindle to rotate at an inclination angle relative to the sample surface and to be secured during machining. Translation of the workpiece below the spindle during machining and friction testing was achieved by mounting the workpiece on linear precision stages (Parker Daedal 10600). These linear precision stages were actuated with stepper motors that were computer controlled (National Instruments PXI-1042Q). Calibration of the stepper motors was made by measuring the real

displacement of the stage using a Keyence Laser Displacement Sensor (LK-G3001) in relation to the number of steps counted during the translation of the stage.

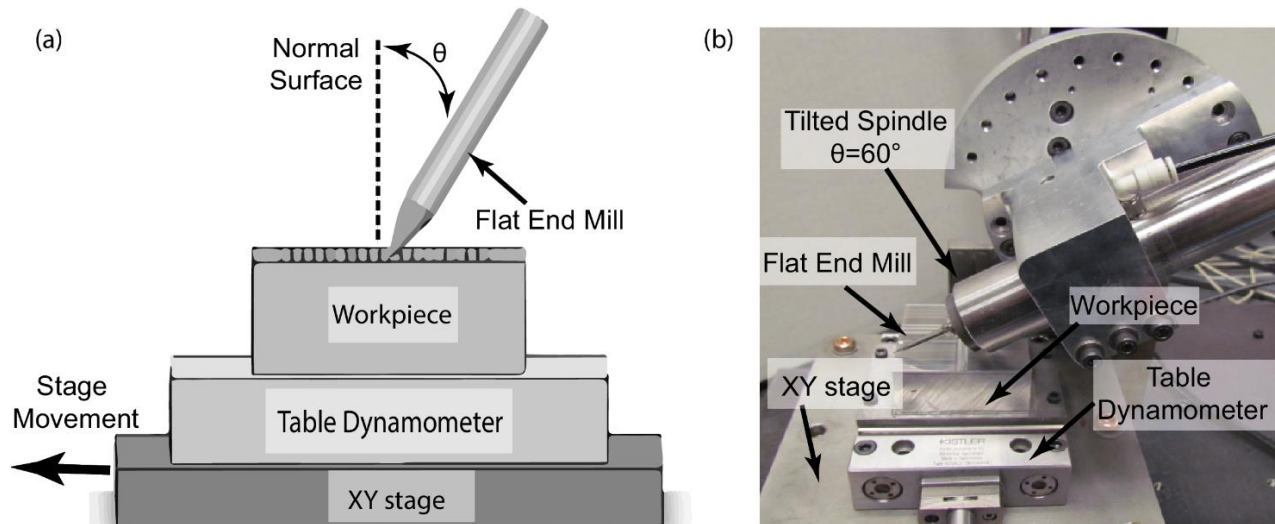


Figure 3.2. (a) Schematic of the machining system used. The flat end mill is tilted with respect to the surface normal of the workpiece to produce the dimpled surface. (b) Photograph of the end mill setup used to produce the dimpled surfaces. The spindle in this case is at an inclination angle (γ) of 60° with a flat end mill attached.

Specimens were produced by fixing an aluminium 6061-T6 workpiece to a piezoelectric table dynamometer (Kistler 9256C), allowing for future measurements of cutting and friction forces. The 6061-T6 alloy is widely used in the aircraft, aerospace, and automotive industries. Before producing dimples, the surface of the aluminium workpiece was flattened by flat milling the top layer of the surface with the spindle positioned so that its long axis was perpendicular to the workpiece surface normal. To avoid chatter effects, feed rate and depth of cut were properly selected. In addition, the entire milling system was secured to a vibration isolation air table to eliminate the possibility of capturing unwanted ground vibration signals.

To ensure a sufficient supply of oil for lubricated surfaces during friction testing, a small depression of about 2 mm was machined onto the surface of the workpiece. This depression

ensured that the lubricated and unlubricated surfaces had the exact same surface normal in subsequent friction testing. Following the surface planning and milling of the oil reservoir, the surfaces were polished using a P800 grit sandpaper to remove machining marks and reduce surface roughness. The surface roughness was measured over a $1 \times 1 \text{ mm}^2$ area to be less than $0.11 \pm 0.02 \text{ }\mu\text{m}$ (Mitutoyo SJ-201P). To measure cutting during dimple fabrication and friction forces, analog signals from the table dynamometer were amplified by a factor of 10 using a Kistler Charge Amplifier 5010, and the signals were digitally recorded using a National Instruments BNC-2110 at a sampling rate of 1 kHz. Dimpled surfaces were machined for an area of $40 \text{ mm} \times 4 \text{ mm}$ by fast translation of the sample workpiece while the end mill, inclined at angle of 60° to the surface normal, was lowered until the rotating cutting tool just reached the workpiece surface.

3.1.3 *Flat End Mills*

Milling is a process of generating machined surfaces by progressively removing a predetermined amount of material from the workpiece, which is advanced at a relatively slow feed rate to a milling cutter rotating at a comparatively high speed. The characteristic feature of the milling process is that each milling cutter tooth removes its share of the stock in the form of small individual chips. In addition, the micro tools can be made of different materials such as tungsten carbide or even diamond.

Tungsten is a common material used in machining operations because it is economic, shows a high resistance to wear and provides good fracture toughness when machining ferrous materials. In this work, a Tungsten micro Flat End Mill with only two flutes and having a diameter of $730 \text{ }\mu\text{m}$ was used. Figure 3.3 shows a picture of a Flat End Mill taken with the optical profilometer (Zeta-20).

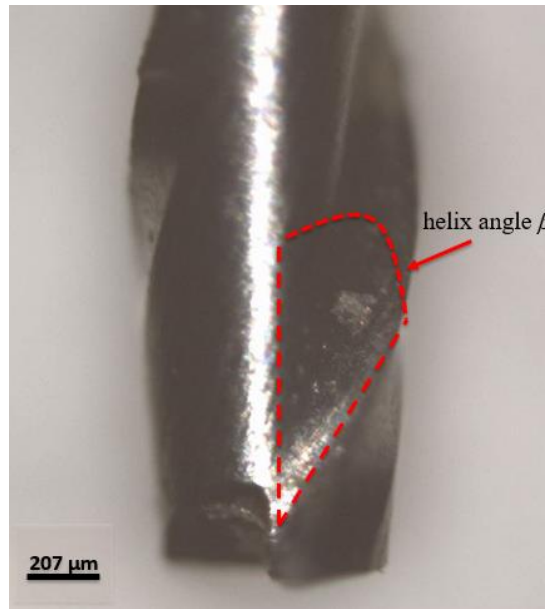


Figure 3.3. *Picture of Flat End Mill made of Tungsten carbide having two cutting flutes, with a diameter of 730 μm .*

Micro tools having only two flutes have the greatest amount of flute space, allowing for more chip-carrying capacity in softer materials (such as aluminium). However, some disadvantages are oscillations of cutters while rotating, cutting tool wear and breakage, tool deflections, and a non-uniformity of cutting conditions (Resendiz et al. 2015). For these reasons, asymmetrical depth dimples as shown in Figure 3.8 were created on an aluminium workpiece when using a Flat End Mill.

3.1.4 *Single Crystal Diamond Cutter*

Diamond cutters are extensively used in ultra-precision machining operations of non-ferrous materials such as aluminium or copper because of their good wear resistance, low friction coefficient, and low chemical affinity between diamond and those materials. In addition, single crystal diamond tools have a sharper edge and a higher thermal conductivity than conventional

Tungsten end mills, diamond tools also present a high hardness, and low adhesion which prevents built-up-edge (Jeong-Du Kim and Youn-Hee Kang 1997; Heaney *et al.* 2008).

Resulting from these properties, diamond cutters produce surface textures with lower variation and more exact tolerances than cutters produced from other materials (J. Yan *et al.* 2010). Moreover, having only one cutter helps to prevent non-uniformity of cutting depth caused by oscillations while the micro tool is rotating, as can be observed in Figure 3.9 where successive dimples have the same depth. Figure 3.4 shows a picture of the single crystal diamond cutter used in this research taken with the optical profilometer (Zeta-20).

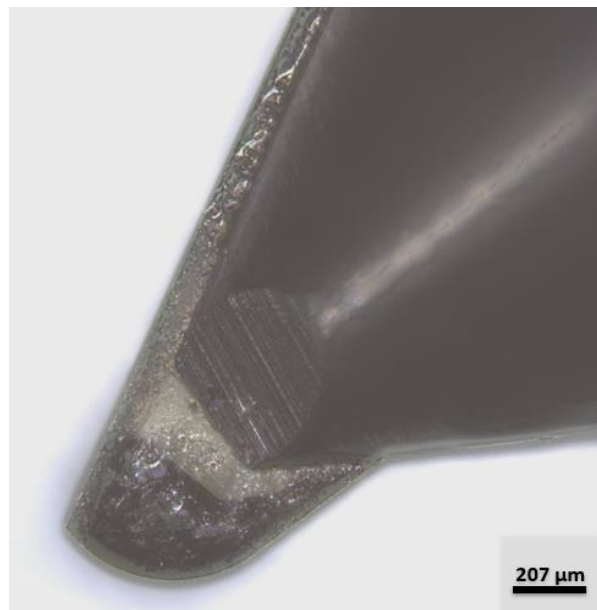


Figure 3.4. *Picture of Single Crystal Diamond cutter having a cutting-edge radius of 500 μm.*

The diamond has a cutting-edge radius of 0.05 μm. Hence, its attainable minimum cutting thickness is 0.05 – 0.2 μm (Yuan, Zhou, and Dong 1996), preventing bumps or burr formation around dimples, which is beneficial for the final roughness and surface finish of the workpiece.

3.2 Dimple Cutting Force Model

Predictive modelling of the machining forces is one mechanism by which the challenges presented in chapter 3.1.3 can be mitigated. Furthermore, comparison of measured machining forces with those predicted by the model can be used to identify issues with patterning the surface, such as issues with uniform cutting, oscillations in the cutter, or tool wear. The performance of textured surfaces depends upon the geometry of the surface patterns.

3.2.1 *Modeling of Cutting Dimple Forces*

Conventional cutting force models for end mills can be modified to predict forces for the inclined end milling technique. Three force components on the milling cutter must be considered to account for the effects of spindle inclination. Inclined cutting of dimples with an end mill is periodic and not continuous as in upright milling, and each flute enters the workpiece surface with a certain frequency. Since the tool geometry of an end mill allows for uniquely shaped dimple geometries, an investigation into how cutting forces are affected is warranted. Using the conventional force model, cutting forces can be identified while the end mill is inclined in local $x'-y'-z'$ coordinates. Afterwards, they can be transformed back through the inclination angle to the global $x-y-z$ coordinate system (E Graham, Park, and Park 2013).

The conventional mechanistic force model (for shearing-dominated cutting) for an end mill determines said forces by calculating the chip thickness and identifying the cutting coefficients (Altintas 2011). The general formula for the chip thickness, h , of a flat end mill is given by equation 3.5.

$$h = f_t \sin(\phi) \quad (3.5)$$

where f_t is the feed rate (*mm/flute*), and ϕ is the tool rotation angle adjusted for the number of flutes and position along the cutting edge.

End mills experience a resultant force comprised of three components in the radial (F_r) tangential (F_t) and axial (F_a) directions. For the shearing-dominated cutting, the elemental components of each force can be expressed as:

$$dF_r = K_{rc} h dz' + K_{re} dz' \quad (3.6)$$

$$dF_t = K_{tc} h dz' + K_{te} dz' \quad (3.7)$$

$$dF_a = K_{ac} h dz' + K_{ae} dz' \quad (3.8)$$

where K_{rc} , K_{tc} , K_{ac} , K_{re} , K_{te} and K_{ae} are the cutting and edge coefficients in each direction, respectively, and dz' is the differential axial height of the cutter. These parameters have been identified experimentally by Malekian *et al*, (Malekian, Park, and Jun 2009).

Surface topography can be predicted analytically by relating tool geometry and machining parameters to the workpiece surface. As shown in Figure 3.5, a cylindrical micro end mill can be modeled as rotating with spindle speed n (rev/min) and moving at feed rate f (mm/s). The tool is inclined at angle γ , has radius R , has N number of flutes, and has a helix angle β (this angle is shown in Figure 3.3). As the tool moves over the workpiece surface, each flute successively cuts a dimple into the material at maximum cutting depth d . The angular direction of feed θ is defined from the x -axis.

For this study, the spindle was inclined about the y -axis in the same direction as the tool feed or x -direction ($\theta=0^\circ$). The equations that relate an inclined ball end mill with the position of the cutting edge to a flat workpiece surface were presented by Matsumura *et al.*, (Matsumura and Takahashi 2011). These equations can be adapted for other end mill geometries as well.

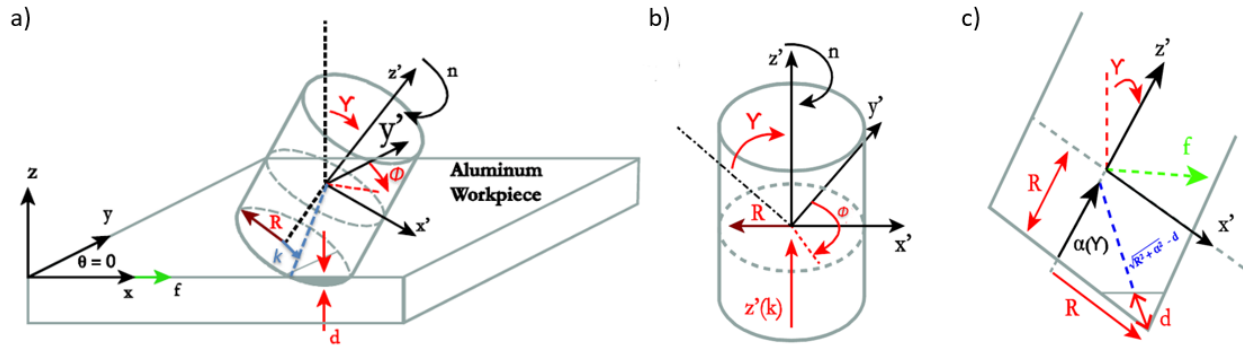


Figure 3.5. Analytic model of a flat end mill. (a) The tool is inclined at angle γ . When the tool moves through the workpiece surface, each flute successively cuts a dimple into the material at cutting depth d . (b) A cylindrical micro end mill can be modeled as rotating element with spindle speed n (rev/min) that moves with feed rate f (mm/s), and the position of a point on the cutting edges can be described in x' - y' - z' coordinates. (c) Knowing a point with distance R from the bottom of the end mill and the top of the end mill at given time t , it is possible to transform this point to global x - y - z coordinates by relating to the cutting depth, inclination of the tool, and feed rate.

The position of a point on the cutting edges can be described in a local x' - y' - z' coordinate system aligned with the cutter axis:

$$x' = R \cos(\phi) \quad (3.9)$$

$$y' = R \sin(\phi) \quad (3.10)$$

$$z' = -(R - z'(k)) \quad (3.11)$$

where ϕ is the immersion angle and is a function of time and rotational speed.

The end mill is comprised of k infinitesimal disks along the axial length starting from the bottom of the cutter, each with width dz' , so that the axial position along the end mill is:

$$z'(k) = kdz' \quad (3.12)$$

Thus, the immersion angle is updated depending upon which flute is cutting and the position along the axial length. The instantaneous immersion angle of each flute is:

$$\phi(k) = \phi - (j - 1)\phi_p - \frac{\tan(\beta_0 * z'(k))}{r} \quad (3.13)$$

where $j=1 \dots N$ is the flute number, and ϕ_p is $2\pi/N$ is the cutter pitch angle.

The radius of the k_{th} disk element r , the axial angle κ , and the local helix angle β_0 change for each disk element with the axial position according to:

$$r = \sqrt{2 * R * z(k) - z(k)^2} \quad (3.14)$$

$$k = \sin^{-1}\left(\frac{r}{R}\right) \quad (3.15)$$

$$\beta_0 = \tan^{-1}\left(\frac{r}{R}\right) * \tan(\beta) \quad (3.16)$$

The origin of the local cutter coordinates is assumed to be distance R from the bottom to the top of the end mill. At given time t , this point can thus be transformed into global x - y - z coordinates by relating to the cutting depth, inclination of the tool, and feed rate:

$$X = R \cos(\emptyset) \cos(\gamma) + \left(\frac{\sqrt{R^2 + \alpha(\gamma)^2} - d}{\cos(\gamma)} - R + z'(k) \right) \sin(\gamma) + f_t \cos(\theta) \quad (3.17)$$

$$Y = R \sin(\emptyset) + f_t \sin \theta \quad (3.18)$$

$$Z = -R \cos(\emptyset) \sin(\gamma) + \left(\frac{\sqrt{R^2 + \alpha(\gamma)^2} - d}{\cos(\gamma)} - R + z'(k) \right) \cos(\gamma) \quad (3.19)$$

$$\alpha(\gamma) = \frac{R}{\tan \gamma} \quad (3.20)$$

where $\alpha(\gamma)$ is the distance shown in Figure 3.5(c) and is dependent on the inclination angle.

Through iterations of the axial position of the cutter, the global coordinates of all points along the cutting edge can be calculated. Knowledge of the relationship between machining parameters and tool geometry allows manufacturers to solve issues such as optimization of tool paths, tool wear, runout, and most importantly, optimizing surface texture to achieve the best performance of the end product (Graham, Park, and Park 2013).

3.3 Cutting Forces Simulation vs. Measured Cutting Forces

Cutting forces are evaluated to determine the effect of machining parameters on tool longevity and efficiency, as well as patterning performance and efficiency. Because accurate modeling is important in order to generate the desired surface patterns without causing tool breakage. Both tool geometry and cutting technique have significant effects on cutting forces and surface finishes (Fontaine et al. 2007). Figure 3.6 shows the simulated machining forces, as well as the forces measured by the table dynamometer resolved into forces, measured in the x -, y -, and z -directions when cutting dimples.

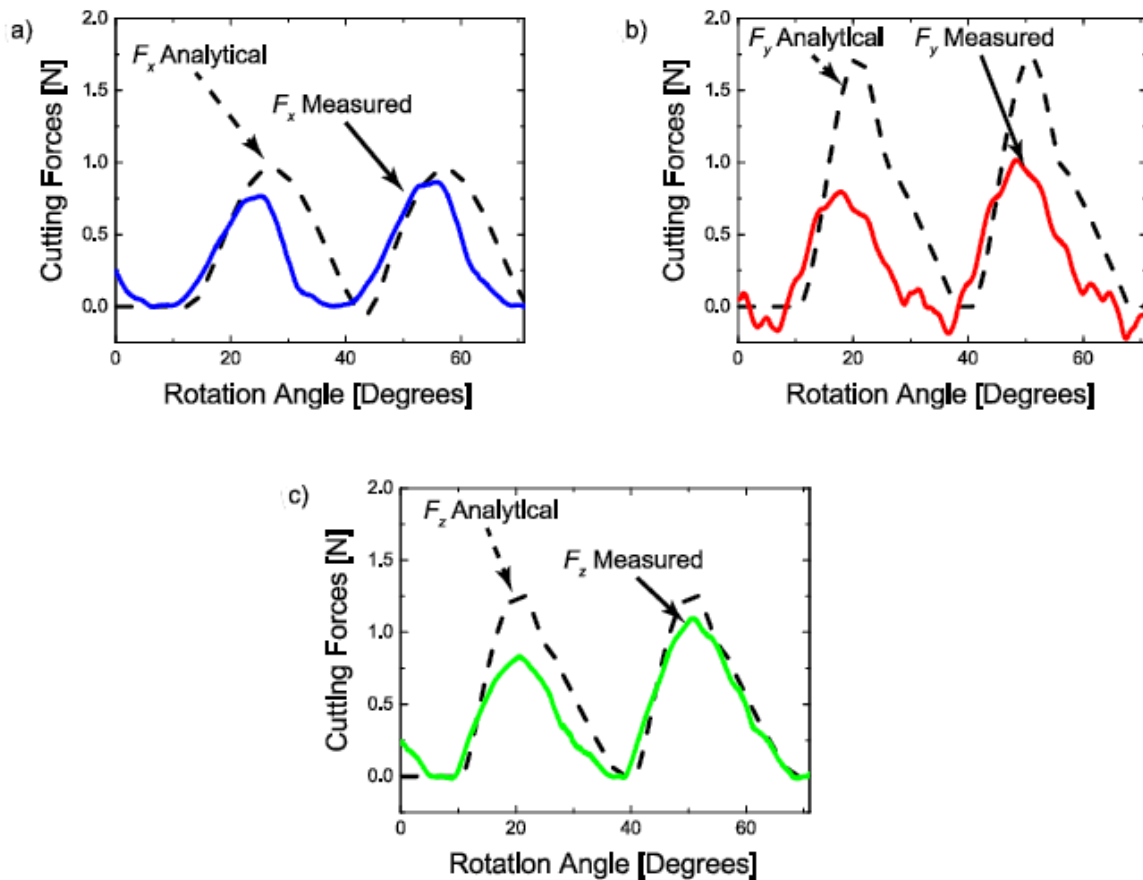


Figure 3.6. Machining forces resolved in the (a) x -, (b) y - and (c) z -axes from both simulations (black dashed line) and measurements (blue, red, and green solid lines, respectively) for inclined flat end milling of the Al6061 workpiece.

Simulated machining forces also used Eqs. (3.9)– (3.11) to achieve analytical profiles of dimple patterns, also revealing the resulting dimple shape and size. Deviations in the force magnitudes observed in Figure 3.6 were likely due to the non-uniform geometry of the cutting tool, tool deflections, or frictional forces on the flank face of the cutting edges due to elastic recovery of material (Bedi, Mann, and Menzel 2003; Fontaine et al. 2007; E Graham, Park, and Park 2013). Figure 3.6 shows that there was a difference between the measured forces and the analytical forces of 17.5% in the *x-direction*, 45.71% in the *y-direction*, and 24% in the *z-direction*. The magnitudes of the measured forces in the *y-direction* and in the *z-direction* indicate that the deflection of the tool may have caused less material to be removed in those directions. It can be observed that the magnitudes of the measured forces oscillate 18%, which corresponds to the slight differences in depth between successive dimples (shown in Figure 3.8).

In an effort to avoid these discrepancies, which result from uneven toolshape, a single crystal diamond cutter was used to create symmetrical dimples (shown in Figure 3.9). Figure 3.7 shows the simulated machining forces, as well as the forces measured by the table dynamometer resolved into the *x*-, *y*-, and *z*-directions when a single crystal diamond was used. Table 3.1 shows the machining parameters used to create both asymmetrical and symmetrical dimples.

Table 3.1. *Machining parameters used to create dimples.*

Tool	Spindle inclination	Spindle speed	Feed rate	Depth of cut
Flat en Mill	60°	500 RPM	5 mm/sec	30 μm
Single crystal diamond	60°	1000 RPM	4 mm/sec	30 μm

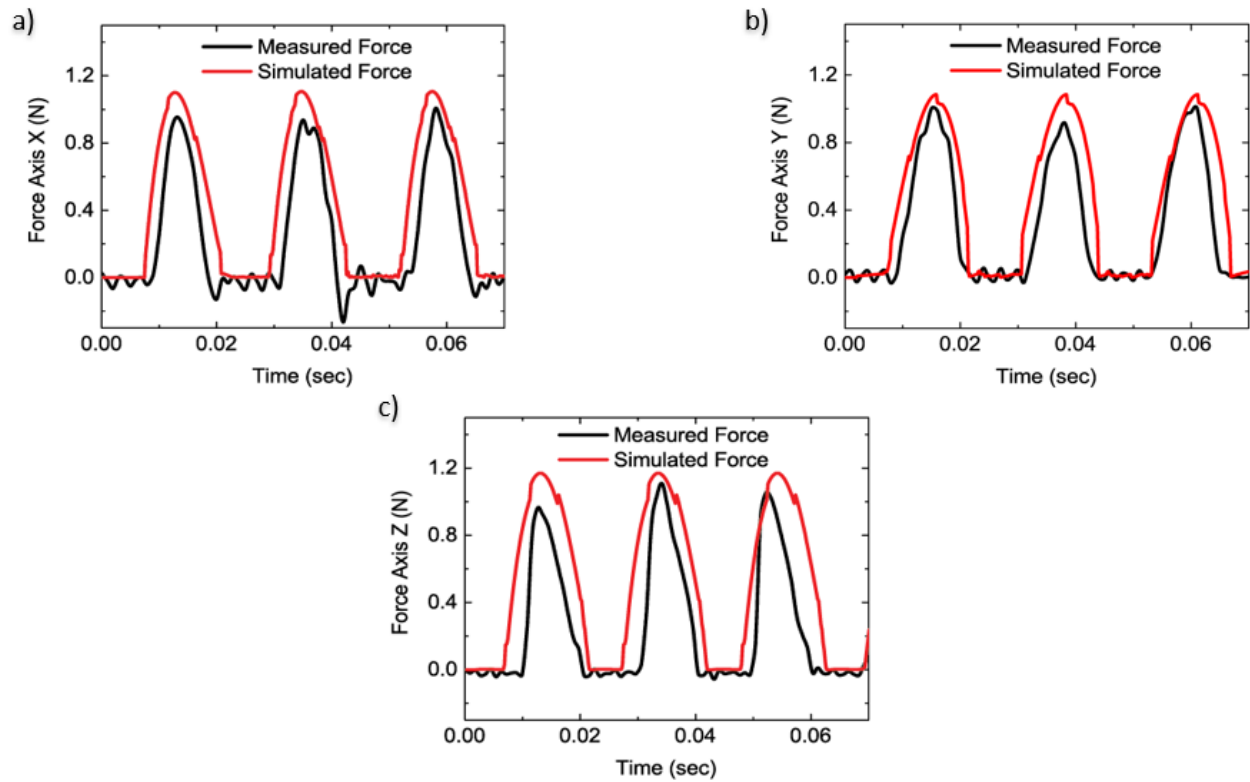


Figure 3.7. Machining forces in the (a) x-, (b) y- and (c) z-axes from both simulations (red line) and measurements (black line) for a single crystal diamond cutter of the Al6061 workpiece.

When the single crystal diamond tool is used, it is observed from Figure 3.7 that discrepancies between simulation and measured forces in the peak of the graphs are not bigger than 9% for all directions. This is because having only one cutter results in no eccentricity, tool deflection, or cutter run-out. Excessive cutting forces in the micromachining process can cause all these problems and lead to tool breakage. Thus, monitoring, measuring and comparing the cutting forces to an analytical model is helpful to increment tool longevity and minimize tool wear to improve surface finishes or in this case, to keep a constant dimple shape. The comparison between the simulated and experimental results relied on the following condition: dimples were machined into the surface when the cutting edge was engaged onto the workpiece surface, which occurred when the z coordinate of a point on the cutting edges was less than zero ($z < 0$).

3.4 Profile of Dimpled Surfaces Produced with Flat end Mill

The influence of the asymmetrically shaped end mill that produced the force variations in Figure. 3.6 can also be seen in Figure. 3.8. When observing the dimples from left to right in Figure. 3.8, the second dimple had a slightly smaller depth (by approximately $5\mu\text{m}$), as shown in Figure 3.8(b). Figure. 3.8(a) shows the measured topographic profile of the dimpled surfaces produced at a constant spindle inclination angle of 60° . Figure 3.8(b) shows the dimples profile.

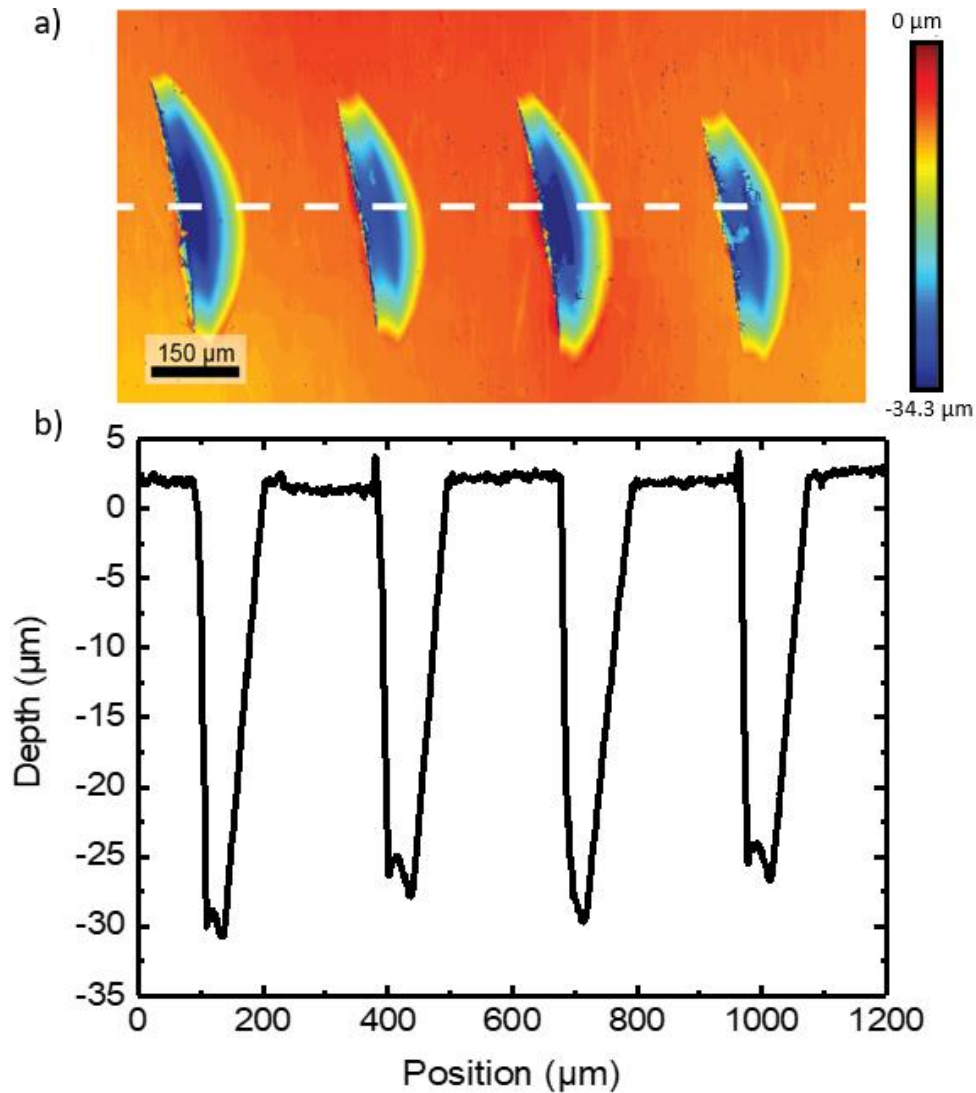


Figure 3.8. (a) Three-dimensional topographic image of the dimpled surfaces produced on the AL6061 workpiece using a flat end milling. The white dashed line indicates the place where the line profile shown in (b) was taken. The dimple geometry was produced at a tool incline of 60° , a feed rate of 5.0 mm/s , and a spindle speed of 500 rpm .

A close examination of Figure. 3.8(b) shows that the dimpled patterns had a depth of approximately 30 μm with the aforementioned machining parameters, which was significantly higher than the average surface roughness ($0.11\pm 0.02 \mu\text{m}$). The size of the dimples in comparison to the surface roughness was also evident by the flatness of the surface surrounding the dimples in these topographic images.

3.5 Profile of Dimpled Surfaces Produced with Single Crystal Diamond Cutter

Diamond is becoming a very important material for machining operations in the recent decades due its physical and chemical properties (C. Chang *et al.* 2003). These properties have been discussed in section 3.1.4. In order to compare the tribological properties of different dimple shapes, a Single Crystal Diamond cutter was used to machine a series of dimples at an inclination angle of 60° with a feed rate of 4 mm/sec., as indicated in Table 3.1. The cutting influence of the single diamond cutter can be seen in Figure 3.9.

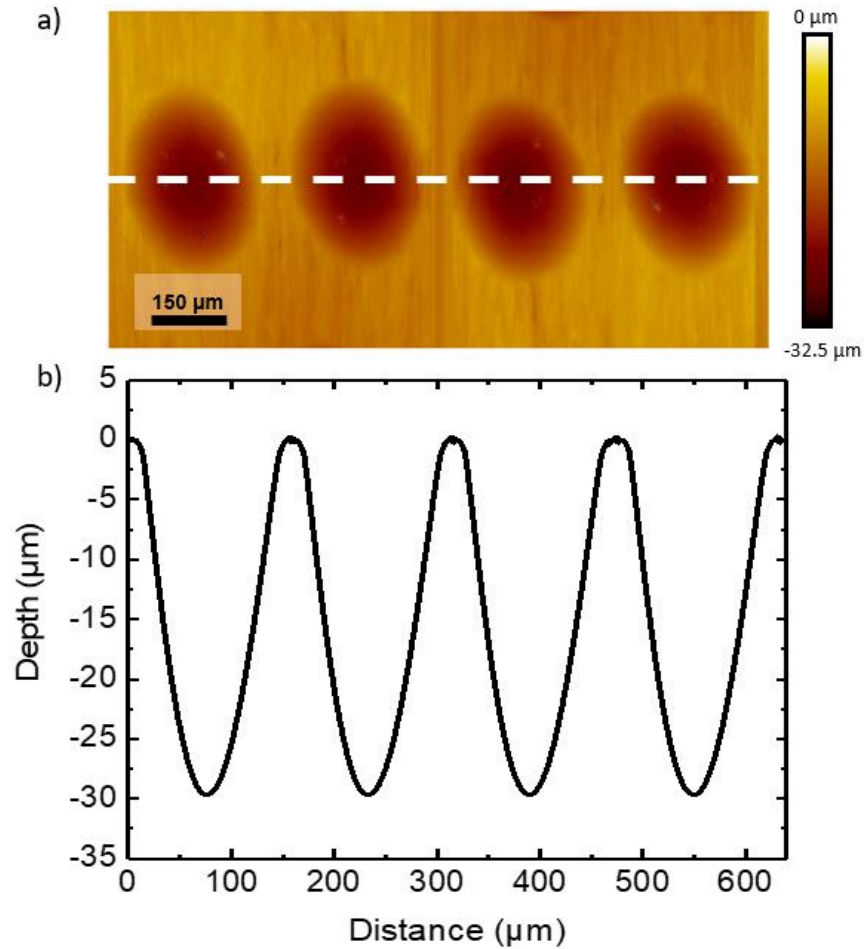


Figure 3.9. (a) Three-dimensional topographic image of the dimpled surfaces produced on the AL6061 workpiece using a single crystal diamond cutter. The white dashed line indicates the place where the line profile shown in (b) was taken. The dimple geometry was produced at a tool incline of 60° , a feed rate of 4.0 mm/s, and a spindle speed of 1000 rpm.

Figure 3.9(a) shows a topographic profile for dimples machined with a Single Crystal Diamond. A close examination of Figure 3.9(b) shows that the dimpled patterns had a depth of approximately 30 μm . When observing the dimples profiles from Figure 3.9 (b), there is no evident difference in depth between successive dimples. The pitch of the dimples in Figure 3.9 is about 150 μm (a deeper analysis of the pitch effect is presented in Chapter 5), showing that the hydrodynamic pressure for dimples with a depth of 30 μm having a pitch of 350 μm is 60% higher compared with dimples having a depth of 30 μm and a pitch of 150 μm . Thus, a pitch of 350 μm was chosen for machining dimples, as shown in Figure 3.10.

3.6 Profile of Multi-scaled Textured Dimpled Surfaces through a High-Velocity Abrasive Machining Process

To gain insight into the effects of micro-roughness and its consequences on lubrication, a multi-textured process was carried out on both a flat and a dimpled surface using a High-Velocity Abrasive Machining process. An optical image of the surface of the workpiece after dimples were cut into it with the diamond cutter is shown in Figure 3.10 (a). The optical image shows that the dimples are circular and approximately 75 μm in radius. Figure 3.10 (b) shows the line profile taken from red dashed line in the optical image (Figure 3.10(a)) showing that the dimples have been cut 30 μm below the flattened surface. This cutting process resulted in the creation of surface textures having an aspect ratio (depth/diameter) of 0.2, which is comparable to the aspect ratio that has been shown to significantly improve friction coefficients in previous studies (Greiner *et al.* 2015; Greiner and Schäfer 2015; B. Zhang *et al.* 2013). A topographic image of a dimpled surface after a multi-textured process is shown in Figure 3.11 (a). This image shows a significant change in the surface topography compared to the dimpled surface. Figure 3.11 (b) shows a line profile through the dimples, indicating that the height of the dimples remained roughly the same as before they were hard shot blasted. The surface roughness was also measured on the flat surfaces that had been multi-textured and was observed to be $0.33 \pm 0.02 \mu\text{m}$, an increase of 88% from the flat surfaces. This increment in roughness affected the wetting properties of the surface, as shown in section 4.2.

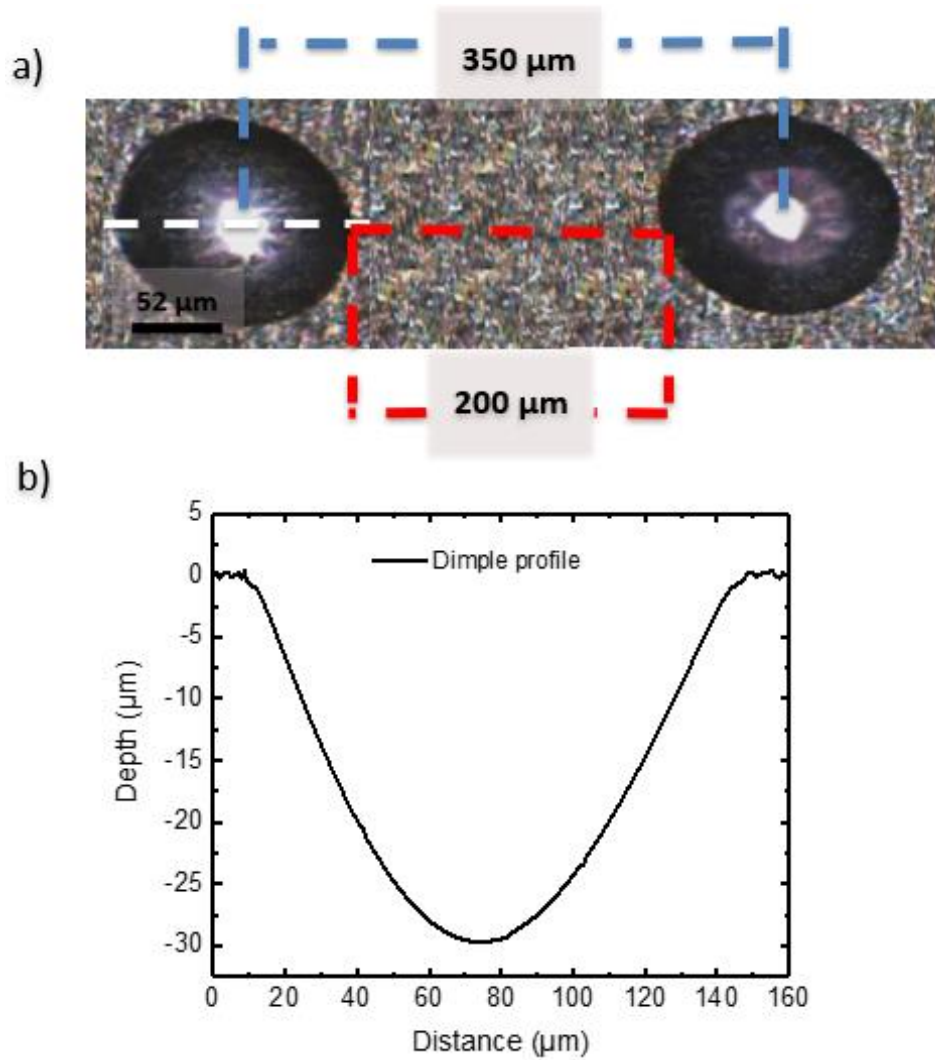


Figure 3.10. (a) Plan view optical microscopy image of the dimpled surface. Dimples were observed to be circular. Pitch between dimples is 350 μm . Flat surface between dimples is 200 μm . (b) Line profile of the height of the dimples taken through the white dashed line in (a) indicating that the dimples have a height of approximately 30 μm .

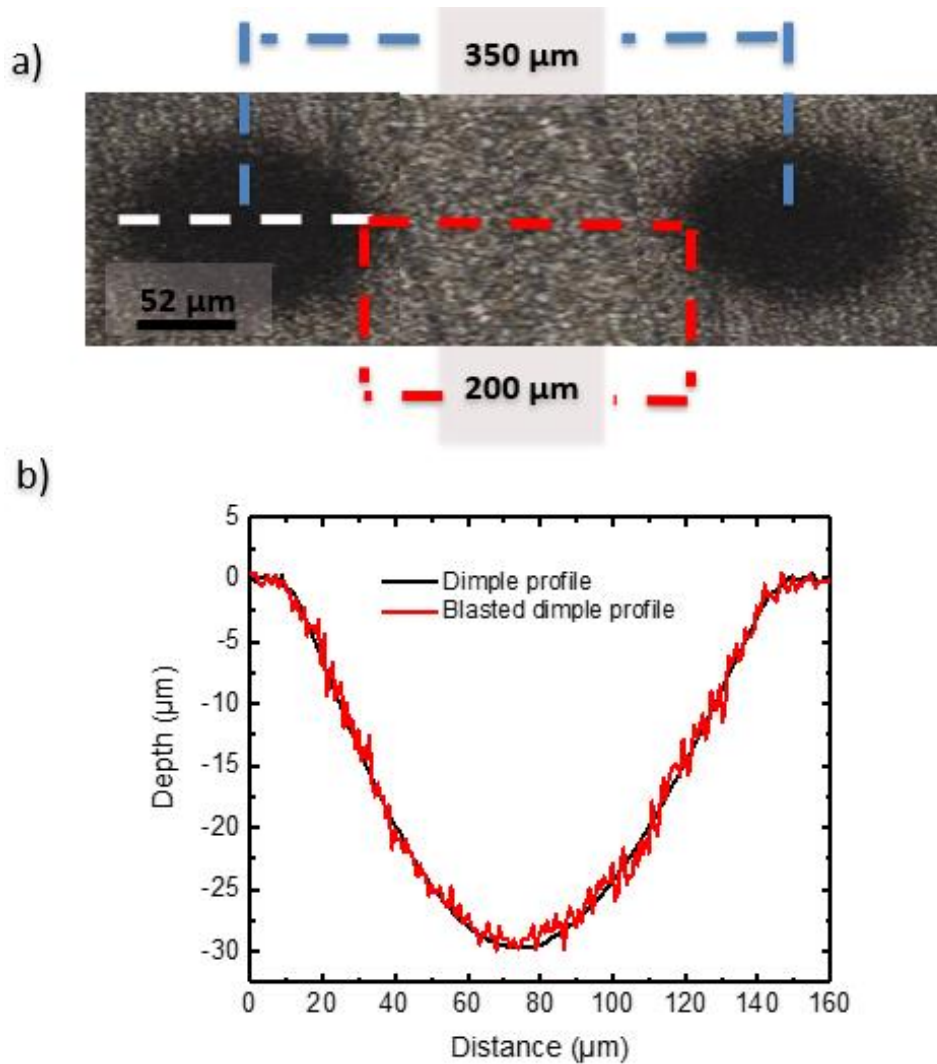


Figure 3.11. (a) Plan view optical microscopy image of the dimpled surface after shot blasting. Pitch between dimples is $350\ \mu\text{m}$. Flat blasted surface between dimples is $200\ \mu\text{m}$. (b) Line profile of the height of dimples taken through the white dashed line in (a) indicating that the dimple height remains relatively unchanged as a result of shot blasting. A grain size of $10\ \mu\text{m}$ with the nozzle at normal position (90°) was used to blasting dimples for 10 seconds to prevent erosion on the textured surface, as indicated in section 4.5.

3.7 Summary

In this section, parameters such as tool geometry, depth of cut, feed rate, and spindle speed were presented. These parameters define the dimple geometry. By increasing the feed rate or decreasing the spindle speed, the tooth passing rate becomes smaller and the spacing between dimples becomes larger, resulting in fewer dimples per row. In contrast, decreasing the feed and

increasing the spindle speed will result in more closely packed dimples. Higher spindle speed and lower feed rates will result in a higher density of dimples, while lower spindle speeds and higher feeds will have the opposite effect.

Force modeling of machining operations is central to understanding how to improve efficiency and understand the process. Comparison of measured machining forces with those predicted by modelling can be used to identify issues with patterning the surface, such as issues with uniform cutting, oscillations in the cutter, or tool damage. The performance of textured surfaces depends upon the geometry of the surface patterns.

Machining forces were acquired by attaching samples on a piezoelectric table dynamometer. Posterior analysis of these forces with simulated ones showed the validity of the analytical model describing the machining forces and showed that the peak forces measured in alternating cuts were slightly higher than in the cut directly beforehand, suggesting that the flat end mill was not completely symmetric.

CHAPTER 4. HIGH VELOCITY ABRASIVE MACHINING

Surface roughness can affect lubrication in many different ways. For example, surface roughness can disturb the process of the building-up of pressure in the oil film, especially at the inlet of the lubricated contact. It has been shown that increased surface roughness requires an increase in the oil film thickness in order to avoid contact between the asperities (Lundberg 1995). In this section, the benefits of the incremental roughness on surfaces by High Velocity Abrasive Machining (HVAM) was considered and analyzed through the contact angle (CA) and contact angle hysteresis (CAH) of those surfaces and a water droplet. HVAM uses a stream of fine-grained abrasive particles propelled by highly pressurized air through a nozzle. Factors such as injection pressure, abrasive particle size, density, stand-off distance, and nozzle inclination affect the results of the multi-textured process (Jang, Cho, and Park 2008). However, this technique can cause an erosion on workpieces.

4.1 Wetting Effects on Multi-textured Surfaces

Wetting (defined as the ability of liquids to form interfaces with solid surfaces) is characterized by the CA, which is the angle between the solid and liquid surfaces. If the liquid wets the surface, the value of the contact angle is $0^\circ < \theta_0 < 90^\circ$ (referred as hydrophilic surfaces), whereas if the liquid does not wet the surface, the value of the contact angle is $90^\circ < \theta_0 < 180^\circ$ (referred as non-wetting or hydrophobic surfaces) (Jung and Bhushan 2006). CA depends on several factors, such as roughness and surface cleanliness (Nosonovsky and Bhushan 2006). It has been demonstrated that the roughness of a surface can affect the tribological properties of those

surfaces (Nosonovsky and Bhushan 2007; Pawlak, Urbaniak, and Oloyede 2011; Belaud et al. 2015).

The wetting degree (wettability) is the ability of a liquid to maintain contact with a solid surface, and it is determined by a force balance between the intermolecular interactions of the adhesive type (liquid to the surface) and cohesive type (liquid to liquid). Wettability produces a continuous fluid film capable of isolating and carrying loads between two sliding surfaces. Normally, the smaller the CA of a droplet on a sliding surface, the better the lubrication is and the lower the friction coefficient is (Pang, Liu, and Liu 2017). The CAH reflects the irreversibility of the wetting/dewetting cycle, it is a measure of energy dissipation during the flow of a droplet along a solid surface. The CA and the CAH are two parameters which characterize the hydrophobicity/hydrophilicity of a solid surface. Experimental CA resulting from blasted surfaces are shown in Figure 4.5 and CAH results are shown in Figure 4.7.

4.2 Roughness Effects on Hydrophobic and Hydrophilic Surfaces

Hydrophobic surfaces with very low droplet adhesion are found on the leaves of many plants, most famously the lotus (as in the “lotus effect”). There also exist surfaces, such as the red rose petal, that exhibit hydrophobicity with high droplet adhesion (“petal effect”) (Ebert and Bhushan 2012). One of the ways to increase the hydrophobic or hydrophilic properties of the surface is to modify the surface roughness (Nosonovsky and Bhushan 2006), considering the R_{sk} (skewness) and the R_{ku} (kurtosis) roughness parameters. R_{sk} measures the symmetry of the variation in a profile about its mean line. Thus, R_{sk} is sensitive to occasional deep valleys or high peaks in the profile. R_{ku} describes the probability density sharpness of the profile, as shown in Figure 4.1. Surfaces with relatively few high peaks and low valleys are reflected in a kurtosis of

less than 3, whereas a kurtosis value of more than 3 indicates many high peaks and low valleys (Sedlaček, Gregorčič, and Podgornik 2017).

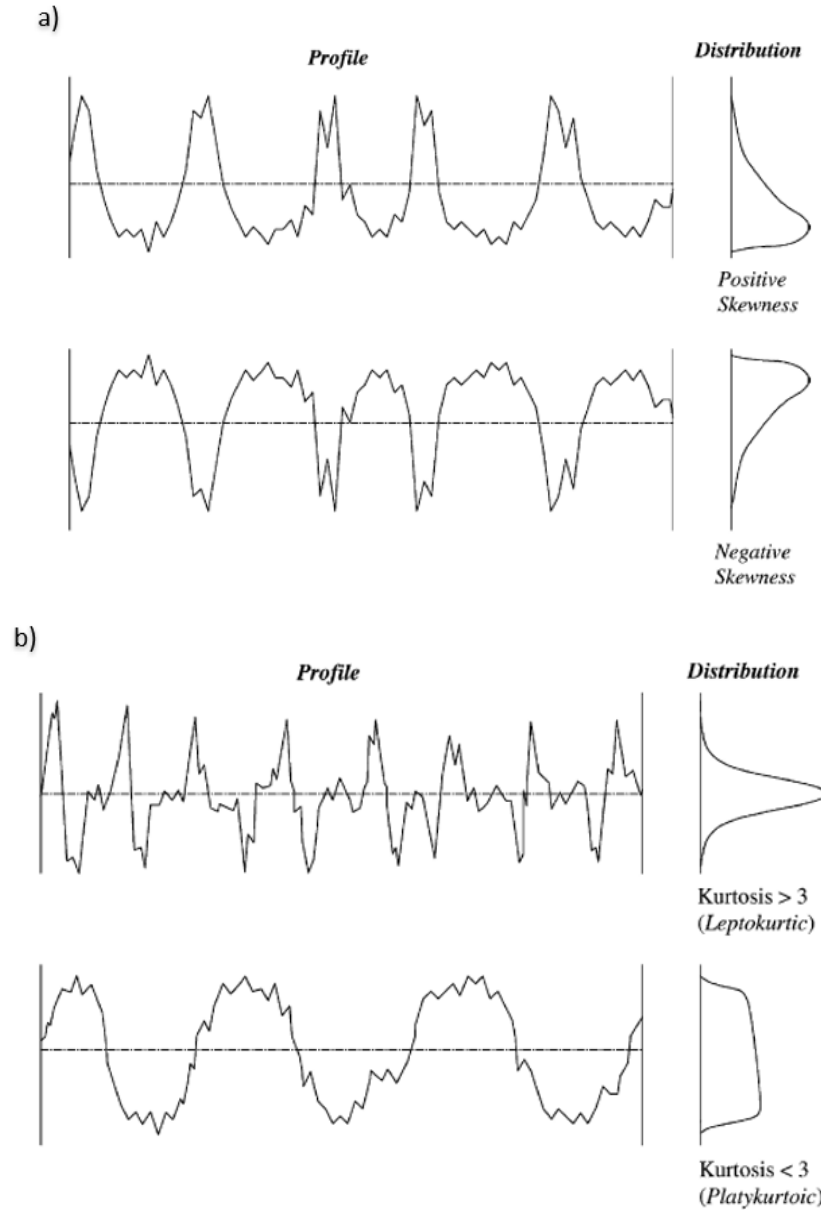


Figure 4.1. Schematic representation of roughness profiles for (a) positive and negative skewness (R_{sk}) and (b) kurtosis (R_{ku}) lower and higher than 3 (Gadelmawla et al. 2002)

As reported by Sedlaček et al. (Sedlaček, Gregorčič, and Podgornik 2017), a change in surface topographies leads to a decrease of friction. This is because plateau-like topographies with

small cavities can supply lubricant into the contact, similar to surface texturing. Thus, a higher kurtosis (R_{ku}) and a more negative skewness (R_{sk}) result in lower friction in the boundary and mixed lubrication regimes. Also, when the roughness of a solid surface increases beyond a certain level, the system enters a regime in which the liquid does not penetrate into the troughs (Nakajima et al. 2000). Figure 4.4 shows an optical microscopic image of a flat surface, and two blasted surface when a blasting powder having 10 μm size and 50 μm were used, indicating the change in R_{ku} and R_{sk} roughness.

4.3 Creation of multi-textured surfaces

A multi-texture process through the HVAM technique is used for the development of surfaces with a smaller scale of roughness that could be achieved with end mill dimple patterning. This technique shows a high machining versatility, high flexibility, and small cutting forces (Çaydaş and Haşçalık 2008). In addition, it provides a high level of surface finish and close geometric tolerances with an economically acceptable rate of surface generation for a wide range of industrial components (Jain, Jain, and Dixit 1999).

In this research, a shot blasting process was carried out to analyze the effect of blasting particles on a flat aluminum 6061-T6 surface (50 x 50 x 25 mm) using a different nozzle inclination angle and varying the exposure time and shot blasting grain size. An abstract with the parameters used is shown in Table 4.1. First, the surface roughness of the workpieces was measured using the samples without a blasting process, $R_a = 0.10 \pm 0.02 \mu\text{m}$. In the second phase, blasting was carried out on the flattened aluminium surfaces by a micro-abrasive blaster (COMCO ProCenter™) under high mean abrasive aluminum oxide. According to the manufacturer's label, the aluminium oxide micro-abrasive particle powders had sizes of 50 μm (PD 1035-2) and 10 μm (PD 1029-4).

During the blasting process, an air pressure of 0.4 MPa and a nozzle having a diameter of 0.75 mm were used. The nozzle inclination angles (α) employed varied from 30° to 90°, having an exposure time of 10 sec., 30 sec. and 60 seconds for all the cases. Figure 4.2 shows a schematic of the blasting technique used. The nozzle was attached to a rotating mount and a manual stage while holding the nozzle to target a constant standoff distance (h) from the aluminium surface at 1.5 cm.

Table 4.1. HVAM texturing parameters used in this research. Two different micro-abrasive powders were used, 10 μm PD1029-4 and 50 μm PD 1035-2. Angle of incidence and test duration were varied.

Grain size 10 μm	Grain size 50 μm
Angle of incidence 30°, 60°, 90°	Angle of incidence 30°, 60°, 90°
Test duration 10 s, 30 s, 60 s	Test duration 10 s, 30 s, 60 s

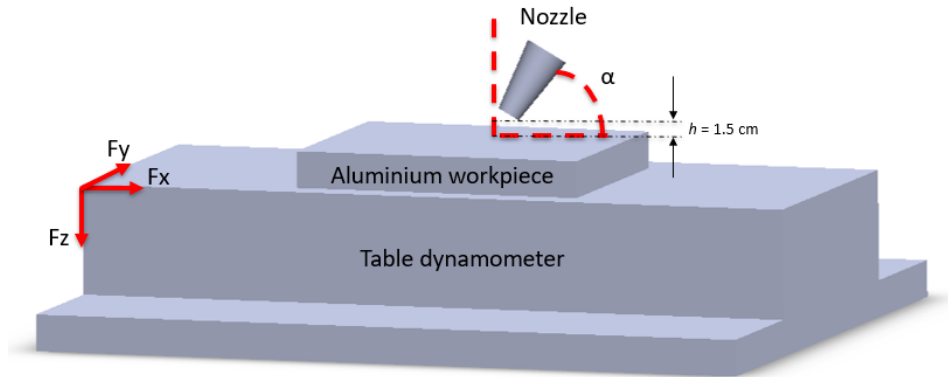


Figure 4.2. Schematic showing the inclination of the nozzle relative to the workpiece allowing for the shot blasting process. Nozzle inclination (α) varied from 30°, 60° and 90°.

After the blasting process, the excess of sand was removed with deionized water. Finally, the surface profile after the blasting process was analyzed by optical profilometry (Zeta-20 optical profiler). Figure 4.3 shows the blasting grain shape for both sizes, 10 μm and 50 μm , respectively.

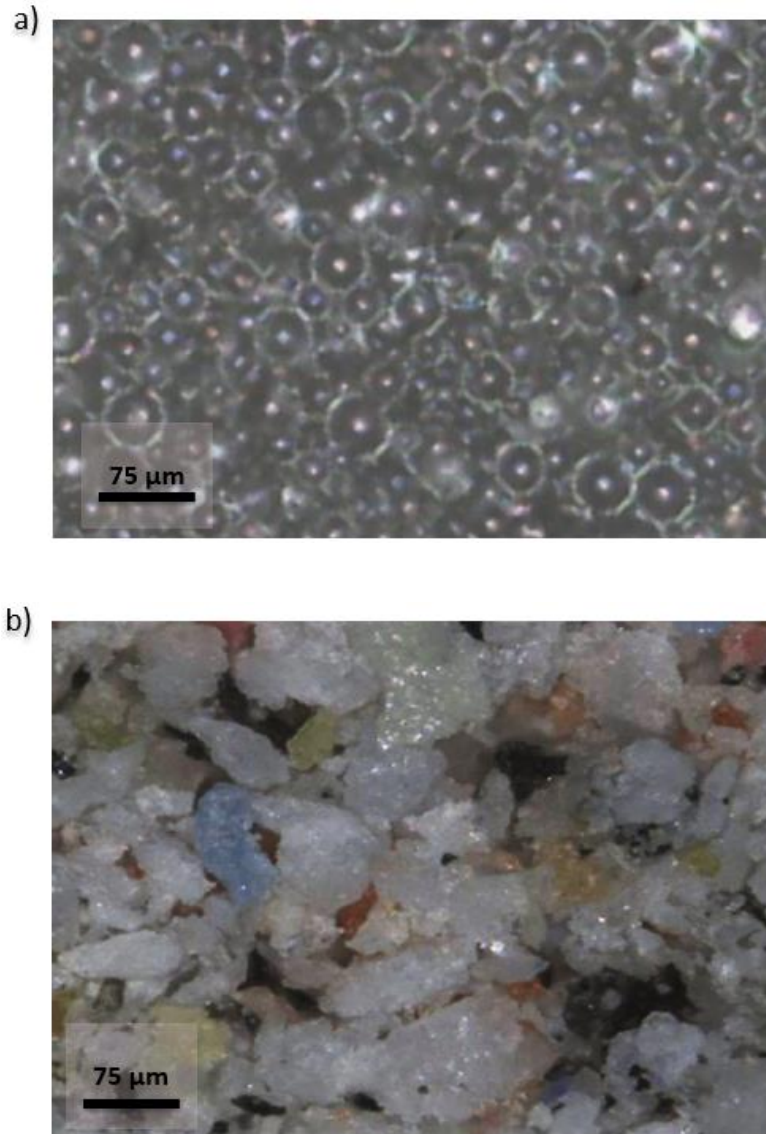


Figure 4.3. *Shape of the micro abrasive powder used in this research. (a) 10 μm PD 1029-4 powder. In this case a circular shape is clearly defined. (b) 50 μm PD 1035-2 powder. An angular powder shape can be observed in this case.*

From Figure 4.3 it is observed that the 10 μm glass bead powder has a spherical shape, while the 50 μm plastic media powder looks like angular flakes. Both kinds of particles can cause an erosion effect on the surface. It has been reported by Oka et al (Oka, Okamura, and Yoshida 2005) that the spherical powder can rotate and cause erosion. The time of impact with some

unbalanced forces can act on the angular-shaped particles, causing a rotating effect and erode surfaces (Deng, Bingley, and Bradley 2004). Also, frictional forces between the surface and the particle may create a crater, as reported by Ruff et al (Ruff and Wiederhorn 1979). Section 4.5 analyzes the erosion effects.

In addition, changes of the textured surface were measured by optical profilometry, allowing for the measurement of the roughness of the textured surfaces using the dimensionless R_{sk} and R_{ku} roughness parameters. Figure 4.4 (a) shows a flat surface, Figure 4.4 (c) shows a textured flat surface (a 10 μm powder size was used) for 10 secs. with the nozzle in normal position. Figure 4.4 (e) shows a textured flat surface (a 50 μm powder size was used) for 10 secs. with the nozzle in normal position. Figure 4.4 (b), Figure 4.4 (d), and Figure 4.4 (f) show the profile of each surface; flat, textured with a 10 μm powder size, and textured with a 50 μm powder size, respectively.

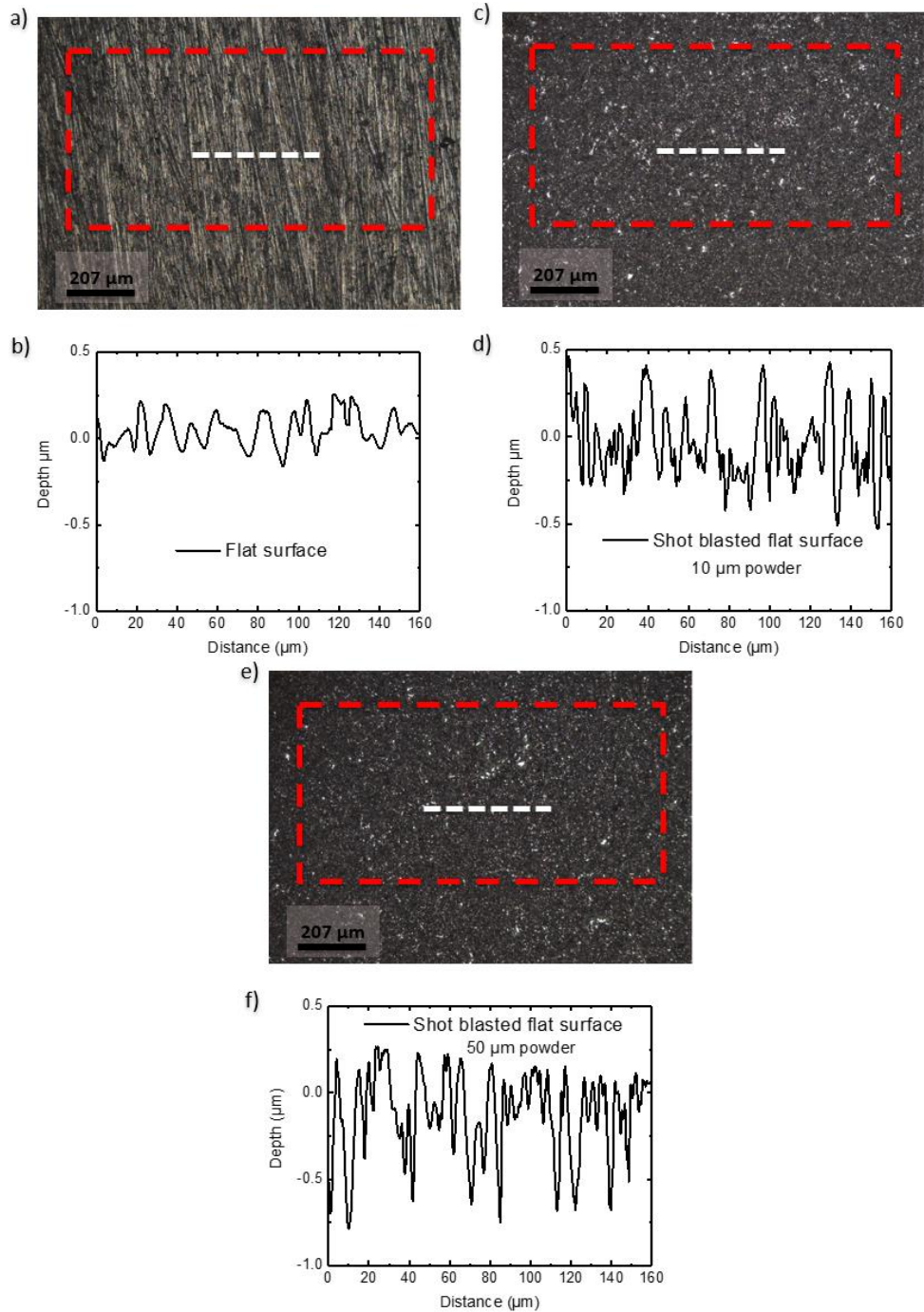


Figure 4.4. Optical profilometry of (a) a flat surface, having a R_{sk} value of 1.5848 ± 0.001 , with a R_{ku} of 2.002 ± 0.001 (c) a flat surface blasted with $10 \mu\text{m}$ grain size during 10 secs., having a R_{sk} value of -2.015 ± 0.001 , with a R_{ku} of 4.021 ± 0.001 (e) a flat surface blasted with $50 \mu\text{m}$ grain size during 10 secs., having a R_{sk} value of -1.014 ± 0.001 , with a R_{ku} of 2.872 ± 0.001 . Rectangles in red colour shows the area where the R_{sk} and R_{ku} roughness values were measured. The dotted white lines show the location where the profile of (b) a flat surface, (d) a flat surface blasted with $10 \mu\text{m}$ grain size and (f) a flat surface blasted with $50 \mu\text{m}$ grain size were obtained.

From Figure 4.4, it is clear that blasting causes a change in the roughness of the aluminium surfaces used in this research. R_{sk} roughness changed from a value of 1.5848 (for the flat surface) to a value of -2.015 when a blasting powder having 10 μm size was used, and to a value of -1.014 when a blasting powder having a size of 50 μm was used. For the R_{ku} roughness, the flat surface changed from a value of 2.002 (for the flat surface) to 4.021 and 2.872 when a blasting powder having 10 μm size and 50 μm were used, respectively. According to Sedlaček et al. (Sedlaček, Gregorčič, and Podgornik 2017), a more negative R_{sk} value and a higher R_{ku} value result in lower friction. Thus, the flat surface blasted with 10 μm powder size will have a lower friction coefficient compared with a flat surface (this is going to be demonstrated in Chapter 6).

4.4 Contact Angle (CA) and Contact Angle Hysteresis (CAH)

To further study the surface properties of the blasted surfaces, CA and CAH effects were investigated using a SmartDrop device. As mentioned in section 4.1, a liquid wets the surface if the CA is less than 90° . Figures 4.5 (a) and 4.5 (b), show the measured CA of blasted surfaces when a 10 μm and a 50 μm powder size were used. A $\sim 5 \mu\text{l}$ water droplet was used for both the CA and CAH measurements. To avoid the effects of gravitational effects on the drop (which would flatten the drop) a drop volume of 2–8 μL is used in contact angle experiments (Erbil 2014). CA and CAH were measured at ten different points. During these experiments, the surface was tilted at an angle (θ) while a high-speed camera captured images of the water droplet; the final CA and CAH used for the comparison of different samples was the average of the left and right angles of each drop.

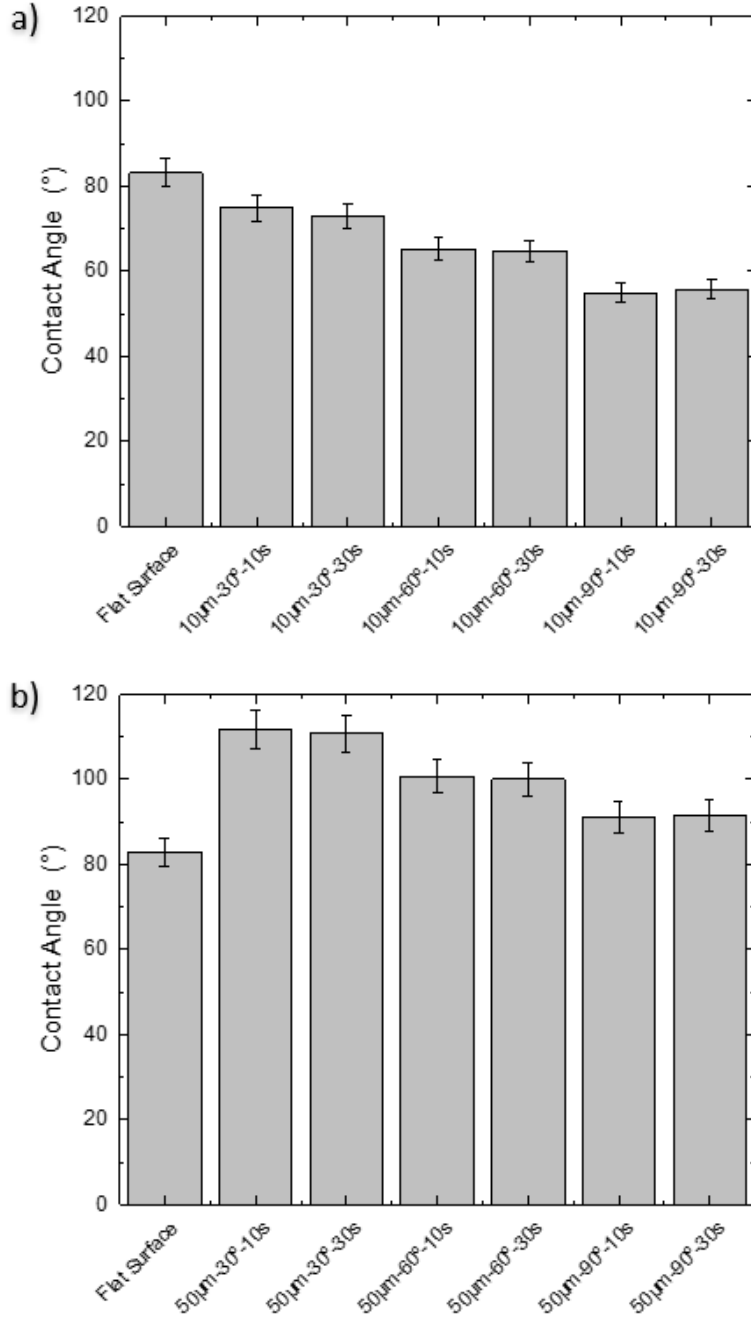


Figure 4.5. Contact angle of a blasted flat surface using (a) 10 μm grain size with an inclination angle of 30°, 60° and 90° during 10 sec. and 30 sec. compared with a flat surface. (b) 50 μm grain size with an inclination angle of 30°, 60° and 90° during 10 sec. and 30 sec. compared with a flat surface.

Results shown in Figure 4.5 indicate that the flat surface has a CA around 90°. When the 10 μm powder size was used the CA has values going from 75° to 55° corresponding to nozzle

inclinations from 30° to 90°. Comparing with a flat surface the CA increased at least 10% after blasting the surfaces using a 50 µm powder size when the nozzle inclination was 90°. When the nozzle inclination was 30° the increment in CA was about 22%, thus going from 90° to more than 110°. The drop-in contact angle value in the roughness range is associated with droplet spreading along the grooves. Values less than 90° are beneficial to wet the surfaces. Even small changes in surface roughness can lead to better wetting properties; for example, in lubricated contacts, such a surface texture can act as a reservoir of lubricant (Kubiak et al. 2011). In order to verify the effects of these changes, a CAH measurement was also carried out. Results are presented in Figure 4.7.

CAH is another important characteristic of a solid-liquid interface. It is the difference between the contact angle at the increased droplet volume (advancing contact angle, θ_{adv}) and the contact angle at the decreased droplet volume (receding contact angle, θ_{rec}) for a droplet on a solid surface as shown in Figure 4.6.

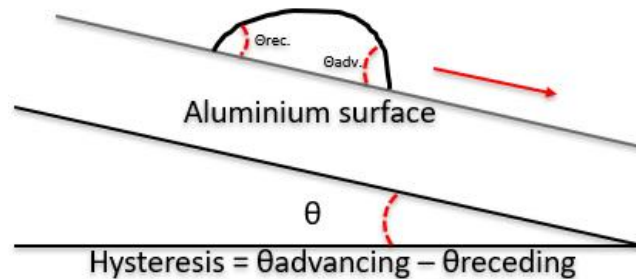


Figure 4.6. Schematic of the calculation of contact angle hysteresis.

CAH denotes the angle to which a surface may be tilted for roll-off of liquid drops. A low CAH results in a very low liquid roll-off angle and implies a low adhesion and friction (Bhushan and Kyu Her 2010). Chemical interactions, interfacial energy, and roughness can affect the CAH (Kijlstra, Reihls, and Klamt 2002; Kubiak *et al.* 2011; Bico, Thiele, and Quéré 2002). Figure 4.7 shows the CAH results for blasted grain sizes of 10 µm and 50 µm, at different nozzle inclination

during 10 secs., 30 secs., and 60 secs. A Stribeck curve showing the effects on friction of this textured surfaces is presented in Figure 6.10.

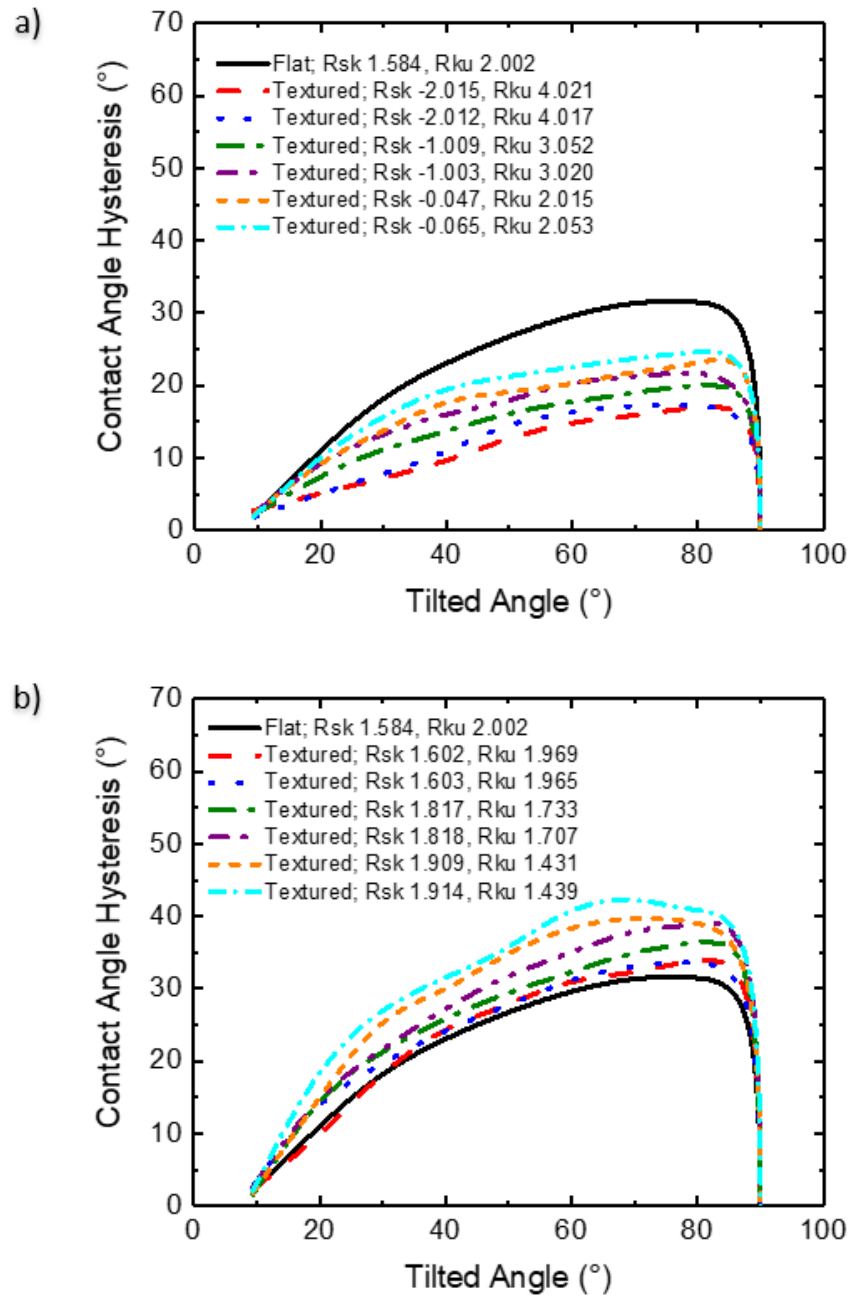


Figure 4.7. Contact angle acquired with a SmartDrop device. (a) Shows results for a 10 μm powder, at different time applications and nozzle inclination. A higher value of R_{ku} and more negative R_{sk} lead to a smaller CAH. (b) Shows results for a 50 μm powder, powder, at different time applications and nozzle inclination. A smaller value of R_{ku} and higher R_{sk} lead to a bigger CAH.

In order to separate the effect of roughness from that of wettability, the surfaces used in this study were polished to obtain smooth surfaces ($R_a = 0.10 \pm 0.02 \mu\text{m}$, $R_{sk} 1.584 \pm 0.001$, $R_{ku} 2.002 \pm 0.001$) using T401 grit sandpaper. Figure 4.7 (a) shows that there is a decrease of 50% (when compared with a flat surface) in the CAH, when the nozzle was at the normal position and grain size of $10 \mu\text{m}$ was used. For the case of a nozzle inclination of 60° , there was a 37% decrease in the CAH, while for a nozzle inclination of 30° the decrease in CAH was only 20%. A decrease in the CAH can cause a lower adhesion and friction (Bhushan and Kyu Her 2010). On the other hand, when the grain size of $50 \mu\text{m}$ was used, the CAH was higher for all the surfaces (when compared with a flat surface). There was an increase of 5% when the nozzle was at the normal position, 22% at a nozzle inclination of 60° , and an increase of 37% at a nozzle inclination of 30° . An analysis of how these results affect the friction coefficient is shown in section 6.3.1

4.5 Erosion Rate

The erosion process is caused by the interaction of solid microparticles. According to Vite-Torres *et al.*, (Vite-Torres et al. 2013), two types of behaviour are shown in solid particle erosion: ductile (where the material is removed due to cutting and ploughing action) and brittle fracture (characterized by the formation of cracks and fractures on the material surface). Some researchers have concluded that the contact angle of microparticles and exposure time have an impact on the erosion rates and thus on the mechanical efficiency of the studied surfaces (D. S. Park, Cho, and Lee 2004; D. A. Lyn, S. Einav, W. Rodi 2000). Figure 4.1 shows both the simulated and the measured erosion rate of aluminium workpieces. Different erosion tests were conducted, the first one using an abrasive micro- abrasive particle PD 1035-2 plastic media ($50 \mu\text{m}$ powder size) and the second one using an aluminum oxide micro-abrasive particle powder COMCO PD1029-4 ($10 \mu\text{m}$ powder size). All tests were performed at a 30° , 60° , and 90° nozzle inclination for 60, 30 and

10 seconds. Simulations were carried out considering Equation 4.1, proposed by Ally *et al.* (Ally, Spelt, and Papini 2012).

$$E_r = (\sin\alpha)^{n_1}(1 + H_V(1 - \sin\alpha))^{n_2} \quad (4.1)$$

where H_V is the nominal Vickers hardness of the target in GPa, α is the nozzle inclination and the parameters n_1 and n_2 are constants that depend on the material used (for aluminium 6061-T6 they are 1.34 and 4.59, respectively).

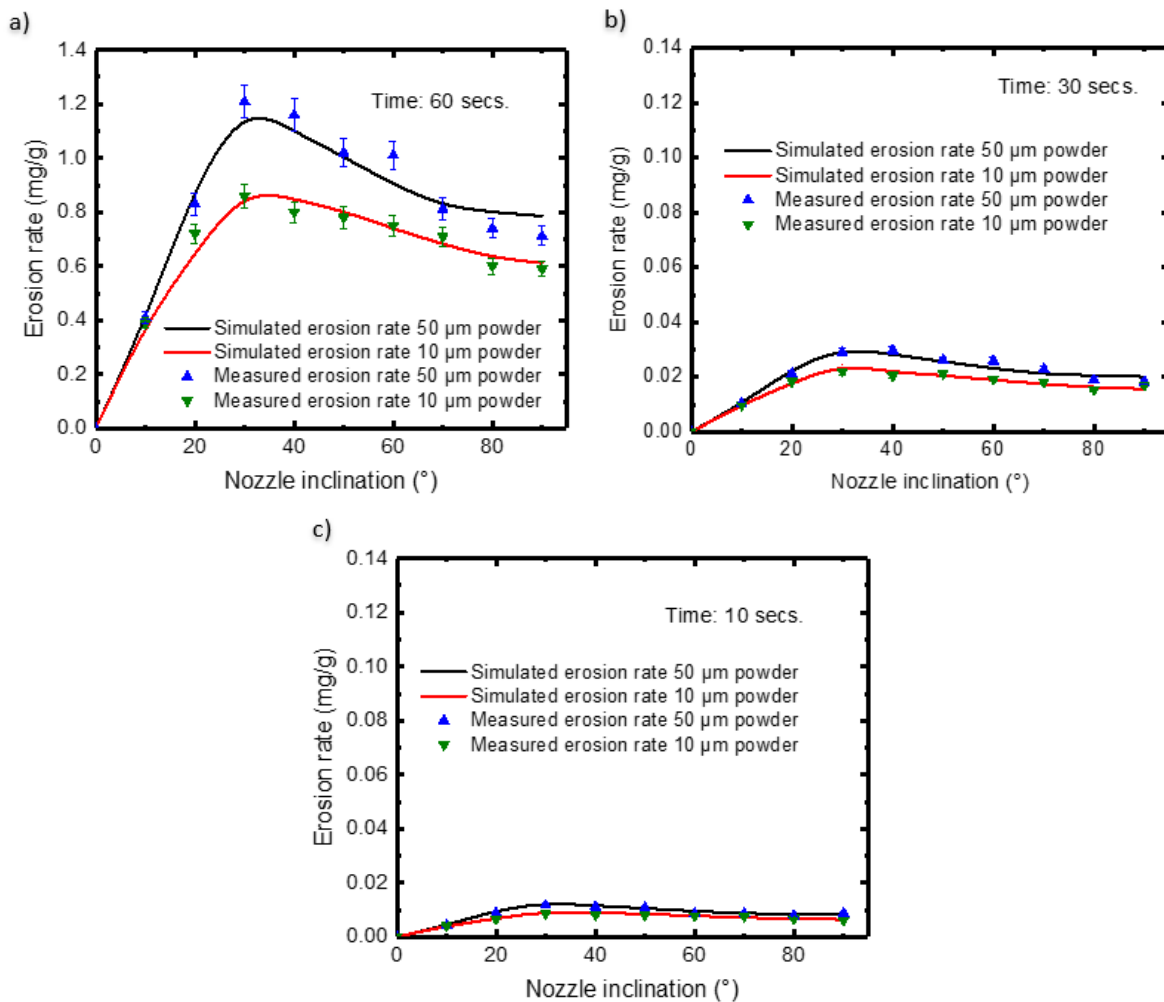


Figure 4.8. Erosion rate of Aluminium 6061-T6 by 50 µm and 10 µm aluminium oxide micro particles at a velocity of 106 m/s during, a) 60 seconds, b) 30 seconds, and c) 10 seconds, at different nozzle inclinations. All tests were performed on a flat surface.

In general, Figure 4.8 shows that the erosion rate depends on the nozzle angle inclination, application time, and powder size. Erosion rate reached a value of 1.2 mg/g when an nozzle inclination of 30° with a powder size of 50 μm during 60 secs. was used (shown in Figure 4.8 (a)). Figure 4.8 (c) shows that the erosion rate is not bigger than 0.0010 mg/g when the aluminium surface was blasted for only 10 secs. for both powder sizes (10 μm and 50 μm) with any nozzle inclination. Chapter 5 includes an analysis of the effect of erosion in a dimple.

4.6 Summary

In this chapter, the benefits of adding a second layer of roughness through a HVAM technique is discussed. A flat aluminum surface was textured at different nozzle inclinations and times, using two different grain sizes of 10 μm and 50 μm. After the texture process, the roughness of the surface was measured, showing a change in the R_{sk} and R_{ku} parameters. After this, both the contact angle and the contact angle hysteresis of a water droplet were measured on every textured surface and compared with a flat surface. Results show that roughness changed the contact angle between the droplet and all the textured surfaces. However, the contact angle hysteresis was only smaller when a 10 μm grain size was used, indicating better wettability and lubrication, thus improving the coefficient of friction (section 6.3.1 shows this).

CHAPTER 5. TRIBOLOGICAL MODELLING

Modelling of the tribological behaviour of textured surfaces is one mechanism by which the disadvantages of those surfaces can be analyzed and reduced, as several of these challenges can be identified beforehand. These include: excessive dimple depth, high dimple density, and lack of lubricant. Furthermore, comparison of measured friction forces with those predicted by the model can be used to identify issues with patterning the surface, such as issues with: uniform depth of dimples, dimples size, or contact area. The performance of textured surfaces depends upon the geometry of the surface patterns. It is therefore essential to understand how different texturing parameters affect the resulting topographic structure.

5.1 Theoretical

In order to understand and predict the tribological behaviour of lubricated textured surfaces, a series of simulations were carried out using MAHLE Virtual Tribology Laboratory – VTL 3.8 developed by Tomanik *et al.* (Profito, Zachariadis, and Tomanik 2011; Prófito 2010). This program allowed the calculation of the contact parameters necessary for the application of the Greenwood models from the roughness profile or the topography of real surfaces. To reduce the complexity involved in modelling three-dimensional geometries, VTL simulates lubrication conditions by simultaneously solving the one-dimensional Reynold's equation for the hydrodynamic phenomena by average visco-correction on a multi-block structured grid. Thus, a 2D computational domain with the texture is used. Previous researchers (Arghir *et al.* 2003; Han *et al.* 2010) have shown that the pressure profiles for 3D and 2D texture geometries are similar

and could accurately predict the load using a 2D geometry. There is a 2 – 8% difference between the 2D and 3D simulation; this difference depends on factors such as: the kind of lubricant, the shape of dimples, movement speed, and the solution to the Reynolds equation. Figure 5.1 shows a schematic of the mathematical model proposed. It is important to mention that due to the limitations of the one-dimensional mathematical modelling implemented in the program, all the simulations that will be presented disregard any type of influence of the two-dimensional effects on the flow of the lubricating fluid through the micro-cavities present in the contact interface. In other words, in the presence of orthogonal rows of micro-dimples, these are considered as grooves of fixed dimensions. This is the main difference between this software and a 3D modelling software. The multigrid solution implemented in the VTL consists of a mesh of approximately 1×10^5 control volumes (Prófito 2010). The code also takes into account the asperity contact models based on the Greenwood and Tripp's formulations for the description of the asperity contact between rough surfaces (Greenwood and Tripp 1970).

In VTL, the lifting-up effect was predicted adopting the complementary Swift-Steiber boundary conditions. As for the lubricant rheology, the viscosity-pressure dependence and viscosity-shear-thinning effects were considered as well (Prófito 2010). For an isothermal and incompressible lubricant, the Reynolds equation is expressed as:

$$\frac{\partial}{\partial x} \left[\frac{(H_2 - H_1)^3}{12\mu} \frac{\partial P_H}{\partial x} \right] = \left[\frac{U}{2} \frac{\partial(H_2 - H_1)}{\partial x} \right] + \left[-U \frac{\partial H_2}{\partial x} \right] + \left[\frac{\partial H_{min}}{\partial t} \right] \quad (5.1)$$

where P_H is the hydrodynamic pressure (in Pa), μ is the lubricant dynamic viscosity (in $Pa*s$), U is the slide velocity of the mobile surface (in m/s), H_1 and H_2 are the geometry of the lubricant film (in m), and h_{min} is the minimum oil film thickness (in m). According to Profito *et al.* (Profito,

Zachariadis, and Tomanik 2011), to solve this elliptic partial differential equation, two boundary conditions are needed to define the hydrodynamic mathematical problem.

$$P_H(0, t) = P_1(t) \quad (5.2)$$

$$P_H(b, t) = P_2(t) \quad (5.3)$$

where P_1 and P_2 are the relative inlet and outlet boundary pressures in Pa respectively, and b the length surface in metres.

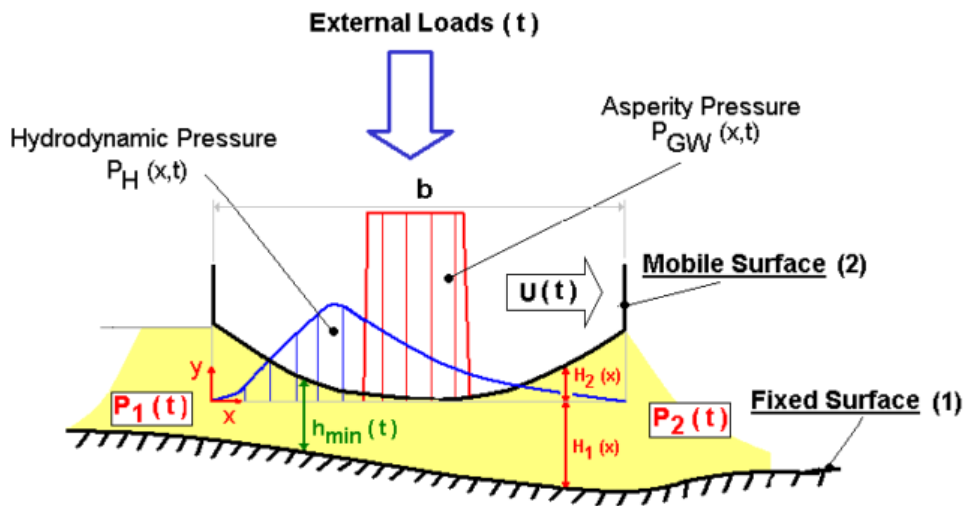


Figure 5.1. Tribosystem for the mathematical model proposed for Profito et al. (Profito, Zachariadis, and Tomanik 2011).

To solve Equation (5.1), Venner et al. (Venner and Lubrecht 2000), proposed a Finite Difference Scheme (FDS) with Successive Over-Relaxation (SOR) by setting to zero all pressures. The asperity of the rough surfaces was calculated using the Greenwood & Tripp model (Greenwood and Tripp 1970). The elastic deformation of each asperity is modelled based on the Hertzian contact theory, and it is assumed that the surfaces are covered by asperities with paraboloid shapes (with constant radius βi and uniformly distributed with a density area ηi), thus:

$$P_{ASP}(x, t) = \begin{cases} \frac{16\pi\sqrt{2}}{15} * E^* \left(\eta^2 \beta^2 \sigma^{5/2} \right) F_{5/2}[\bar{h}(x, t)] & P_{asp} \leq 3\sigma_{esc} \\ 3\sigma_{esc} & P_{asp} > 3\sigma_{esc} \end{cases} \quad (5.4)$$

where P_{ASP} is the asperity pressure (in Pa), E^* is the reduced Young's modulus (in Pa), \bar{h} is the dimensionless separation distance between surfaces (defined by the combined asperity summits' mean height, Z_s (in m), and the combined asperity summits' height standard deviation, σ (in m), calculated by Equations 5.5 and 5.6, respectively), β is the combined asperity summits' mean radius (in m), calculated from Equation 5.7, and η is the combined asperity summits' density in m^{-2} , calculated from Equation 5.8.

$$Z_s = \sqrt{Z_{s1}^2 + Z_{s2}^2} \quad (5.5)$$

$$\sigma = \sqrt{\sigma_1^2 + \sigma_2^2} \quad (5.6)$$

$$\beta = \sqrt{\frac{\beta_1^2 * \beta_2^2}{\beta_1^2 + \beta_2^2}} \quad (5.7)$$

$$\eta = \sqrt{\eta_1^2 + \eta_2^2} \quad (5.8)$$

According to Profito *et al.* (Profito, Zachariadis, and Tomanik 2011) the function $F_{5/2}[\bar{h}(x, t)]$ is a Gaussian random distribution of heights fitted by a sixth order polynomial, concluding that asperity contact will be significant only if $h < Z_s + 3\sigma$. In addition, from Equation 5.4, the contact pressures are strongly dependent on the mechanical properties and roughness of the surfaces in contact. The mechanical properties are expressed by the mean of the reduced Young's modulus, E^* , and by the mean of the tensile strength of the softer surface, σ_{esc} . The surface roughness is expressed by the contact parameters; Z_s , σ , β , and η . The VTL software

methodology assumes summits as the local maximum points above the surface (profile in one-dimensional cases) mean plane (line), and the calculation of the parameters (Z_s , σ , β , η) is done strictly numerically.

5.2 Two-dimensional results

To replicate the experimental conditions in the VTL simulations, 2-D profiles of the machined surfaces acquired from the Zeta-20 optical profiler was input into VTL for the base counter surface. Figure 5.2 shows a schematic of the simulation components. The flow direction of the lubricant is parallel to the x -axis, the maximum pressure can be found at the right edge of the dimple. The reason for this is that additional hydrodynamic pressure was produced by the converging wedge in this area. At the left edge of the dimple, however, there is a diverging wedge that can result in negative pressure. But considering the Reynolds equation on the diverging region, the pressure gradient with respect to the direction normal to the boundary is zero and the pressure is retained constant close to ambient pressure. So in the course of numerical calculation, only the positive pressure was used to calculate the value of the hydrodynamic pressure, as presented by Yu *et al*, (Haiwu Yu, Wang, and Zhou 2009) and Hang *et al*, (Han et al. 2010).

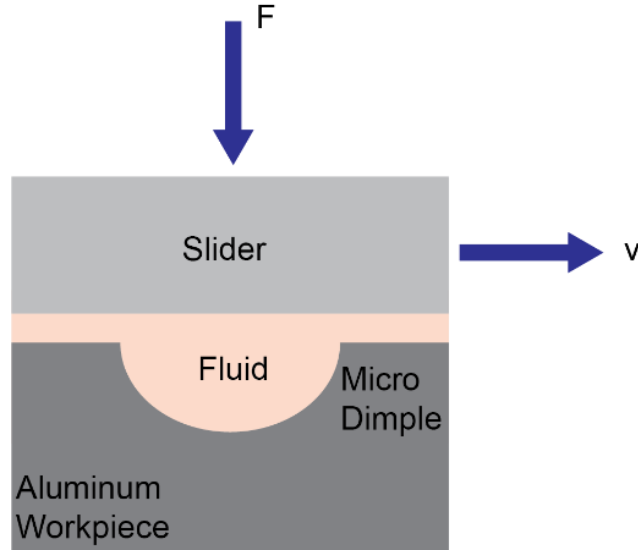


Figure 5.2. A schematic of the tribological simulation. A slider moves with a velocity v over a stationary aluminum workpiece with an applied normal force F . The surface of the aluminum workpiece designed from the surface topography was measured from a real surface, but contains at most one dimple in the simulation. A fluid between the slider and the aluminum workpiece matching the physical properties of the oil used in the experiments was then placed in the sliding contact.

The top surface was modeled as a flat slider that moved at 0.05 m/s in relation to the bottom dimpled/textured surface. The mechanical properties of the bottom textured surface matched those of the AL6061-T6 surface, as stated previously, and the top flat surface was modeled to have the same mechanical properties as the ruby hemisphere, using Herizian mechanics Equations 5.9 and 5.10.

$$E^* = \left(\frac{1 - \nu_1^2}{E_1} + \frac{1 - \nu_2^2}{E_2} \right)^{-1} \quad (5.9)$$

$$a = \left(\frac{3 * N * R}{4 * E^*} \right)^{\frac{1}{3}} \quad (5.10)$$

where E^* is the reduced Young's modulus, E_n is the Young's modulus of the n material, and ν_n is the Poisson's ratio of the n material. The contact diameter is denoted by a , R is the radius of the ruby half-sphere, and N is the applied load.

Using Equation 5.10, the contact diameter between the ruby hemisphere and the aluminum workpiece was estimated to be $64 \mu\text{m}$ at an applied load of 1 N , and $190 \mu\text{m}$ at an applied load of 25 N . This analysis clearly indicated that the contact was being subject to a high pressure, resulting in a high wear and deformation of the work piece that could be observed directly after testing. In addition, friction pairs (indenter and textured surface) were roughly simplified as infinite parallel planes with periodic micro-dimples in the simulations (Z. M. Zhang et al. 2011). Two parallel planes can also be considered as rigid walls. Thus, there was no external pressure (negative or positive) to push or pull the fluid in or out the textured surface (Han et al. 2010).

To determine how pitch between dimples can affect a dimpled surface, a series of simulations were run at pitch values of: $150 \mu\text{m}$, $350 \mu\text{m}$. All the simulations were held on a surface having a size of $1400 \mu\text{m}$, with dimples having a depth of $30 \mu\text{m}$, and using a constant load of 10 N . Simulated results are shown in Figure 5.3.

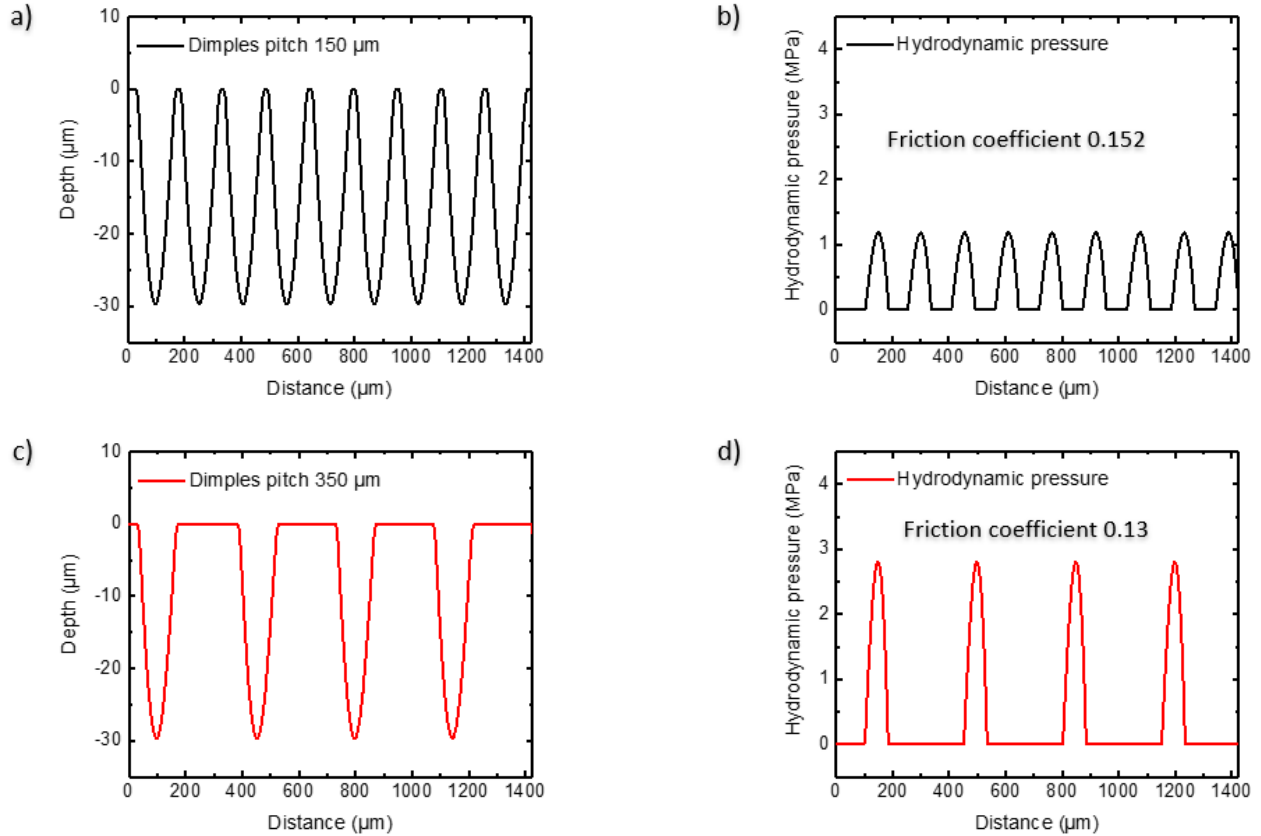


Figure 5.3. *Dimples profiles and hydrodynamic pressures for (a) dimples having a depth of 30 μm with a pitch of 150 μm , (c) dimpled surface having a depth of 30 μm with a pitch of 350 μm . Also, the hydrodynamic profile of (b) dimples having a depth of 30 μm with a pitch of 150 μm , and (d) dimples having a depth of 30 μm with a pitch of 350 μm .*

Results from Figure 5.3 indicate that varying the pitch between dimples can provoke a change in the hydrodynamic pressure, causing a change in the friction coefficient. Figure 5.3 (b) shows that when the dimples pitch was 150 μm the hydrodynamic pressure was about 1.2 MPa, and the friction coefficient was 0.152. This friction value could have been because of the high-pressure on the flat surface separating the dimples or because of a higher density of dimples causing an oil leak. Figure 5.3 (d) show that the hydrodynamic pressure was around 3 MPa, and having a friction coefficient of 0.13. Figure 5.3 (f) show that the hydrodynamic pressure was around 2.3 MPa, but the friction coefficient was 0.141. This difference of 8% indicates that a

proper pitch is beneficial to create hydrodynamic lubrication. Therefore, the dimple pitch of 350 μm was used in this research. Also, Figure 5.4 shows the surface profiles used in this research.

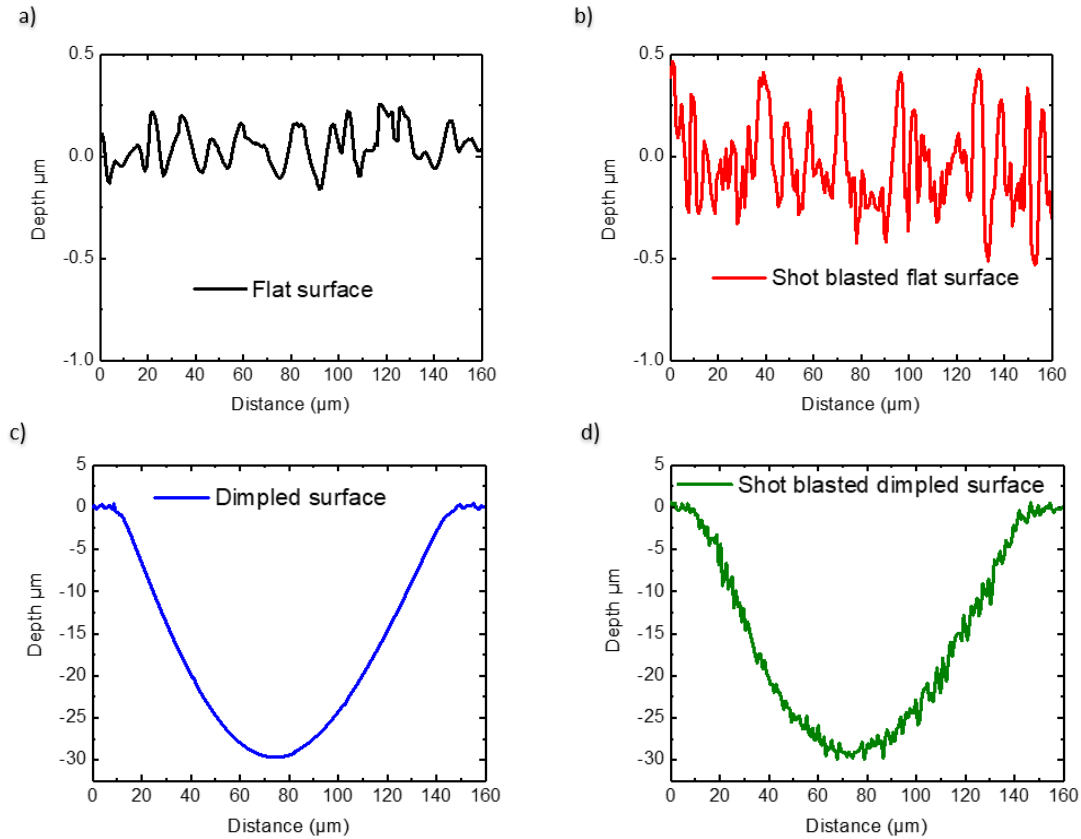


Figure 5.4. Profiles of the surfaces used during simulations. (a) Profile of the flat surface, (b) profile of a shot blasted surface, (c) profile of a dimpled surface, and (d) profile of a shot blasted dimpled surface.

Simulations were performed replicating the sliding conditions and surface structure of the aluminum workpiece, allowing for the generation of Stribeck curves. More specifically, these surfaces included a flat surface, a shot blast surface, a dimpled surface with a single dimple of a depth of 30 μm and diameter of about 150 μm , and a shot blasted dimple having the same plane view dimensions. In all cases, a fixed flat surface was used for the slider and a base oil lubricant with similar characteristics as the one used in experiments was chosen. Hydrodynamic simulations performed on these surfaces using the VTL software are shown in Figure 5.5.

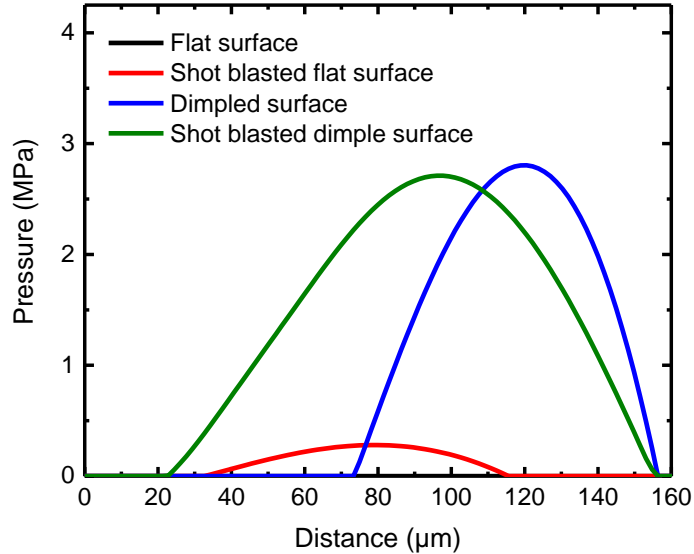


Figure 5.5. Hydrodynamic pressure profile determined from VTL simulations of the profiles shown in Figure 5.4. The pressure profiles for all surfaces are shown on one graph to make direct comparisons between the four variations, including a flat surface (black line), shot blasted flat surface (red line), dimpled surface (blue line), and shot blasted dimple surface (green line). The sliding speed was 0.05 m/s and an applied load of 15N was used in the simulations that generated these pressure profiles.

From simulation results shown in Figure 5.5, it is possible to observe an increase in the hydrodynamic load capacity around the divergent region of dimples. Thus, the observed increase in the maximum hydrodynamic pressure that resulted from changing the surface structure is generating a lift-up force on the sliding counter surface. Moreover, a 45% wider width of pressure profiles for the shot blasted dimple case is observed in Figure 5.5. The viscous-elastic oil film between sliding surfaces in elastohydrodynamic lubrication regime is equivalent to a massless spring element, thus creating an oil film stiffness, similar to that presented in gear systems (Y. Zhang et al. 2016; Zhou and Xiao 2018). However, the oil film stiffness concept has not been applied to the study of textured surfaces. In this research, the area under the curve generated due to the hydrodynamic pressure on the textured surfaces was calculated to obtain the oil film

stiffness. Figure 5.6 shows the hydrodynamic pressure area resulting from the simulated profiles when a load of 15 N was applied.

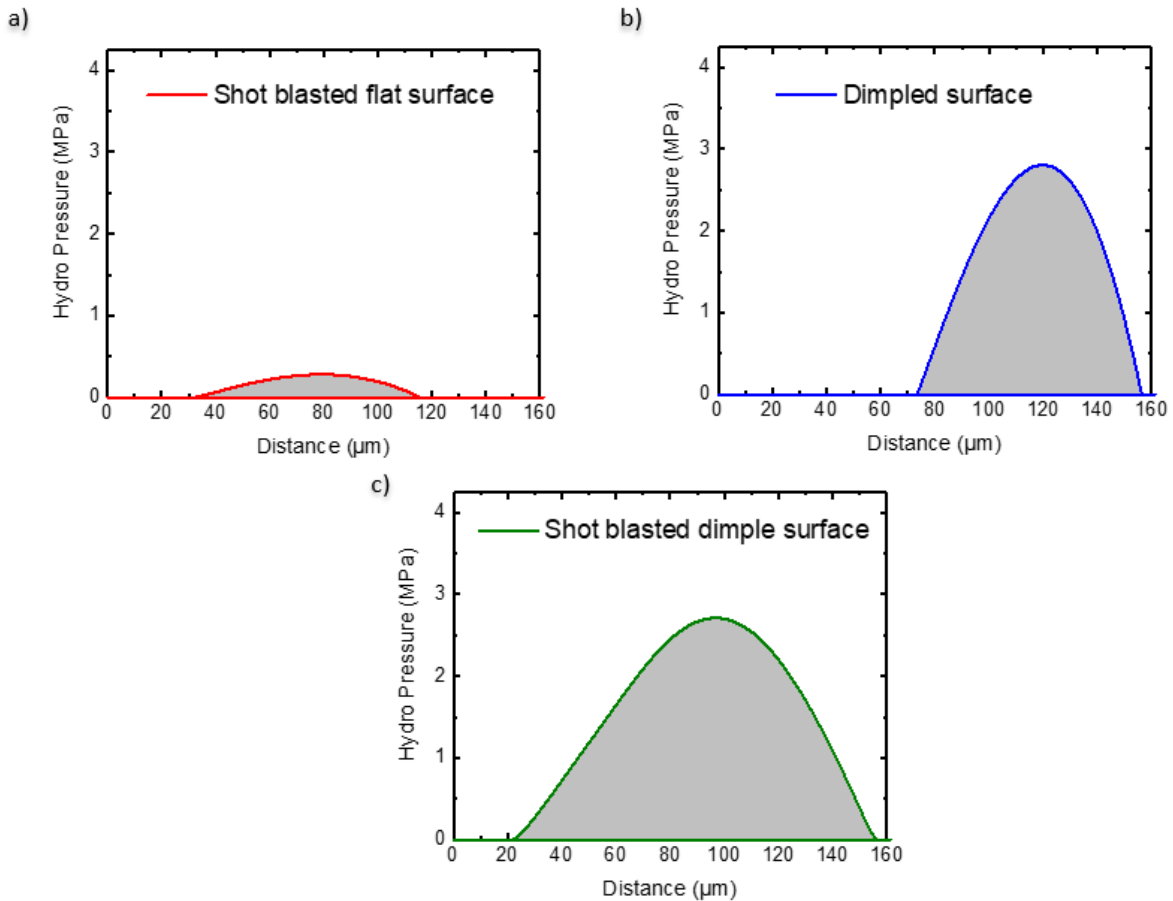


Figure 5.6. Measured hydrodynamic area under the curve for (a) a shot blasted flat surface, (b) a dimple surface, and (c) a shot blasted dimple surface.

The pressure area shown in Figure 5.3 acted as a force on the textured surfaces helping to support the applied load, similar to an oil film stiffness. This oil film stiffness depended on the deformation caused by the Hertzian pressure under EHL regime, which prevents damage and reduces the wear on textured surfaces (as shown in Figure 6.13). Results shown in Figure 5.6 (a) indicate the shot blasted flat surface created an oil film stiffness of 18.07 N/m; this could have been because of an extra amount of oil was stored in the micro spaces created after the blasting process, as denoted in the change in roughness between a flat surface (Figure 4.4 (a)) and a blasted

flat surface (Figure 4.4 (b)). Figure 5.6 (b) shows that in the dimpled surface there was a hydrodynamic pressure of 150.5 N/m caused by the effects of Hertzian pressure. Finally, there was an oil film stiffness of 216.08 N/m in the multitextured surface; this increment of about 45% in the oil film stiffness could have been because of the wetting effect caused by the change in roughness. However, it is important to avoid damage to the dimpled surfaces when multitexturing. Figure 5.7 shows the effect of the erosion on a multi texture dimple after using a powder size of 50 μm during 60 secs.

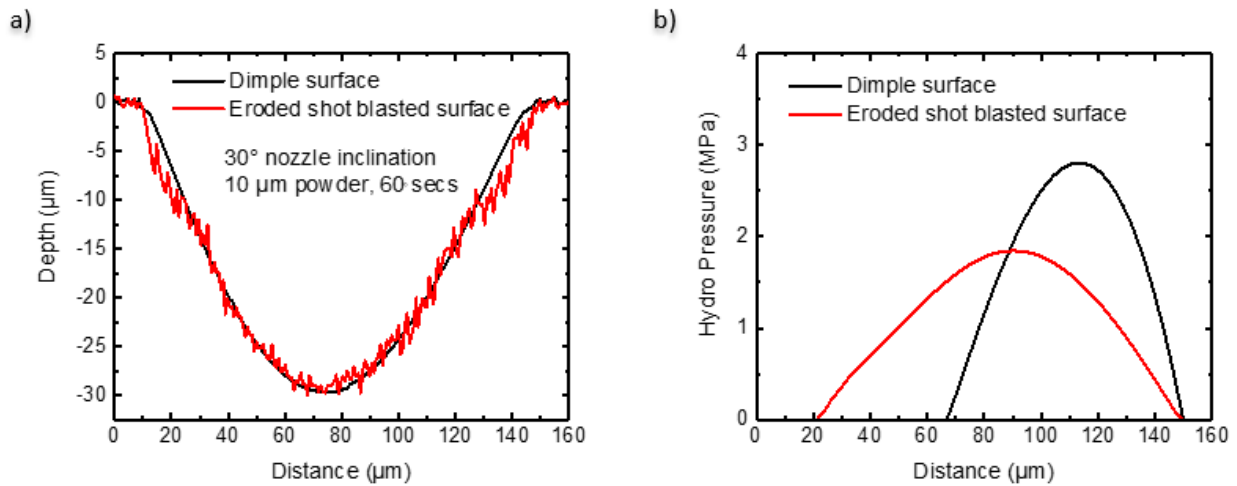


Figure 5.7. Effect of erosion on a multi texture dimple. (a) untextured dimple (black profile) is used to compared the erosion on a multi texture dimple (red profile). (b) Hydrodynamic pressure of a untextured dimple (black line) vs hydrodynamic profile of eroded multi texture dimple (red line).

Hydrodynamic pressure is affected by erosion, as shown in Figure 5.7 (b). The oil film stiffness of a dimple is 150 N/m, having a friction coefficient of 0.13. The oil film stiffness of an eroded shot blasted dimple is 145.5 N/m, having a friction coefficient of 0.129. When the shot blasted dimple is not eroded, the friction coefficient is 0.125. Therefore, the erosion caused by a nozzle inclination of 30° during 60 secs by a 10 μm powder has not a significative effect on the friction coefficient. However, it could be different for the wear rate. Hence, a blasting powder of 10 μm size with a texturing time of 10 secs. was used in order to prevent any damage by erosion

to the workpiece or completely cover the machined dimples. Figure 5.8 shows the Stribeck curve resulting from VTL simulations determined from profiles shown in Figure 5.3.

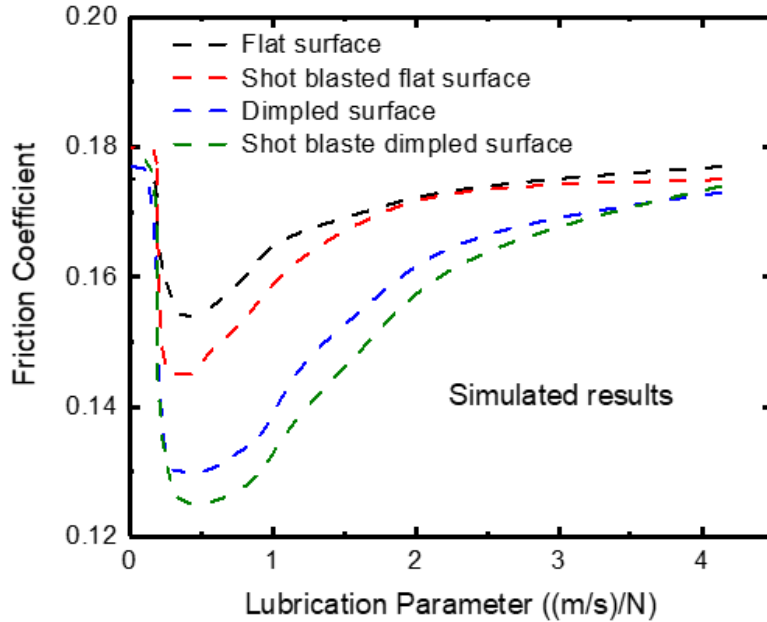


Figure 5.8. Stribeck curve determined from VTL simulations of the profiles shown in Figure 5.4. The Stribeck curve for all surfaces is shown on one graph to make direct comparisons between the four variations, including a flat surface (black line), shot blasted flat surface (red line), dimpled surface (blue line), and shot blasted dimpled surface (green line). The sliding speed varied from 0.05 m/s to 5 mm/s and the applied loads from 1 N to 25 N were used in the simulations that generated these Stribeck curves. These analytical results will be compared with experimental results in section 6.3.

Several studies (Křupka, Poliščuk, and Hartl 2009; Křupka and Hartl 2007b, 2007a; Mourier et al. 2006) have tried to explain the effect of film thickness on micro textured surfaces and its benefits; Křupka *et al.* (Křupka, Poliščuk, and Hartl 2009) concluded that a combination between film formation and textured surface increased the tribological properties of machine parts. The direct influence of the increased hydrodynamic pressure on the measured Stribeck curves will be compared in Section 6.3.

5.3 Summary

In this chapter, two-dimensional models of both the flat and the textured surfaces in contact with the rigid indenter were developed using the VTL software simulation. Simulations were performed replicating the sliding conditions and surface structure of the aluminium workpiece, allowing for the generation of Stribeck curves; these surfaces included a flat surface, a shot blast surface, a dimpled surface with a single dimple, and a shot blasted dimple (both dimpled surfaces having a dimple depth of 30 μm and diameter of about 150 μm). In all cases, a fixed flat surface was used for the slider and a base oil lubricant having similar characteristics used in experiments was chosen. Sliding contact was simulated, and the increase in the hydrodynamic load capacity around the divergent region of dimples was investigated. Each texture was analyzed individually, and its contribution to load support was taken into account. This analysis concluded that the observed increase in the maximum hydrodynamic pressure with changing the surface structure is generating a lift up force on the sliding counter surface.

CHAPTER 6. TRIBOLOGICAL TESTING AND ANALYSIS OF TEXTURED SURFACES

Dimpled surfaces have been studied previously (Nakano *et al.* 2007a; Ogawa *et al.* 2010; H. Yu *et al.* 2011a; D. Yan *et al.* 2010). Thus, several factors such as geometry, depth, texture, speed, and lubricant were considered in this work, achieving and discovering interesting results. For example, asymmetrical dimples show anisotropic, or sliding direction dependent, friction coefficients resulting from the variation in hydrodynamic pressures that occur when sliding from left to right versus right to left (Resendiz *et al.* 2015). In addition, the tribological benefits in terms of reducing the friction coefficient and wear rate adding a second layer of roughness on dimpled surfaces are demonstrated (Resendiz, Egberts, and Park 2018).

The tribological performance of the textured surfaces presented in this thesis have been evaluated in both dry and lubricated conditions, performed in forward and backward sliding directions (reciprocal movement). Different loads and speeds were applied. In all cases, the friction force was measured continuously with a table dynamometer. The load was applied using a ruby half-sphere with a diameter of 6 mm. Reciprocating friction tests were then performed by pressing the ruby-capped end mill against the textured surface. All the tests were performed within one week, under controlled conditions with a room temperature of 23 °C, where the humidity did not vary significantly (less than 5% RH) over the series of measurements. A Stribeck curve was used to summarize the results obtained for the various applied loads and speeds on the different surfaces.

6.1 Contact Mechanics on Textured Surfaces

Physical surfaces are rarely perfectly flat where they come into contact. Surface curvature or roughness often causes the contact areas to be extremely small, and therefore the resulting contact pressures and stresses are usually relatively high. In many cases, this has resulted in failure or yielding in the contact regions due to ploughing (Ghaednia *et al.* 2017). The mechanics of contact between solid surfaces has been extensively studied (Baney, Butt, and Kappl 2010; Y. Wang, Dhong, and Frechette 2015), describing the forces and deformations around the contact area between two pressed bodies, which play an important role in tribological interactions like wear and friction. For example, Elastohydrodynamic deformation (EHD) can cause lift and reduce friction during sliding (Gopinath and Mahadevan 2011; Scaraggi *et al.* 2011).

The Hertz contact theory allows the prediction of the resulting contact area, contact pressure, compression of the bodies, and the induced stress in the bodies (Baney, Butt, and Kappl 2010). Figure 6.1 shows a schematic of the well-known scenario of the contact between a rigid sphere and a flat surface, which also was used in this work.

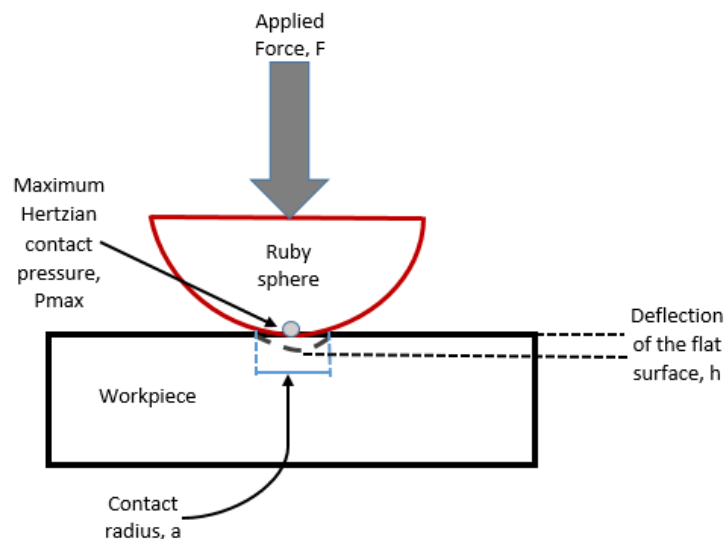


Figure 6.1. Schematic of contact between the ruby sphere and the workpiece.

In his research, Hertz (Hertz 1882) found that the radius of the sphere of contact a is related to the indenter applied force F , the indenter radius R , and the elastic properties of the materials by:

$$a = \sqrt[3]{\frac{3f_N R_{ind}}{4E^*}} \quad (6.1)$$

$$\frac{1}{E^*} = \frac{1}{2} \left(\frac{1 - \nu_1^2}{E_1} + \frac{1 - \nu_2^2}{E_2} \right) \quad (6.2)$$

where, E_2, ν_2 and E_1, ν_1 describe the elastic modulus and Poisson's ratio of the indenter and the specimen respectively.

The materials that have been used in the experiments are aluminum alloy number 6061-T6 (workpiece) and a ruby half-sphere (counter surface). According to the *Handbook Manual (ASM Handbook Volume 2: Properties and Selection: Nonferrous Alloys and Special-Purpose Materials 1990)*, the elastic module and Poisson's ratio for aluminum 6061-T6 is 68.9 GPa and 0.33, respectively. For ruby, these values 345 GPa and 0.28 (“Technical Data/Properties Synthetic Sapphire & Ruby” n.d.), respectively.

The deflection h_d of the flat surface around the indenter is given by:

$$h_d = \frac{1}{E^*} \frac{3}{2} \frac{F}{4a} \left(2 - \frac{R_{ind}^2}{a^2} \right) \quad (6.3)$$

The maximum Hertzian contact pressure, P_{max} , is given by the indenter load divided by the projected contact area:

$$P_{max} = \frac{3f_N}{2\pi a^2} \quad (6.4)$$

Table 6.1 shows a summary of the input parameters used to solve the above equations, while Table 6.2 shows the results obtained. The ruby ball used in all experiments was 6 mm in diameter. If a smaller diameter were to be used (i.e. 3 mm), the Hertzian contact pressure could have increased up to 50%, causing more deflection of the workpiece.

Table 6.1. Input parameters for *applying Hertz contact mechanics to estimate the maximum pressure beneath the ruby ball*

Input parameters	Symbol	Object 1	Object 2
		Sphere	Workpiece
Poisson's ratio	ν	0.28	0.33
Elastic modulus	E	3.52 GPa	68.9 Gpa
Yield stress	σ	800 MPa	476 Mpa
Diameter	d	6 mm	-
Applied force	F_N	1-25N	

Table 6.2. *Results of the determination of the contact pressures using Hertzian analysis.*

	Symbol	Value
Reduced modulus	E^*	3.64GPa
Contact circular radius	a	0.0325-0.0955 mm
Deflection	h_d	0.06-0.15 mm
Maximum Hertzian contact pressure	P_{max}	445-1302 MPa

A certain roughness will begin to deform plastically when the magnitude of the mean contact pressure reaches values above 10% of the yield stress (yield stress is the maximum pressure before the material starts to deform plastically) of the surface material of least hardness (Butt, Hans-Jürgen. Kappl 2010). As the resultant Hertzian pressure exceeded the aluminium yield stress, there was a plastic deformation of the aluminium workpiece, especially when a load of 25 N was applied. The Hertzian condition establishes the overall shape of the contacting surfaces so that one of the requirements for the generation of hydrodynamic pressure is that the surfaces must be converging in a region. The hydrodynamic pressure generated in this region has the task of separating the surfaces, which are forced together by the applied force (Totten 2012). Hence, dimples can help create the hydrodynamic pressure needed to separate those surfaces and avoid any excessive damage due to the high pressure applied on the workpiece by the ruby half sphere.

6.2 Tribological Mechanics and Experimental Setup

To perform friction testing on the surfaces of the flat and textured workpieces, the spindle of the mill was again rotated such that it was parallel with the normal of the workpiece surface. The end mill was removed and one capped with a 6 mm ruby hemisphere was put into the spindle. The spindle was then translated downwards, allowing the ruby sphere to make contact with the surface of the workpiece. A photograph of friction measurement apparatus/tribometer is shown in Figure 6.2.

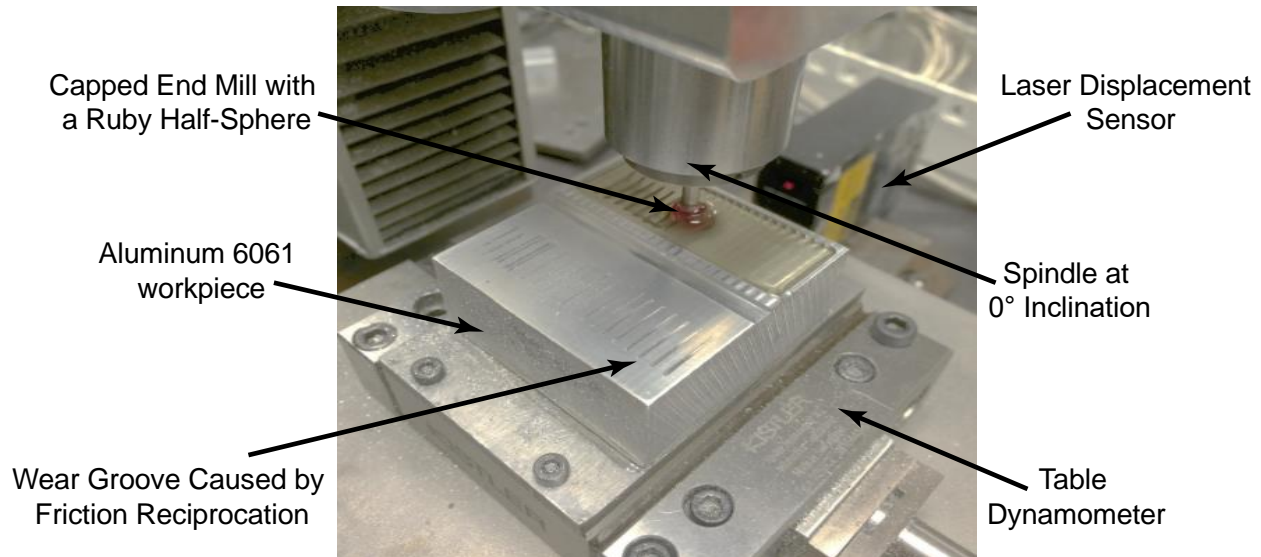


Figure 6.2. Photograph of friction measurement apparatus / tribometer. A 6 mm ruby ball is attached at the end of an end mill held stationary, while the workpiece, attached to a table dynamometer (a 3-axis table dynamometer), and is moved in a reciprocating motion. A laser displacement sensor measures the stage movement.

Reciprocating (forward and backward direction) friction measurements under controlled laboratory conditions (tests were performed at 23° Celsius, during the tests the temperature did not vary more than 10%) were conducted under both dry and lubricated conditions (5W30 engine oil) for asymmetrical dimples to investigate the effect of the anisotropic profiles of the micro-dimples on the measured friction coefficient. A reciprocating motion beneath the ruby sphere/spindle assembly for 100 cycles at a distance of 2 cm in each direction of the reciprocation cycle. The normal applied load was varied from 1 to 25 N at a sliding speed of 4 mm/s. this process was repeated 10 times. For the case of symmetrical dimples, mineral oil (AMRESO J217) having a viscosity of 14.2-17.0 cS at 40°C was used to avoid the effects of lubricants or any additive added to the motor oil. The normal applied load was varied from 1 to 25 N and two sliding speeds (0.5 mm/sec and 5 mm/sec) were used, this process was repeated 10 times and again under controlled laboratory conditions. The reciprocating movement was performed 100 times.

Hertzian contact pressure for these load ranges was determined to be 445 to 1302 MPa, assuming a Young's modulus and Poisson ratio of 68.9 GPa and 0.33 for the Al6061-T6 (*ASM Handbook Volume 2: Properties and Selection: Nonferrous Alloys and Special-Purpose Materials* 1990), and 345 GPa and 0.28 for the ruby hemisphere (Dobrovinskaya Elena R. Leonid A. Lytvynov. Valerian Pishchik 2009), respectively. In comparison to the applied stresses, the compressive strength for the Al6061-T6 alloy is 310 MPa (*ASM Handbook Volume 2: Properties and Selection: Nonferrous Alloys and Special-Purpose Materials* 1990) and 2.9 GPa (Dobrovinskaya Elena R. Leonid A. Lytvynov. Valerian Pishchik 2009) for the ruby hemisphere, indicating the applied loads are significantly above the yield stress of the aluminum workpiece.

The reported values of friction were determined using the following procedure: the normal force (F_N) and lateral forces (F_L) were the recorded forces in the z - and x -directions and were recorded in both the forward ($+x$) and backwards ($-x$) sliding directions. The average normal force during one reciprocating movement was recorded from the middle 60% of the data points acquired in that reciprocation, and the error represented the standard deviation in that value. Inclusion of this subset of the calculated friction coefficients is intended to remove the turning effects that occur at the start and stop of each reciprocation.

The friction force was half of the difference in the lateral force measured at each point along the surface. This calculation was necessary to remove the offset in the lateral force that may have resulted from surface topography (Ogletree, Carpick, and Salmeron 1996). The average friction force was the average value of the friction force for one reciprocation movement; thus, the error in this value was the standard deviation. Figure 6.3 shows the average friction coefficient (or the division of the average friction force by the average normal force) as a function of cycle number.

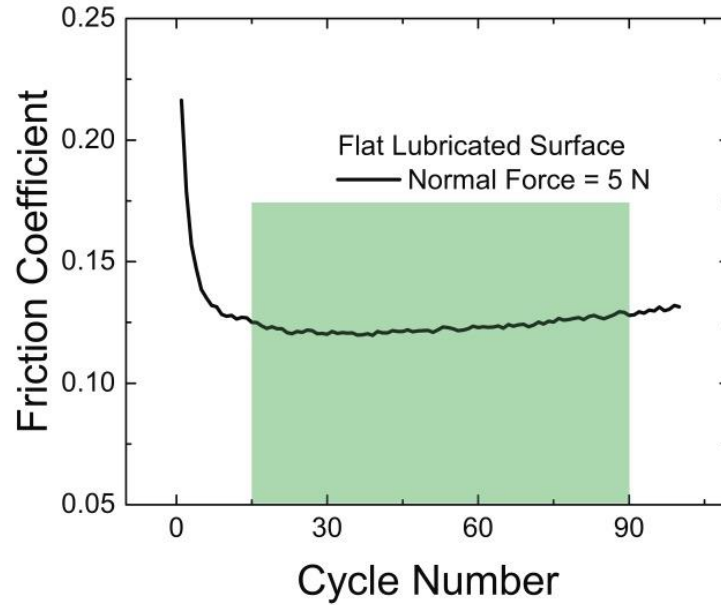


Figure 6.3. Measured friction coefficient versus cycle number for a flat, oil-lubricated surface. One hundred reciprocation cycles were recorded at an applied load of 5N on the Al6061 workpiece. The green square shows the region from which the steady-state friction coefficient was determined, which approximately corresponds to friction coefficients recorded from cycle numbers 25 to 90.

Figure 6.3 demonstrates the classic wear-in behaviour often seen in tribological experiments, where the friction coefficient drastically decreases in the initial sliding cycles and then reaches a plateau or steady-state value at higher cycle numbers. The average friction coefficient is determined from only those cycle numbers where the steady-state friction coefficient has been achieved.

6.3 Symmetrical Dimpled Surfaces

Circular shaped dimples were machined onto the flattened surfaces using a single crystal diamond cutter with a radius of 500 μm . Diamond tools have some advantages such as: micro-dimples machined with a diamond tool do not have bulges formed in their surroundings since there is no significant thermal damage compared to laser technology (Kurniawan, Kiswanto, and Ko

2017), and there is a lower surface roughness compared with the etching technique (Mukaida and Yan 2017). Figure 6.4 shows a schematic of the arrangement of the electric spindle in relation to the workpiece during the machining of the micro dimples.

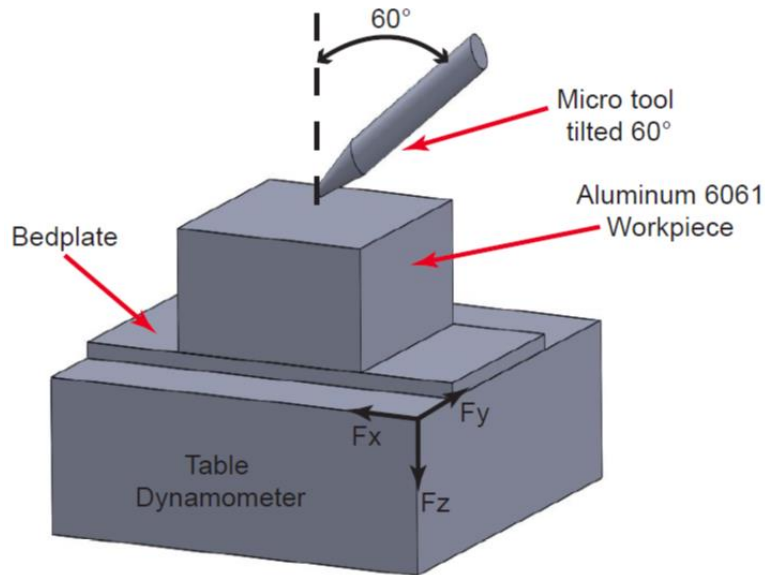


Figure 6.4. Schematic showing the inclination of the spindle relative to the workpiece allowing for the machining of dimple patterns on flattened surfaces of the workpiece.

Fast translation of the workpiece beneath the tilted ball end mill ensures that a small piece of the workpiece is removed during every revolution of the end mill. The machining of circular dimple patterns was realized by translating the workpiece at a feed rate of 4 mm/sec and a constant depth of 30 μm relative to the flattened surface, while the spindle operated at a rotational speed of 1000 revolutions/min and was placed at an inclination angle of 60° relative to the normal of the flattened surface.

In order to demonstrate the effect of a dimpled surface full of debris, a dimpled surface with added debris was prepared. To do this, the debris remaining from a flattened surface was added to the dimpled surface. A friction test using mineral oil was run using an applied load of 10 N over both a dimpled surface and a dimpled surface full of debris. Figure 6.5 demonstrates the instability

of the friction coefficient when the dimpled surface was full of debris, as proposed by Borghi *et al.* (Borghi *et al.* 2008).

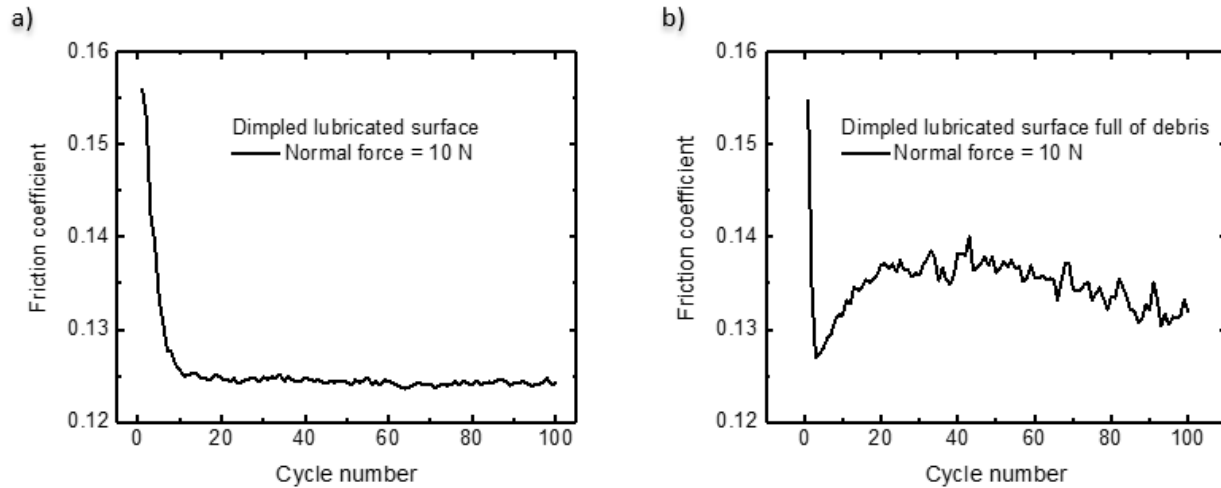


Figure 6.5. Measured friction coefficient versus cycle number for a (a) dimple lubricated surface, and a (b) dimple lubricated surface full of debris. One hundred reciprocation cycles were recorded at an applied load of 10 N on the Al6061 workpiece.

Figure 6.5 (a) shows a friction coefficient of 0.125 while Figure 6.5 (b) shows a friction coefficient of 0.135. Thus, for this case when the dimple surface was full of debris, there was an increase of the friction coefficient of about 8%. After the friction tests, some debris could be observed inside dimples, as shown in Figure 6.11. However, dimples are not completely full of debris neither completely vanish. Figure 6.6 shows the simulated hydrodynamic profile (black line) and the simulated friction force (red line) over a symmetrical dimple.

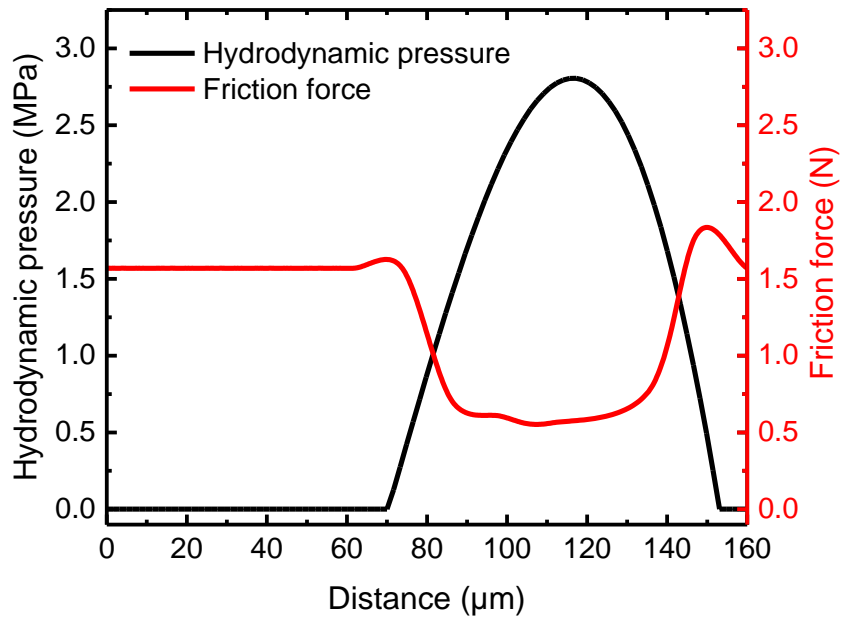


Figure 6.6. Simulated *hydrodynamic pressure* (black line) and *friction force* (red line) over a *symmetrical dimple*. The applied load was 13 N. The friction force starts around 1.5 N and drops to 0.55 N when the hydrodynamic pressure rises to about 3.5 MPa. The friction force reaches again 1.5 N when the hydrodynamic pressure drops to 0 again.

To perform the friction tests, four surfaces were prepared: a flat surface, a shot blasted flat surface, a dimpled surface, and a shot blasted dimpled surface. To summarize the results obtained for the various applied loads and speeds on the four different surfaces, Figure 6.7 shows a Stribeck curve for the shot blasted surface (Figure 6.7 (a)), symmetrical dimpled surface (Figure 6.7 (b)), and shot blasted dimpled surface (Figure 6.7 (c)). All textured surfaces were compared with a flat surface.

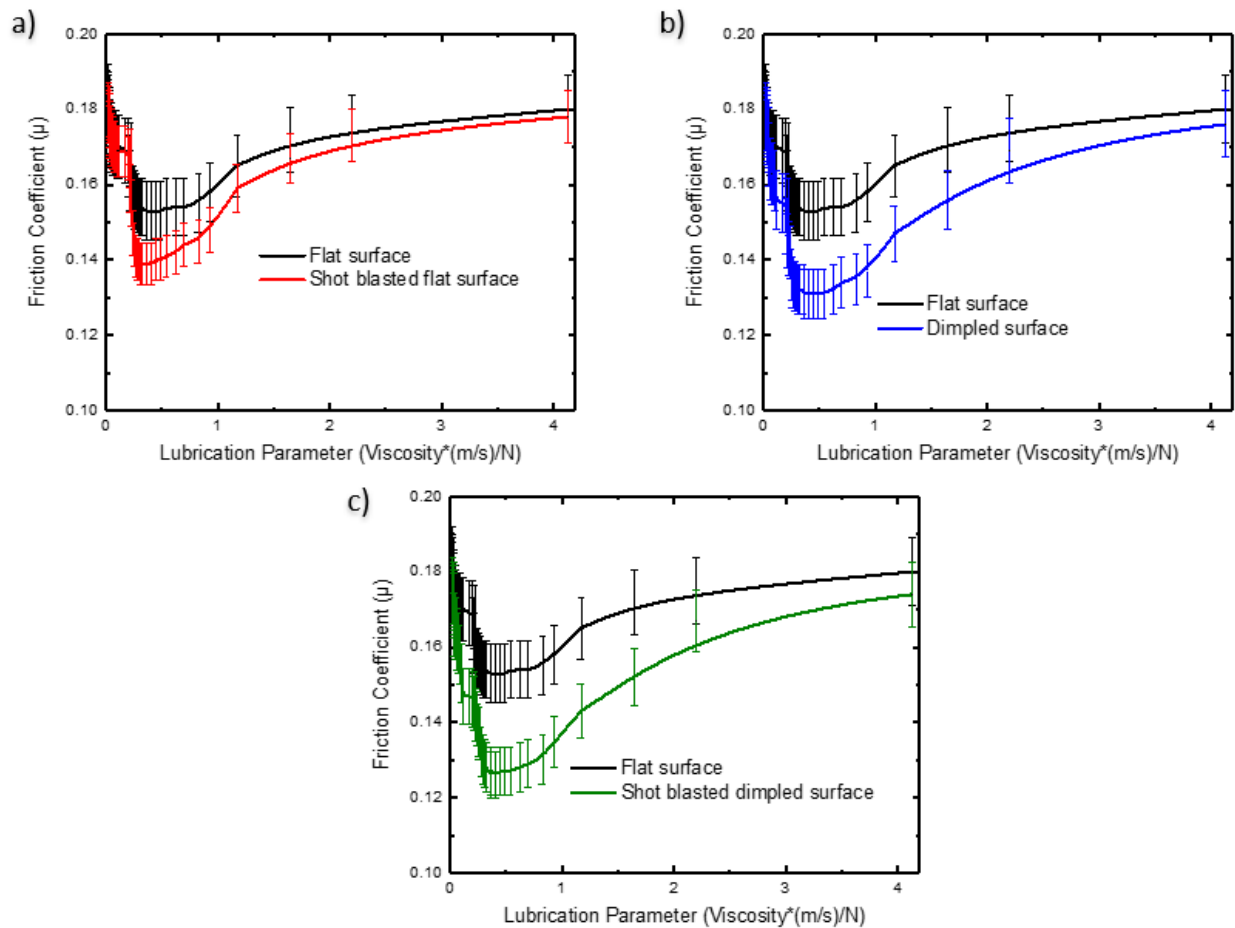


Figure 6.7. Stribeck curve compared with a flat surface for (a) a shot blasted flat surface, (b) a dimpled surface, and (c) a shot blasted dimpled surface. All tests were performed under lubricated sliding conditions during 100 iterations using a reciprocation speed of 0.5 mm/sec and 5 mm/sec.

Figure 6.7 (a) shows that when a shot blasted surface was used, there was an improvement of about 5% in terms of friction coefficient reduction in the onset of EHL compared with a flat surface. There is not a significant benefit in the boundary, mixed, or hydrodynamic lubrication regimes. Figure 6.7 (b) shows a comparison between the dimpled surface and a flat surface. The dimpled surface showed an improvement of around 12% in terms of friction coefficient when the applied load was increased compared with the flat surface. Again, the enhancement was present in the EHL region, but this time also in the hydrodynamic lubrication region. There was not a significant benefit in the boundary or mixed lubrication regimes. Figure 6.7 (c) shows there was an 18% friction coefficient reduction, when the shot blasted dimpled surface is compared with a flat surface. Benefits in the friction coefficient reduction were present in all the lubrication regimes. In general, as the speed increased, going from 0.5 mm/sec to 5 mm/sec. the friction coefficient decreased for all the textured surfaces, indicating that the lubrication regime transitioned from boundary to elastohydrodynamic lubrication regime.

A series of simulations were also performed to compare the analytical results with the experimental results of the Stribeck curves for a flat surface, a shot blasted flat surface, a single-dimple surface, and a shot blasted single-dimple surface, having the same plane view dimensions and replicating the lubricated sliding conditions and surface structure of the aluminium workpiece. Figure 6.8 shows the direct influence of the increased hydrodynamic pressure on the measured Stribeck curves.

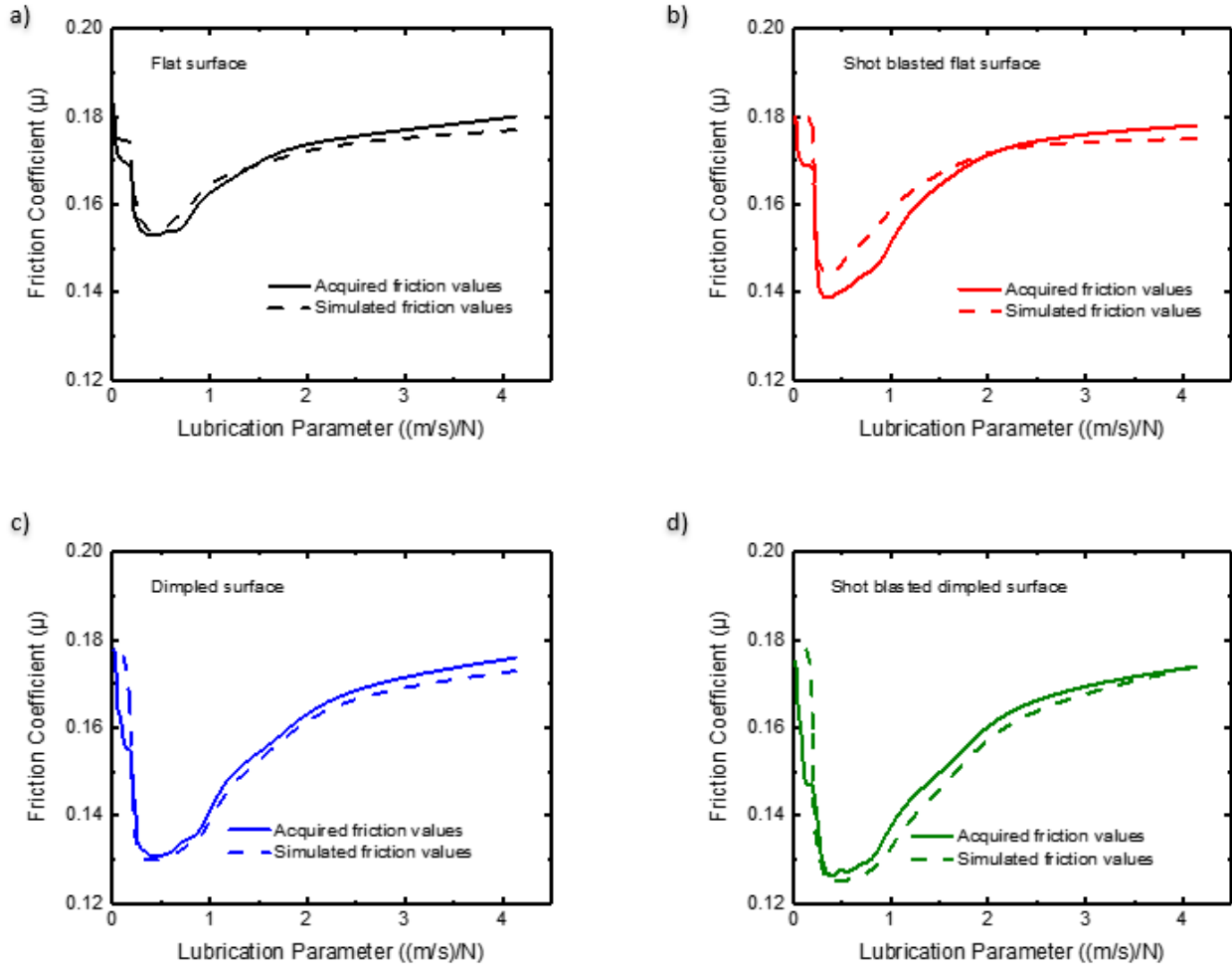


Figure 6.8. (a) Stribeck curve showing acquired experimental data (black solid line) and simulated (black dashed line) results of a flat surface. (b) Stribeck curve showing acquired experimental data (red solid line) and simulated (red dashed line) results of a shot blasted flat surface. (c) Stribeck curve showing acquired experimental data (blue solid line) and simulated (blue dashed line) results of a dimpled surface. (d) Stribeck curve showing acquired experimental data (green solid line) and simulated (green dashed line) results of a shot blasted dimpled surface.

The simulation results show enhanced lubrication through improved hydrodynamic forces, and the experimental results, whose enhanced lubrication properties are unknown, show very good overlap in Figures 6.8 (a), (c), and (d), corresponding to flat, dimpled, and shot blasted & dimpled surfaces. Significant variance is observed between experimental and simulation results in Figure 6.8 (b) for the shot blasted surface.

This indicates that the mechanism responsible for reducing friction on these roughened surfaces is not captured solely through hydrodynamic effects. The film thickness was calculated for the four different surfaces tested at the two sliding speeds examined with an applied load of 10 N, the results of which are summarized in Table 6.3.

Table 6.3 shows that the film thickness increased significantly for those surfaces that contained dimples, compared to the flat surface and the surface that had only been shot blasted. A small increase in the film thickness was observed when the velocity was increased from 0.5 mm/s to 5 mm/s. The results show that roughening the surface had a greater impact at higher sliding speeds than at slower sliding speeds, compared to the change observed with velocity for the flat and dimpled surface.

Table 6.3. *Maximum values of film thickness separating the aluminum workpiece and the slider at 0.5 mm/sec and 5 mm/sec and an applied load of 10 N. Film thicknesses were determined as the distance from the flat surface outside of the dimpled region to the top of the slider in the VTL simulations.*

Surface	Max. Film thickness at 0.5 mm/sec	Max. Film thickness at 5 mm/sec
Flat surface	0.27 μm	0.42 μm
Shot blasted flat surface	0.69 μm	0.84 μm
Dimple surface	68.05 μm	76.03 μm
Shot blasted dimpled surface	68.17 μm	93.7 μm

6.3.1 Effects of Roughness

Two of the critical surface properties for materials in micro/nanoscale applications are non-wetting (hydrophobicity) and low real area of contact (Jung and Bhushan 2006). As mentioned in Chapter 4, hydrophilic or hydrophobic properties of a surface (wettability) are characterized by the contact angle made between a water droplet and a surface. A surface is hydrophilic if the value of the contact angle is less than 90° , whereas the surface is hydrophobic if the value of the contact angle is greater than 90° . In order to determine the effects of wettability on multi-texture surfaces, a series of simulations were run (summarized in the Stribeck curves shown in Figure 6.9).

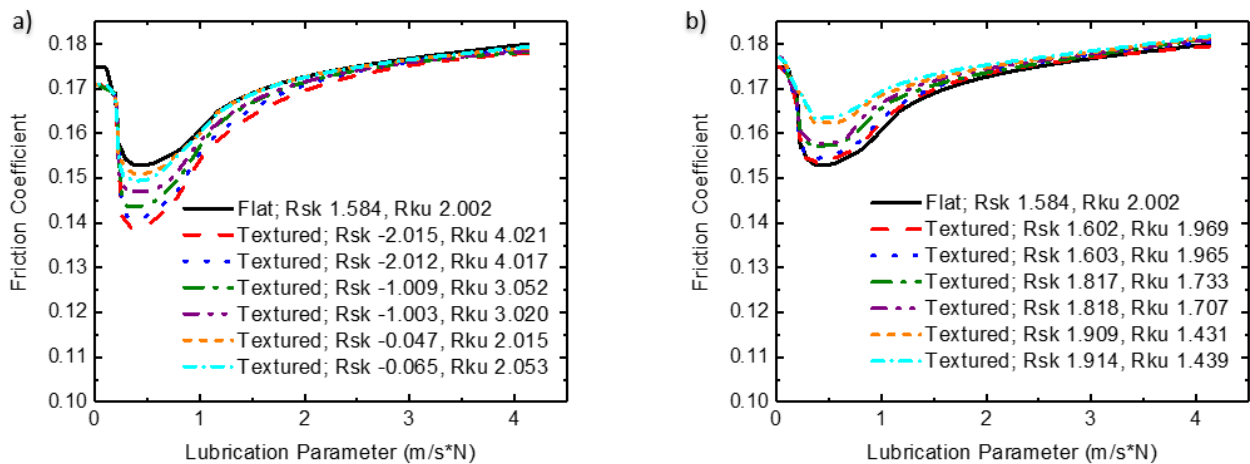


Figure 6.9. Simulated Stribeck curve for a flat surface, and different shot blasted surfaces, under lubricated sliding conditions. All cases were performed for 100 iterations using both a reciprocation speed of 0.5 mm/sec and 5 mm/sec. (a) Stribeck curve showing simulated results of a flat surface compared with a multi-textured using a grain size of $10\ \mu\text{m}$ with different nozzle inclinations and texturing time. A higher value of Rku and more negative Rsk lead to lower friction. (b) Stribeck curve showing simulated results of a flat surface compared with a multi-textured surface using a grain size of $50\ \mu\text{m}$ with different nozzle inclinations and texturing time.

Figure 6.9 shows the influence of increased roughness on the measured Stribeck curves. Only the textured surfaces produced with a $10\ \mu\text{m}$ aluminium oxide micro-abrasive particle powder have a lower friction coefficient when compared with a flat surface, especially when the nozzle was at the normal position and an exposure time of 10 seconds was used. For this case, the

simulation indicated a 7% friction reduction in total for all the lubrication regimes. From Figure 4.5 (a) and 4.7 (a), it is observed that CA decreases 30% and CAH decreases 50% when a textured surface with the above-mentioned parameters is compared with a flat surface, indicating that a lower CA with a lower CAH is beneficial to decrease the friction coefficient. On the other hand, when a 50 μm aluminium oxide was used, the friction coefficient increased up to 10%.

6.4 Asymmetrical Dimpled Surfaces

Using the inclined micro-milling technique with a flat end mill, another application of patterned surfaces was investigated: anisotropic or sliding direction dependent friction coefficients resulting from the variation in hydrodynamic pressures that occur when sliding from left to right versus right to left. Friction tests were performed to study the performance of unique surface patterns obtained by using the inclined micro-milling technique and flat end mills.

Figure 6.10 shows the average friction coefficient versus the applied normal force. As expected, Figure 6.10 shows a lower friction coefficient for both the lubricated flat (hollow black squares) and dimpled (hollow red circles) surfaces compared to unlubricated flat (filled black squares) and dimpled (filled red circles) surfaces. In both lubricated and unlubricated conditions, the dimpled surfaces produced lower coefficients than those of the flat surfaces. The observed lower friction coefficients of friction on dimpled surfaces in comparison to flat surfaces were consistent with previous studies of lubrication (Ryk and Etsion 2006; I Etsion and Sher 2009; I Etsion 2004; Galda, Pawlus, and Sep 2009; Ramesh *et al.* 2013; X. Wang *et al.* 2001; Ronen, Etsion, and Kligerman 2001a). Figure 6.11 shows the lateral force divided by the average normal force for two reciprocating motions of the tribometer under lubricated conditions for flat and dimpled surfaces. The lateral force offset from the topography was determined on the flat surface and applied to both data sets.

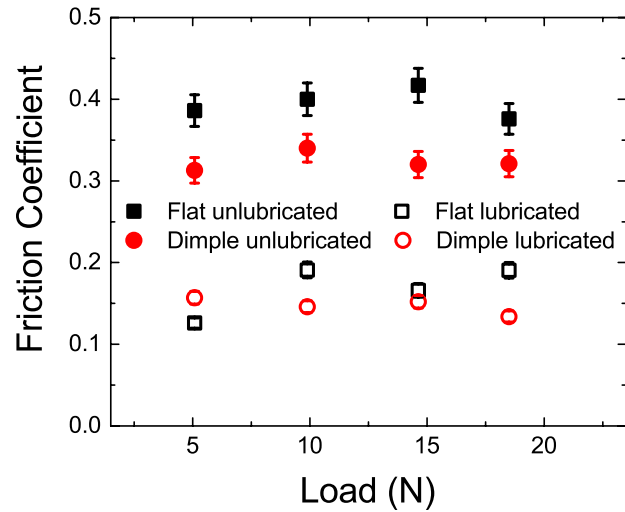


Figure 6.10. Average friction coefficient versus normal load measured for flat and dimpled surface under lubricated and unlubricated sliding conditions. All cases were performed for 100 iterations at a speed of 4 mm/sec. The friction coefficient reported here represents the average steady-state value of the friction coefficient from approximately cycle 25 to cycle 90. The maximum pressure beneath the sliding ruby sphere calculated using Hertzian contact mechanics for the applied loads measured ranges between 112-179MPa. The elastic module for aluminum 6061 and Poisson's ratio is 68.9GPa and 0.33, respectively ("ASM Material Data Sheet" n.d.), while the elastic modules and Poisson's ratio for ruby is 3.52GPa and 0.28 ("Technical Data/Properties Synthetic Sapphire & Ruby" n.d.), respectively.

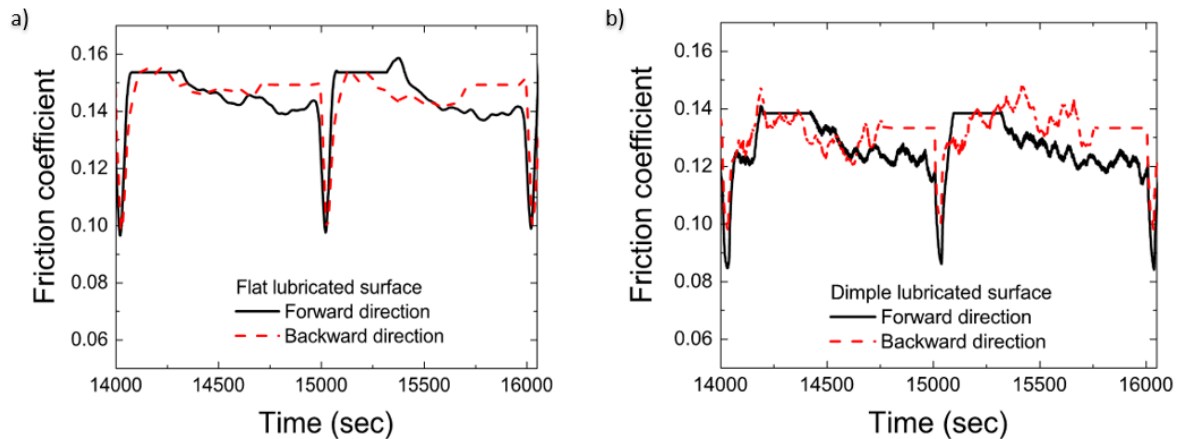


Figure 6.11. Friction coefficient measured during reciprocating motion of the tribometer applying a normal force of 18.5 N for (a) lubricated flat surface in forward and backward direction, friction coefficient of 0.141 ± 0.010 for both forward and backward directions, and (b) lubricated dimpled surface in forward and backward directions with friction coefficient of 0.126 ± 0.009 for the forward directions and 0.131 ± 0.009 for the backward direction.

Determination of the offset for the zero value of force offset from the untextured surface assumes the friction loop has the same value as the forward and reverse sliding directions. Given the analysis of the friction data presented in similar studies of friction on textured surfaces, a similar assumption regarding the symmetry of the friction loops has been made for these surfaces (Myant et al. 2010; Leeuwen 2010). As expected, the friction coefficient on the lubricated dimpled surface in Fig. 6.9 (b), on average, was lower than that for the lubricated flat surface.

6.5 Wear Analysis

Optical profilometry was conducted to obtain three-dimensional images of the worn samples after tribological tests. Figures 6.12 (a), (b), and (c) show a plane view optical image of a flat surface, dimpled surface, and a shot blasted dimpled surface after friction tests. To measure the wear volume on these surfaces, a cross section from the three-dimensional image was taken, as shown in Figures 6.12 (d), (e), and (f). These line profiles show the change in the surface as a result of the friction measurements. Wear coefficients were determined by the amount of volume lost, which were in turn determined by a summation of the area removed in the line profile along the wear scar.

Comparing the initial depth of the dimples, which were approximately 30 μm as shown in Figures 6.12 (b) and (c), with the depth measured in Figures 6.12 (e) and (f), shows that the dimples have decreased in depth substantially. In fact, their depth was only approximately 3-17 μm in the worn region. Given that the wear track itself is only 1-3 μm deep in Figures 6.12 (e) and (f), it is seen that wear particles or other debris have filled the dimples significantly over the course of the measurement.

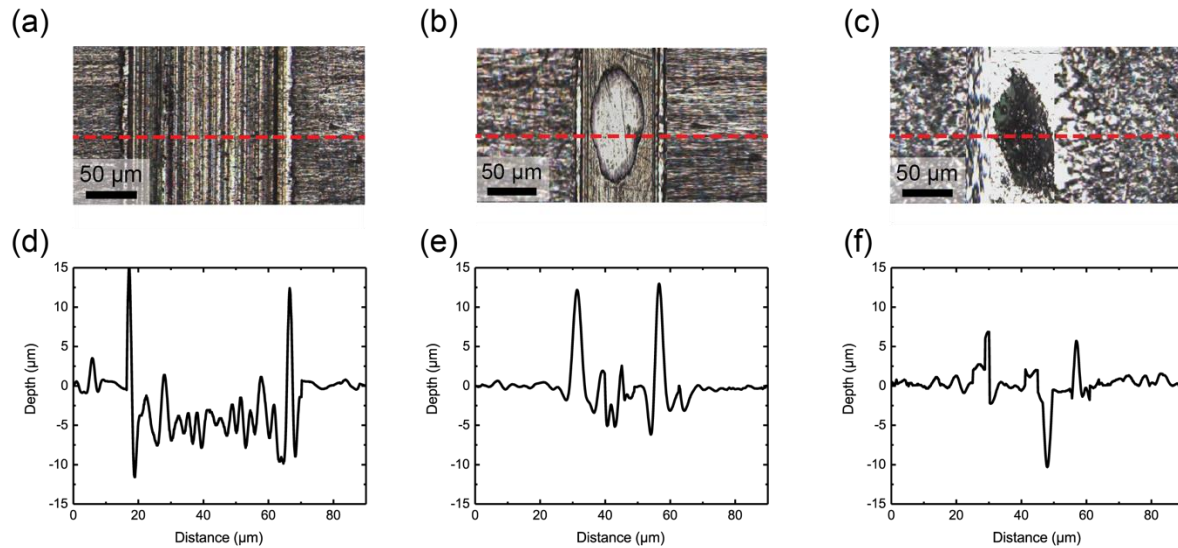


Figure 6.12. Optical images of the worn surface on (a) flat surface, (b) dimpled surface, and (c) a shot blasted dimpled surface after a tribological test. These scratches were taken from samples where a reciprocation speed of 5 mm/sec and applied load of 15 N was used. Also, Figure 6.10 shows the wear profile of (d) flat surface, (e) dimpled surface, and (f) a shot blasting dimpled surface. The red dotted line indicates the position where the wear profiles were taken.

After tribological tests and similar procedures as presented by Timothy *et al.* (Rupert and Schuh 2010), the area both below and above the zero level was integrated and multiplied by the track length to determine the total wear rate, considering the Archard equation presented by Mandal *et al.* (Mandal, Dutta, and Panigrahi 2004).

$$V = \frac{K * l * P}{3 * H} \quad (6.5)$$

where K is the wear coefficient, l is the sliding distance, P is the applied load and H is the material hardness. The corresponding absolute wear volume versus load for each of the surfaces is presented in Figure 6.13. For both the dimpled surface and the shot blasted dimpled surface, the volume due to dimple cavity was not considered as part of wear measurement.

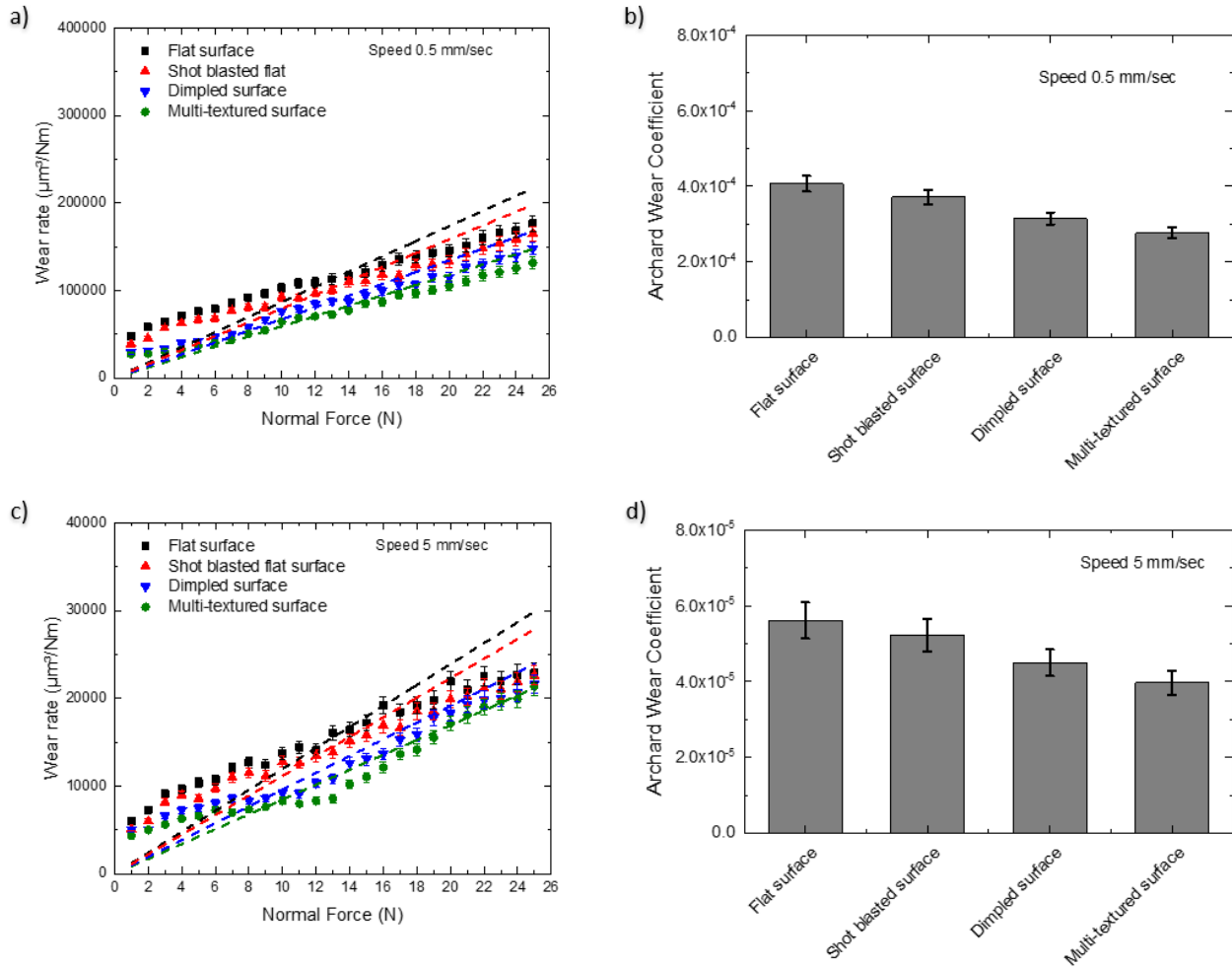


Figure 6.13. (a) Comparison of average wear versus applied load with a reciprocation speed of 0.5 mm/sec for the flat surface (black squares), sandblasted flat surface (red triangles), dimple surface (blue inverted triangles), and sandblasted dimple surface (green circles). Dashed lines in the same colours as the data points represent linear fits to the wear volume versus normal force data, where the intercept was forced to 0 N. The slopes of these fits are $8700 \pm 100 \mu\text{m}^3/\text{Nm}$ (flat surface), $8000 \pm 100 \mu\text{m}^3/\text{Nm}$ (shot blasted surface), $6700 \pm 700 \mu\text{m}^3/\text{Nm}$ (dimpled surface), and $6000 \pm 70 \mu\text{m}^3/\text{Nm}$ (shot blasted dimple surface). (b) Archard wear coefficients calculated from the slopes determined in (a), the measured hardness of the aluminum work piece ($141 \pm 7 \text{ MPa}$), and the length of the wear track measured ($300 \mu\text{m}$). (c) Comparison of average wear versus applied load with a reciprocation speed of 5 mm/sec. for the flat surface (black squares), sandblasted flat surface (red triangles), dimple surface (blue inverted triangles), and sandblasted dimple surface (green circles). Dashed lines in the same colours as the data points represent linear fits to the wear volume versus normal force data, where the intercept was forced to 0 N. The slopes of these fits are $1200 \pm 100 \mu\text{m}^3/\text{Nm}$ (flat surface), $1120 \pm 100 \mu\text{m}^3/\text{Nm}$ (shot blasted surface), $970 \pm 70 \mu\text{m}^3/\text{Nm}$ (dimpled surface), and $850 \pm 70 \mu\text{m}^3/\text{Nm}$ (shot blasted dimple surface). (d) Archard wear coefficients calculated from the slopes determined in (c), the measured hardness of the aluminum work piece ($141 \pm 7 \text{ MPa}$), and the length of the wear track measured ($300 \mu\text{m}$).

A significant decrease in the wear rate of the shot blasted dimpled surface when compared with the flat surface for both speeds of 0.5 mm/sec and 5 mm/sec is shown in Figure 6.13. Overall, Archard's wear coefficient was higher on the flat surfaces compared with any textured surface regardless of the reciprocation speed. Compared with a flat surface, the shot blasted surface had wear reductions of 8.5% and 7% when using speeds of 0.5 mm/sec and 5 mm/sec, respectively. The dimpled surface showed wear reductions of 23% and 20% with speeds of 0.5 mm/sec and 5 mm/sec, respectively. Finally, the shot blasted dimpled surface had wear reductions of 30% and 30% when the reciprocation speeds were 0.5 mm/sec and 5 mm/sec, respectively.

6.6 Summary

Real contact area is a very important parameter that affects the friction coefficient; micro dimples can affect the EHL effect, causing a build-up of pressure and may also assist in optimizing the real contact area between surfaces. Contact conditions play an important role in improving the tribological properties on surface textures. For the case of full and mixed lubrication conditions, the micro dimples work as micro-hydrodynamic bearings, helping to increase the hydrodynamic pressure due to asymmetric pressure distribution and therefore increasing the load carrying capacity (Ryk, Kligerman, and Etsion 2002; X. Wang *et al.* 2001; Izhak Etsion 2013). In mixed lubrication conditions, this additional lift in hydrodynamic pressure alters the balance between hydrodynamic and boundary lubrication. Hence, the number of the asperities in contact decreases, so that friction and wear also decrease (I Etsion 2004; X. Wang, Kato, and Adachi 2002). In boundary lubrication, these dimples act as lubricant reservoirs for the continuous retention of lubricant (Wakuda *et al.* 2003; Nam P. Suh, Mohsen Mosleh 1994). In addition, it is shown that after adding the second layer of texture, surfaces present a decrement in terms of friction coefficient and wear for about 30% when compared with a flat surface.

CHAPTER 7. CONCLUSIONS

Energy is a key resource crucial for our sustainability. A considerable amount of energy is consumed to overcome friction, especially in the transportation, industrial, and power-generation sectors; major economic losses are also due to wear of products and components (Holmberg and Erdemir 2015). For this reason, friction reduction is critical for preventing wear and reducing global energy consumption.

In this study, textured surfaces were presented as an effective way to reduce friction and wear on sliding metallic surfaces, providing new insights into understanding the physical mechanisms governing sliding lubricated friction. In particular, the role of lubricant microtextured surfaces have been investigated, and the related consequences for the Stribeck diagram were determined. These results are necessary to design new frictional systems to determine more effective geometries for low-friction microtextured surfaces. This chapter summarizes the novel contributions presented in this study, and the assumptions and limitations involved. It concludes with the future studies to develop and improve the performed research.

7.1 Summary of the Research

This research has investigated the effects of texture surfacing as a method for tribological improvement on the friction coefficient in dry and lubricated sliding metallic surfaces under various normal loads and speed values. Two kind of dimples were machined by the inclined end milling technique, using two different micro tools on a flat 6061-T6 aluminum workpiece. The aluminium workpiece was chosen due its importance in many automotive components such as engines.

This machining technique offers unique advantages over other techniques like laser texturing; examples include high material removal rates, accurate surface finishes, few restrictions on the workpiece, the ability to produce a variety of different surface structures, fewer facility necessities, and lower energy requirements. In addition, using lasers can unintentionally modify the workpiece structure, due to the high temperature needed to create dimples.

A micro flat end milling with two flutes was used to create asymmetrical dimples, and a single crystal diamond cutter was used to create symmetrical dimples. A force modelling technique was proposed for the predictive determination of the size, shape, distribution, and end mill requirements for patterning surfaces. These calculations were validated by comparing the measured forces while milling the dimpled surfaces with the calculated forces from our machining model. The comparison between the model and experimental measurements of the machining forces also allowed for the determination of tool asymmetry, which could be correlated with variations in the geometry of the machined dimple pattern. For the case of symmetrical dimples, a second layer of texture was added by an HVAM technique helping to increase the roughness on workpieces and enhancing lubrication.

The performance of the textured surfaces in reducing friction was evaluated with a reciprocating tribometer by pressing a 6-mm ruby hemisphere against the aluminum textured surfaces and sliding them in forward and backward directions. In this study, asymmetric dimpled surfaces were lubricated with 5W30 engine oil and analyzed during a reciprocating sliding speed of 4 mm/sec. under both dry and lubricated conditions, while multi-scaled microtextured surfaces were analyzed under mineral oil-lubricated conditions during reciprocating sliding speeds of 0.5 mm/sec and 5 mm/sec. The performance of the multi-scaled microtextured surfaces with a constant

aspect ratio of 0.2 was evaluated through their sliding speeds and load-dependent friction coefficients, as well as their sliding speed and load-dependent wear rates.

The comparison of asymmetrical dimpled and flat surfaces shows that, under both lubricated and unlubricated sliding conditions, dimpled surfaces resulted in lower measured friction coefficients, which is consistent with the literature on symmetrically shaped dimples (Denkena, Kästner, and Wang 2010; Ryk and Etsion 2006; Haiwu Yu, Wang, and Zhou 2009; H. Yu et al. 2011b). Under unlubricated conditions a friction reduction of approx. 15% was achieved, indicating that a reduction in the contact area because of dimples is beneficial to reduce the friction. While for lubricated conditions a reduction in the friction coefficient of 18% was accomplished when compared with a flat surface. Furthermore, asymmetrically shaped dimples have been shown to have a sliding direction dependent response, in terms of the measured friction forces, there is a difference of 4% less friction in the forward direction compared with the backward direction.

On the other hand, the combined influence of multi-textured surfaces had a synergistic influence on the friction coefficient, suggesting that roughness of surface textures is a novel mechanism to further improve the friction and wear performance of dimpled surfaces. Surface texturing resulted in a decrease of the minimum friction coefficient that could be attained. This minimum value occurred at approximately the same Hersey number for all surfaces. In general, multi-textured surfaces lubricated with mineral oil present a friction reduction of about 20% for both the mixed and EHL lubrication regime and 6% for the boundary region when compared with a flat surface. For the case of symmetrical dimples, friction coefficient reduction is about 15% for both the mixed and EHL regimes and 3% for the boundary lubrication regime when compared with a flat surface. Overall, Archard's wear coefficient was higher on the flat surfaces compared with any textured surface regardless the reciprocation speed. Comparing with a flat surface;

dimpled surface shows a wear reduction of 23% and 20% with a speed of 0.5 mm/sec and 5 mm/sec. respectively. Finally, multi-textured surface has a wear reduction of 30% regardless the reciprocation speed when mineral oil was used.

In conclusion, it has been observed that surface texturing decreases the measured friction coefficient under both unlubricated and lubricated conditions and that greater reductions in the friction coefficient are observed for those surfaces that had been both dimpled and multi-textured. The best performance for this surface texture shape, in terms of low friction coefficients and wear rates, was demonstrated in the surfaces that had been textured with dimples and subsequently multi-texture, while flat, untextured surfaces demonstrated the worst results.

7.2 Limitations and Assumptions

In general, most studies have shown that the hydrodynamic pressure built in the liquid between the two surfaces is enhanced in elastohydrodynamic lubrication (EHL), thus typically moving the onset of EHL to higher loads, as well as lower velocities and lubricant viscosities (Gropper, Wang, and Harvey 2016; Křupka and Hartl 2007a; Mourier et al. 2006). However, other studies have shown that the textured surfaces allow for wear particles to be trapped in the surface textures, reducing friction between the surfaces (Ito et al. 2000; Kim et al. 2002; Borghi et al. 2008). The third mechanism that has been observed is that surface texturing acts as a lubricant reservoir, allowing it to reach the sliding interface faster (Borghi et al. 2008; Xing et al. 2013; Galda, Pawlus, and Sep 2009). In this research, two of these three mechanisms involved in the textured surfaces have been observed.

First, the experimental study of the influence of surface texturing has shown that texturing the surface does indeed reduce the friction coefficient compared with the flat surface, consistent with previous studies of textured surfaces (Ryk and Etsion 2006; Kovalchenko et al. 2004; Ryk,

Kligerman, and Etsion 2002). Both randomly roughening the surface and purposefully texturing the surface individually reduced friction, as shown in Figure 6.5. The combined influence of the multi-texture shows that improved performance can be made when the surface has a hierarchical surface texture to it. While a shift of the Stribeck curve to the left or right was not observed in Figure 6.5, a general trend of improved friction coefficients for a given Stribeck coefficient or Hersey number was observed in the mixed and EHL regimes.

A post-mortem analysis through the optical profilometry images in Figure 6.10 (c) showed that most of the surface texture and the roughness induced by HVAM was removed in the contact region, so the influence that these two surface texturing strategies have on friction must occur beyond the contacting region between the workpiece and the ruby hemisphere. While the observed results indicate a widening of the mixed and elastohydrodynamic lubrication regime, the most often reported influence of surface texturing has been to improve hydrodynamic lubrication (Ramesh et al. 2013; J. Zhang and Meng 2012; Kovalchenko et al. 2004; H. L. Costa and Hutchings 2007; Haiwu Yu, Wang, and Zhou 2010). Despite this fact, surface texturing has also been shown to improve boundary and mixed lubrication (Vladescu et al. 2015; T. Hu, Hu, and Ding 2012; Ryk, Kligerman, and Etsion 2002; Braun et al. 2014; Liew, Kok, and Ervina Efzan 2016; Wakuda et al. 2003). Thus, the results here indicate the complexity of understanding lubrication enhanced by surface texturing, which requires further examination to truly understand.

Two dimensional simulations conducted using the VTL software package support the mechanism through enhanced lubrication. While the simulation results did not capture the wear damage caused through sliding that was observed in the experiments, they exhibited the basic structure of the Stribeck curve for the various patterned surfaces, and showed the same decrease in measured coefficients with the change in surface topography through the four samples. This

observation suggests that the primary mechanism influencing the friction coefficients measured during lubricated sliding conditions was the build-up of hydrodynamic pressure. Despite the good reproduction of the experimental Stribeck curves at higher values of the Hersey number, the poor reproduction of the experimental results at lower values of the Hersey number was likely a result of the one-dimensional fluid modeling implemented in VTL software package, which was insufficient to reproduce the three-dimensional flows that occur in the experiments. More specifically, the simulations disregarded any type of influence of the two-dimensional effects on the flow fluid through the micro-cavities present in the contact interface (Prófito 2010).

To interpret the observed Stribeck curves in more detail, the simulations showed that there is a significant impact on the film thickness with the change in surface structure. Similar results have been observed previously, where higher sliding speeds and deeper surface features resulted in a decrease in the measured friction coefficient on textured surfaces (Vilhena et al. 2011), likely a result of improved fluid film thickness. Furthermore, the observed improvement in the friction coefficient recorded between surface roughening through multi-texture compared with surface texturing is consistent with the results observed in Vilhena's work. Finally, the observation of the friction coefficients converging to the same values at high values of the Hersey number for all surfaces is likely a result of viscous fluid forces and other friction mechanisms overwhelming the contribution of the improved fluid pressure developed in the sliding interface by the surface texturing pattern in reducing friction (Kovalchenko et al. 2005b; Lu and Khonsari 2007; Braun et al. 2014; X. Wang et al. 2009).

Secondly, the *post* examination of the surfaces show that the wear scars are typically on the order of a few micrometer deep into the surface. However, while the dimples were 30 μm deep before friction testing, they were less than 10 μm deep after friction testing. The results suggest

that the dimples are being filled in with by-products of sliding, suggesting that the capturing of wear particles and other contaminants that may influence the friction coefficient on the untextured surfaces is also important to the observed reduction on the dimpled surfaces. The production and storage of wear particles or other by-products of sliding was not captured in the simulations. While the simulations did not replicate the experiments in this respect, the good overlap between simulations and experiments resulting from the increased hydrodynamic lubrication that resulted from the surface texturing suggests that the trapping of wear particles and other debris does not play a significant factor in reducing the friction coefficient in textured surfaces. The calculation of the wear coefficient provides us with some greater insight into the friction and wear performance of the surfaces. The reduced friction with surface texturing appears to be linked with reduced wear in every case. Additionally, wear coefficients approximately one order of magnitude smaller when the velocity was increased from 0.5 mm/s to 5 mm/s, as shown in Figure 6.11.

Finally, linking Figure 6.11 with Figure 6.5 and the trends observed with the Hersey number, it suggests that EHL lubrication and the associated low wear rates that was indeed achieved at the low applied loads and high sliding speeds, given the reduced friction forces and wear coefficients. Thus, the observation of reduced friction coefficients attributed to enhanced fluid pressure resulting from the surface texturing is supported by the observation of the lowered wear rates also observed with surface texturing. Variation in the dimple pitch, density, size and depth ratio, shape and configuration (parallel or stagger) may result in a variation in the relative contribution in the reduction of friction of increased hydrodynamic pressure in the contact versus wear particle entrapment but would require further experimentation to verify this hypothesis.

7.3 Future Work

In the future, more experiments need to be conducted to ascertain the performance of the micro textured surfaces. Thus, a variety of materials can be used to fabricate the surfaces, each suitable for a specific application. For example, materials like magnesium alloys and copper can be used to fabricate the current micro textures discussed in this work to generate higher load support. In addition, different dimples configurations must be performed applying the tilted spindle technique shown in this research. For example, different shapes, densities and texture arrangement like the ones presented by Galda *et al.* (Galda, Pawlus, and Sep 2009), and Yu *et al.* (H. Yu et al. 2011b). Also, interferometry techniques can be used to measure the film thickness accurately between the opposing surfaces.

In this study, a single geometry of spherical dimple with the aspect ratio of 0.2 was investigated. However, several studies have worked with different ratios and showed exceptional results. For example, the work done by Hu *et al.* (T. Hu, Hu, and Ding 2012), where dimples having a diameter of 45 μm , 160 μm and 300 μm with a depth of 25 μm were created and thus, with a ratio of 0.555, 0.156 and 0.083. Under the experimental conditions, the best dimples size is found to be 160 (ratio of 0.156). In the research conducted by Nakano *et al.* (Nakano et al. 2007b), dimples have a ratio of 0.16, and friction coefficient results show a better performance compared with an untextured surface. In the research performed by Ito *et al.* (Ito et al. 2000), dimples having a diameter as big as 0.5 mm and depth of 0.1 mm, thus a ratio of 0.2 was created and showed a lower friction coefficient than an untextured sample. On the other hand, small ratios can be detrimental, as shown in the research made by Choudhury *et al.* (Choudhury et al. 2015), which depth/diameter ratio was 0.066 but when compared the friction coefficient of texture surfaces against an untextured one, it was higher. An interesting result was achieved by Greiner *et al.*

(Greiner et al. 2014), showing dimples having a depth of 20 μm and a bigger diameter of 100 μm . It is, ratios bigger than 0.2 present a decrement of static friction. Therefore, static friction data has to be taken into account when searching for the optimum dimple dimensions and not only to consider the ratio value of depth/diameter.

The elasto-hydrodynamic model could be extended with the plasticity theory from the contact mechanics approach. Further development of the homogenization techniques presented here also consider elastic and possibly plastic deformation as another interesting area. Perhaps the most important physical aspect to be considered here are the thermodynamic effects, which are present in all situations that may be simulated with the different approaches developed in this thesis.

In addition, changes in the film thickness can be probed using Laser Induced Fluorescence techniques, such as those developed by Hidrovo *et al.*, (Hidrovo and Hart 2001). In this case, a new experimental setup would have to be implemented. For example, instead of texturing an aluminium surface, an etched glass can act as the textured surface and stay positioned on the top of the beam splitter, while a parallel plate could be used as a moving surface. In this way, the fluorescent dye could be mixed with the lubricant, and the lubricant thickness could be measured while the experiment is running. This measurement would give information about the exact gap height between the surfaces.

Several other aspects also need more attention. For example, deeper research into multi-scale features and their interactions with friction and wear is necessary. In addition, a future comparison between different machining techniques, such as tilted spindle and laser ablation would be of great interest. Finally, continued work on asymmetric dimples, their effects, and applications on creating a gradient of friction is also a noteworthy pursuit.

REFERENCES

- Ally, S., J. K. Spelt, and M. Papini. 2012. "Prediction of Machined Surface Evolution in the Abrasive Jet Micro-Machining of Metals." *Wear* 292–293: 89–99. <https://doi.org/10.1016/j.wear.2012.05.029>.
- Almqvist, T., A. Almqvist, and R. Larsson. 2004. "A Comparison between Computational Fluid Dynamic and Reynolds Approaches for Simulating Transient EHL Line Contacts." *Tribology International* 37 (1): 61–69. [https://doi.org/10.1016/S0301-679X\(03\)00131-2](https://doi.org/10.1016/S0301-679X(03)00131-2).
- Almqvist, T., and R. Larsson. 2002. "The Navier-Stokes Approach for Thermal EHL Line Contact Solutions." *Tribology International* 35 (3): 163–70. [https://doi.org/10.1016/S0301-679X\(01\)00112-8](https://doi.org/10.1016/S0301-679X(01)00112-8).
- Altintas, Yusuf. 2011. *Manufacturing Automation*. <https://doi.org/10.1017/CBO9780511843723.002>.
- Amanov, A., I. S. Cho, Y. S. Pyoun, C. S. Lee, and I. G. Park. 2012. "Micro-Dimpled Surface by Ultrasonic Nanocrystal Surface Modification and Its Tribological Effects." *Wear* 286–287: 136–44. <https://doi.org/10.1016/j.wear.2011.06.001>.
- Arghir, Mihai, Nicolas Roucou, Mathieu Helene, and Jean Frene. 2003. "Theoretical Analysis of the Incompressible Laminar Flow in a Macro-Roughness Cell." *Journal of Tribology* 125 (2): 309. <https://doi.org/10.1115/1.1506328>.
- ASM Handbook Volume 2: Properties and Selection: Nonferrous Alloys and Special-Purpose Materials*. 1990. ASM International.
- "ASM Material Data Sheet." n.d. Accessed May 27, 2015. <http://asm.matweb.com/search/SpecificMaterial.asp?bassnum=MA6061t6>.
- Bai, Linqing, and Shaoxian Bai. 2014. "Frictional Performance of a Textured Surface with Elliptical Dimples: Geometric and Distribution Effects." *Tribology Transactions* 57 (6): 1122–28. <https://doi.org/10.1080/10402004.2014.939317>.
- Baney, C.-Y. Hui and J. M., Hans-Jürgen Butt, and Michael Kappl. 2010. "Contact Mechanics and Adhesion." *Surface and Interfacial Forces*, no. 22: 219–50. <https://doi.org/10.1002/9783527629411.ch8>.
- Bedi, Sanjeev, Stephen Mann, and Cornelia Menzel. 2003. "Flank Milling with Flat End Milling Cutters." *CAD Computer Aided Design* 35 (3): 293–300. [https://doi.org/10.1016/S0010-4485\(01\)00213-5](https://doi.org/10.1016/S0010-4485(01)00213-5).
- Belaud, V., S. Valette, G. Stremdoerfer, M. Bigerelle, and S. Benayoun. 2015. "Wettability versus Roughness: Multi-Scales Approach." *Tribology International* 82 (PB): 343–49. <https://doi.org/10.1016/j.triboint.2014.07.002>.
- Beng, Nam, Tay Myo Minn, and Sujeet K. Sinha. 2011. "A Tribological Study of SU-8 Micro-Dot Patterns Printed on Si Surface in a Flat-on-Flat Reciprocating Sliding Test." *Tribology Letters* 44 (2): 167–76. <https://doi.org/10.1007/s11249-011-9835-1>.
- Bewilogua, K., G. Bräuer, A. Dietz, J. Gäbler, G. Goch, B. Karpuschewski, and B. Szyszka. 2009. "Surface Technology for Automotive Engineering." *CIRP Annals - Manufacturing Technology* 58 (2): 608–76. <https://doi.org/10.1016/j.cirp.2009.09.001>.

- Bhushan, Bharat, and Eun Kyu Her. 2010. "Fabrication of Superhydrophobic Surfaces with High and Low Adhesion Inspired from Rose Petal." *Langmuir* 26 (11): 8207–17. <https://doi.org/10.1021/la904585j>.
- Bhushan, Bharat, and Michael Nosonovsky. 2003. "Scale Effects in Friction Using Strain Gradient Plasticity and Dislocation-Assisted Sliding (Microslip)." *Acta Materialia* 51 (14): 4331–45. [https://doi.org/10.1016/S1359-6454\(03\)00261-1](https://doi.org/10.1016/S1359-6454(03)00261-1).
- Bico, José, Uwe Thiele, and David Quéré. 2002. "Wetting of Textured Surfaces." *Colloids and Surfaces A: Physicochemical and Engineering Aspects* 206 (1–3): 41–46. [https://doi.org/10.1016/S0927-7757\(02\)00061-4](https://doi.org/10.1016/S0927-7757(02)00061-4).
- Borghini, A., E. Gualtieri, D. Marchetto, L. Moretti, and S. Valeri. 2008. "Tribological Effects of Surface Texturing on Nitriding Steel for High-Performance Engine Applications." *Wear* 265 (7–8): 1046–51. <https://doi.org/10.1016/j.wear.2008.02.011>.
- Braun, Daniel, Christian Greiner, Johannes Schneider, and Peter Gumbsch. 2014. "Efficiency of Laser Surface Texturing in the Reduction of Friction under Mixed Lubrication." *Tribology International* 77: 142–47. <https://doi.org/10.1016/j.triboint.2014.04.012>.
- Bruzzzone, A A G, H L Costa, P M Lonardo, and D A Lucca. 2008. "Advances in Engineered Surfaces for Functional Performance." *CIRP Annals - Manufacturing Technology* 57 (2): 750–69. <https://doi.org/10.1016/j.cirp.2008.09.003>.
- Bulatov, V.P, V.a Krasny, and Y.G Schneider. 1997. "Basics of Machining Methods to Yield Wear- and Fretting-Resistive Surfaces, Having Regular Roughness Patterns." *Wear* 208 (1–2): 132–37. [https://doi.org/10.1016/S0043-1648\(96\)07403-0](https://doi.org/10.1016/S0043-1648(96)07403-0).
- Butt, Hans-Jürgen. Kappl, Michael. 2010. *Surface and Interfacial Forces*. Mainz, Germany: Wiley-VCH.
- Çaydaş, Ulaş, and Ahmet Hasçalik. 2008. "A Study on Surface Roughness in Abrasive Waterjet Machining Process Using Artificial Neural Networks and Regression Analysis Method." *Journal of Materials Processing Technology* 202 (1–3): 574–82. <https://doi.org/10.1016/j.jmatprotec.2007.10.024>.
- Chae, J, S S Park, and T Freiheit. 2006. "Investigation of Micro-Cutting Operations." *International Journal of Machine Tools and Manufacture* 46 (3–4): 313–32. <https://doi.org/10.1016/j.ijmachtools.2005.05.015>.
- Chang, C, Y Liao, G Z Wang, Y R Ma, and R C Fang. 2003. "Crystal Growth Technology." In *Crystal Growth Technology*, 93. Springer-Verlag Berlin Heidelberg New York.
- Chang, L. 1995. "Deterministic Modeling and Numerical Simulation of Lubrication between Rough Surfaces a Review of Recent Developments." *Wear*, 1995;0(0):0 184: 155–60.
- Choudhury, Dipankar, Taposh Roy, Ivan Krupka, Martin Hartl, and Rajshree Mootanah. 2015. "Tribological Investigation of Ultra-High Molecular Weight Polyethylene against Advanced Ceramic Surfaces in Total Hip Joint Replacement." *Proceedings of the Institution of Mechanical Engineers, Part J: Journal of Engineering Tribology* 229 (4): 410–19. <https://doi.org/10.1177/1350650114541106>.
- Coblas, D. G., a. Fatu, a. Maoui, and M. Hajjam. 2014. "Manufacturing Textured Surfaces: State of Art and Recent Developments." *Proceedings of the Institution of Mechanical Engineers, Part J: Journal of Engineering Tribology* 229 (1): 3–29. <https://doi.org/10.1177/1350650114542242>.
- Costa, H. L., and I. M. Hutchings. 2007. "Hydrodynamic Lubrication of Textured Steel Surfaces under Reciprocating Sliding Conditions." *Tribology International* 40 (8): 1227–38. <https://doi.org/10.1016/j.triboint.2007.01.014>.

- Costa, HL, and IM Hutchings. 2015. "Some Innovative Surface Texturing Techniques for Tribological Purposes." *Proceedings of the Institution of Mechanical Engineers, Part J: Journal of Engineering Tribology* 229 (4): 429–48. <https://doi.org/10.1177/1350650114539936>.
- D. A. Lyn, S. Einav, W. Rodi, J.-H. PARK. 2000. "Effect of Impact Angle on Glass Surfaces Eroded by Sand Blasting." *Journal of the European Ceramic Society* 20 (4): 481–88. [https://doi.org/10.1016/S0955-2219\(99\)00140-5](https://doi.org/10.1016/S0955-2219(99)00140-5).
- Deng, T., M. S. Bingley, and M. S A Bradley. 2004. "The Influence of Particle Rotation on the Solid Particle Erosion Rate of Metals." *Wear* 256 (11–12): 1037–49. [https://doi.org/10.1016/S0043-1648\(03\)00536-2](https://doi.org/10.1016/S0043-1648(03)00536-2).
- Denkena, B., J. Kästner, and B. Wang. 2010. "Advanced Microstructures and Its Production through Cutting and Grinding." *CIRP Annals - Manufacturing Technology* 59 (1): 67–72. <https://doi.org/10.1016/j.cirp.2010.03.066>.
- Dimov, Stefan Simeonov, Duc Truong Pham, Atanas Ivanov, Krastimir Borisov Popov, and K. Fansen. 2004. "Micromilling Strategies: Optimization Issues," no. March: 731–36. <https://doi.org/10.1177/095440540421800706>.
- Dobrica, M. B., and M. Fillon. 2009. "About the Validity of Reynolds Equation and Inertia Effects in Textured Sliders of Infinite Width." *Proceedings of the Institution of Mechanical Engineers, Part J: Journal of Engineering Tribology* 223 (1): 69–78. <https://doi.org/10.1243/13506501JET433>.
- Dobrovinskaya Elena R. Leonid A. Lytvynov. Valerian Pishchik. 2009. *Sapphire: Material, Manufacturing, Applications*. Springer Science & Business Media. <https://doi.org/10.1007/978-0-387-85695-7>.
- Dubrujeaud, B., M. Vardavoulias, and M. Jeandin. 1994. "The Role of Porosity in the Dry Sliding Wear of a Sintered Ferrous Alloy." *Wear* 174 (1–2): 155–61. [https://doi.org/10.1016/0043-1648\(94\)90097-3](https://doi.org/10.1016/0043-1648(94)90097-3).
- Dumitru, G., V. Romano, H. P. Weber, S. Pimenov, T. Kononenko, J. Hermann, S. Bruneau, Y. Gerbig, and M. Shupegin. 2003. "Laser Treatment of Tribological DLC Films." *Diamond and Related Materials* 12 (3–7): 1034–40. [https://doi.org/10.1016/S0925-9635\(02\)00372-2](https://doi.org/10.1016/S0925-9635(02)00372-2).
- Ebert, Daniel, and Bharat Bhushan. 2012. "Wear-Resistant Rose Petal-Effect Surfaces with Superhydrophobicity and High Droplet Adhesion Using Hydrophobic and Hydrophilic Nanoparticles." *Journal of Colloid and Interface Science* 384 (1): 182–88. <https://doi.org/10.1016/j.jcis.2012.06.070>.
- Elements, Machine. n.d. "COMPARISON OF REYNOLDS AND NAVIER-STOKES APPROACHES FOR SOLVING ISOTHERMAL EHL LINE CONTACTS," no. 1: 1–4.
- Erbil, H. Yildirim. 2014. "The Debate on the Dependence of Apparent Contact Angles on Drop Contact Area or Three-Phase Contact Line: A Review." *Surface Science Reports* 69 (4): 325–65. <https://doi.org/10.1016/j.surfrep.2014.09.001>.
- Etsion, I., G. Halperin, V. Brizmer, and Y. Kligerman. 2004. "Experimental Investigation of Laser Surface Textured Parallel Thrust Bearings." *Tribology Letters* 17 (2): 295–300. <https://doi.org/10.1023/B:TRIL.0000032467.88800.59>.
- Etsion, I. 2004. "Improving Tribological Performance of Mechanical Components by Laser Surface Texturing." *Tribology Letters* 17 (4): 733–37.
- Etsion, I, and E Sher. 2009. "Improving Fuel Efficiency with Laser Surface Textured Piston Rings." *Tribology International* 42 (4): 542–47. <https://doi.org/10.1016/j.triboint.2008.02.015>.

- Etsion, Izhak. 2004. "Improving Tribological Performance of Mechanical Seals by Laser Surface Texturing." *Tribology Letters* 17.
- Etsion, Izhak. 2005. "State of the Art in Laser Surface Texturing." *Journal of Tribology* 127 (1): 248. <https://doi.org/10.1115/1.1828070>.
- Etsion, Izhak. 2013. "Modeling of Surface Texturing in Hydrodynamic Lubrication." *Friction* 1 (3): 195–209. <https://doi.org/10.1007/s40544-013-0018-y>.
- Fiorini, C., N. Prudhomme, G. De Veyrac, I. Maurin, P. Raimond, and J. M. Nunzi. 2000. "Molecular Migration Mechanism for Laser Induced Surface Relief Grating Formation." *Synthetic Metals* 115 (1): 121–25. [https://doi.org/10.1016/S0379-6779\(00\)00332-5](https://doi.org/10.1016/S0379-6779(00)00332-5).
- Fleischer, J., and J. Kotschenreuther. 2006. "The Manufacturing of Micro Molds by Conventional and Energy-Assisted Processes." *The International Journal of Advanced Manufacturing Technology* 33 (1–2): 75–85. <https://doi.org/10.1007/s00170-006-0596-1>.
- Fletcher, D. I., A. Kapoor, K. Steinhoff, and N. Schuleit. 2000. "Wear Behaviour and Surface Form Evolution of a Novel Titanium Carbide Implanted Surface under Lubricated Conditions." *Proceedings of the Institution of Mechanical Engineers, Part J: Journal of Engineering Tribology* 214 (6): 597–610. <https://doi.org/10.1243/1350650001543449>.
- Fontaine, M., A. Devillez, A. Moufki, and D. Dudzinski. 2007. "Modelling of Cutting Forces in Ball-End Milling with Tool-Surface Inclination. Part I. Influence of Cutting Conditions, Run-out, Ploughing and Inclination Angle." *Journal of Materials Processing Technology* 189 (1–3): 85–96. <https://doi.org/10.1016/j.jmatprotec.2007.01.007>.
- Gadelmawla, E. S., M. M. Koura, T. M. A. Maksoud, I. M. Elewa, and H. H. Soliman. 2002. "Roughness Parameters." *Journal of Materials Processing Technology* 123: 13. [https://doi.org/10.1016/S0924-0136\(02\)00060-2](https://doi.org/10.1016/S0924-0136(02)00060-2).
- Galda, Lidia, Waldemar Koszela, and Pawel Pawlus. 2007. "Surface Geometry of Slide Bearings after Percussive Burnishing." *Tribology International* 40 (10-12 SPEC. ISS.): 1516–25. <https://doi.org/10.1016/j.triboint.2007.01.010>.
- Galda, Lidia, Pawel Pawlus, and Jaroslaw Sep. 2009. "Dimples Shape and Distribution Effect on Characteristics of Stribeck Curve." *Tribology International* 42 (10): 1505–12. <https://doi.org/10.1016/j.triboint.2009.06.001>.
- Gelinck, E.R.M., and D.J. Schipper. 2000. "Calculation of Stribeck Curves for Line Contacts." *Tribology International* 33 (3–4): 175–81. [https://doi.org/10.1016/S0301-679X\(00\)00024-4](https://doi.org/10.1016/S0301-679X(00)00024-4).
- Ghaednia, Hamid, Xianzhang Wang, Swarna Saha, Yang Xu, Aman Sharma, and Robert L. Jackson. 2017. "A Review of Elastic–Plastic Contact Mechanics." *Applied Mechanics Reviews* 69 (6): 060804. <https://doi.org/10.1115/1.4038187>.
- Gopinath, A., and L. Mahadevan. 2011. "Elastohydrodynamics of Wet Bristles, Carpets and Brushes." *Proceedings of the Royal Society A: Mathematical, Physical and Engineering Sciences* 467 (2130): 1665–85. <https://doi.org/10.1098/rspa.2010.0228>.
- Graham, E, C I Park, and S S Park. 2013. "Force Modeling and Applications of Inclined Ball End Milling of Micro-Dimpled Surfaces." *The International Journal of Advanced Manufacturing Technology* 70 (1–4): 689–700. <https://doi.org/10.1007/s00170-013-5310-5>.
- Graham, Eldon, Chaneel I. Park, and Simon S. Park. 2013. "Fabrication of Micro-Dimpled Surfaces through Micro Ball End Milling." *International Journal of Precision Engineering and Manufacturing* 14 (9):

1637–46. <https://doi.org/10.1007/s12541-013-0221-9>.

- Greenwood, James A., and J. H. Tripp. 1970. “The Contact of Two Nominally Flat Rough Surfaces.” *Proceedings of the Institution of Mechanical Engineers* 1–196. <https://doi.org/10.1243/PIME>.
- Greiner, Christian, Tobias Merz, Daniel Braun, Andrea Codrignani, and Franco Magagnato. 2015. “Optimum Dimple Diameter for Friction Reduction with Laser Surface Texturing: The Effect of Velocity Gradient.” *Surface Topography: Metrology and Properties* 3 (4). <https://doi.org/10.1088/2051-672X/3/4/044001>.
- Greiner, Christian, and Michael Schäfer. 2015. “Bio-Inspired Scale-like Surface Textures and Their Tribological Properties.” *Bioinspiration & Biomimetics* 10 (4): 44001. <https://doi.org/10.1088/1748-3190/10/4/044001>.
- Greiner, Christian, Michael Schäfer, Uwe Popp, and Peter Gumbsch. 2014. “Contact Splitting and the Effect of Dimple Depth on Static Friction of Textured Surfaces.” *ACS Applied Materials and Interfaces* 6 (11): 7986–90. <https://doi.org/10.1021/am500879m>.
- Gropper, Daniel, Ling Wang, and Terry J. Harvey. 2016. “Hydrodynamic Lubrication of Textured Surfaces: A Review of Modeling Techniques and Key Findings.” *Tribology International* 94: 509–29. <https://doi.org/10.1016/j.triboint.2015.10.009>.
- Han, Jing, Liang Fang, Jiapeng Sun, and Shirong Ge. 2010. “Hydrodynamic Lubrication of Microdimple Textured Surface Using Three-Dimensional CFD.” *Tribology Transactions* 53 (6): 860–70. <https://doi.org/10.1080/10402004.2010.496070>.
- Han, Jing, Liang Fang, Jiapeng Sun, Yanqing Wang, Shirong Ge, and Hua Zhu. 2011. “Hydrodynamic Lubrication of Surfaces with Asymmetric Microdimple.” *Tribology Transactions* 54 (4): 607–15. <https://doi.org/10.1080/10402004.2011.584364>.
- Heaney, Patrick J, Anirudha V Sumant, Christopher D Torres, Robert W Carpick, and Frank E Pfefferkorn. 2008. “Diamond Coatings for Micro End Mills: Enabling the Dry Machining of Aluminum at the Micro-Scale.” *Diamond and Related Materials* 17 (3): 223–33. <https://doi.org/10.1016/j.diamond.2007.12.009>.
- Henry, Y., J. Bouyer, and M. Fillon. 2014. “An Experimental Analysis of the Hydrodynamic Contribution of Textured Thrust Bearings during Steady-State Operation: A Comparison with the Untextured Parallel Surface Configuration.” *Proceedings of the Institution of Mechanical Engineers, Part J: Journal of Engineering Tribology* 229 (4): 362–75. <https://doi.org/10.1177/1350650114537484>.
- Hertz, Heinrich. 1882. “Über Die Berührung Fester Elastischer Körper (On the Contact of Rigid Elastic Solids).” *Journal Für Die Reine Und Angewandte Mathematik* |, 358.
- Hidrovo, Carlo H., and Douglas P. Hart. 2001. “Emission Reabsorption Laser Induced FLuorescence (ERLIF) Film Thickness Measurement.” *Institute of Physics Publishing* 12:) 467–477. http://www.me.utexas.edu/~hidrovo/papers/ERLIF-film-thickness-measurement_MST_HIDROVO.pdf.
- Holmberg, Kenneth, and Ali Erdemir. 2015. “Global Impact of Friction on Energy Consumption, Economy and Environment.” *FME Transactions* 43 (3): 181–85. <https://doi.org/10.5937/fmet1503181H>.
- Hu, Tianchang, Litian Hu, and Qi Ding. 2012. “The Effect of Laser Surface Texturing on the Tribological Behavior of Ti-6Al-4V.” *Proceedings of the Institution of Mechanical Engineers, Part J: Journal of Engineering Tribology* 226 (10): 854–63. <https://doi.org/10.1177/1350650112450801>.
- Hu, Yuan-Zhong, and Dong Zhu. 2000. “A Full Numerical Solution to the Mixed Lubrication in Point

- Contacts.” *Journal of Tribology* 122 (1): 1. <https://doi.org/10.1115/1.555322>.
- Hutchings, I. M. 2001. *Tribology Friction and Wear of Engineering Materials*. Butterworth Heinemann.
- Ito, H, K Kaneda, T Yuhta, I Nishimura, K Yasuda, and T Matsuno. 2000. “Reduction of Polyethylene Wear by Concave Dimples on the Frictional Surface in Artificial Hip Joints.” *The Journal of Arthroplasty* 15 (3): 332–38. [https://doi.org/10.1016/S0883-5403\(00\)90670-3](https://doi.org/10.1016/S0883-5403(00)90670-3).
- Jain, Rajendra K., Vijay K. Jain, and P. M. Dixit. 1999. “Modeling of Material Removal and Surface Roughness in Abrasive Flow Machining Process.” *International Journal of Machine Tools and Manufacture* 39 (12): 1903–23. [https://doi.org/10.1016/S0890-6955\(99\)00038-3](https://doi.org/10.1016/S0890-6955(99)00038-3).
- Jang, HS, MW Cho, and DS Park. 2008. “Micro Fluidic Channel Machining on Fused Silica Glass Using Powder Blasting.” *Sensors*, 700–710. <https://doi.org/10.3390/s8020700>.
- Jeong-Du Kim and Youn-Hee Kang. 1997. “High-Speed Machining of Aluminium Using Diamond End Mills.” *Int. J. Mnch. Tools Manufact* 37: 1155–65.
- Jung, Yong Chae, and Bharat Bhushan. 2006. “Contact Angle, Adhesion and Friction Properties of Micro- and Nanopatterned Polymers for Superhydrophobicity.” *Nanotechnology* 17: 4970–80. <https://doi.org/10.1088/0957-4484/17/19/033>.
- Kijlstra, J., K. Reihs, and A. Klamt. 2002. “Roughness and Topology of Ultra-Hydrophobic Surfaces.” *Colloids and Surfaces A: Physicochemical and Engineering Aspects* 206 (1–3): 521–29. [https://doi.org/10.1016/S0927-7757\(02\)00089-4](https://doi.org/10.1016/S0927-7757(02)00089-4).
- Kim, D. E., K. H. Cha, I. H. Sung, and J. Bryan. 2002. “Design of Surface Micro-Structures for Friction Control in Micro-Systems Applications.” *CIRP Annals - Manufacturing Technology* 51 (1): 495–98. [https://doi.org/10.1016/S0007-8506\(07\)61569-8](https://doi.org/10.1016/S0007-8506(07)61569-8).
- Kogusu, S, and T Ishimatsu. 2008. “Decoration of Metal Surface by Dimples Using Ball-End Milling Process.” ... , 2008. *ICIT 2008*. http://ieeexplore.ieee.org/xpls/abs_all.jsp?arnumber=4608539.
- Koszela, Waldemar, Andrzej Dzierwa, Lidia Galda, and Pawel Pawlus. 2012. “Experimental Investigation of Oil Pockets Effect on Abrasive Wear Resistance.” *Tribology International* 46 (1): 145–53. <https://doi.org/10.1016/j.triboint.2011.05.001>.
- Kovalchenko, Andriy, Oyelayo Ajayi, Ali Erdemir, George Fenske, and Izhak Etsion. 2004. “The Effect of Laser Texturing of Steel Surfaces and Speed-Load Parameters on the Transition of Lubrication Regime from Boundary to Hydrodynamic.” *Tribology Transactions* 47 (2): 299–307. <https://doi.org/10.1080/05698190490440902>.
- Kovalchenko, Andriy, Oyelayo Ajayi, Ali Erdemir, George Fenske, and Izhak Etsion. 2005. “The Effect of Laser Surface Texturing on Transitions in Lubrication Regimes during Unidirectional Sliding Contact.” *Tribology International* 38 (3): 219–25. <https://doi.org/10.1016/j.triboint.2004.08.004>.
- Křupka, I., and M. Hartl. 2007. “The Effect of Surface Texturing on Thin EHD Lubrication Films.” *Tribology International* 40 (7): 1100–1110. <https://doi.org/10.1016/j.triboint.2006.10.007>.
- Křupka, I., and M. Hartl. 2007. “The Influence of Thin Boundary Films on Real Surface Roughness in Thin Film, Mixed EHD Contact.” *Tribology International* 40 (10–12): 1553–60. <https://doi.org/10.1016/j.triboint.2006.10.008>.
- Křupka, I., R. Poliščuk, and M. Hartl. 2009. “Behavior of Thin Viscous Boundary Films in Lubricated Contacts between Micro-Textured Surfaces.” *Tribology International* 42 (4): 535–41. <https://doi.org/10.1016/j.triboint.2008.03.013>.

- Křupka, I., M. Vrbka, and M. Hartl. 2008. "Effect of Surface Texturing on Mixed Lubricated Non-Conformal Contacts." *Tribology International* 41 (11): 1063–73. <https://doi.org/10.1016/j.triboint.2007.11.016>.
- Kubiak, K. J., M. C.T. Wilson, T. G. Mathia, and Ph Carval. 2011. "Wettability versus Roughness of Engineering Surfaces." *Wear* 271 (3–4): 523–28. <https://doi.org/10.1016/j.wear.2010.03.029>.
- Kurniawan, Rendi, Gandjar Kiswanto, and Tae Jo Ko. 2017. "Surface Roughness of Two-Frequency Elliptical Vibration Texturing (TFEVT) Method for Micro-Dimple Pattern Process." *International Journal of Machine Tools and Manufacture* 116 (January): 77–95. <https://doi.org/10.1016/j.ijmachtools.2016.12.011>.
- Leblond, H, R Barille, S Ahmadi-Kandjani, J-M Nunzi, E Ortyl, and S Kucharski. 2009. "Spontaneous Formation of Optically Induced Surface Relief Gratings." *Journal of Physics B: Atomic, Molecular and Optical Physics* 42 (20): 205401. <https://doi.org/10.1088/0953-4075/42/20/205401>.
- Leeuwen, Harry van. 2010. "The Determination of the Pressure- Viscosity Coefficient of Two Traction Oils Using Film Thickness Measurements Harry van Leeuwen." *Lubrication*.
- Li, Jianliang, Dangsheng Xiong, Jihui Dai, Zhongjia Huang, and Rajnesh Tyagi. 2010. "Effect of Surface Laser Texture on Friction Properties of Nickel-Based Composite." *Tribology International* 43 (5–6): 1193–99. <https://doi.org/10.1016/j.triboint.2009.12.044>.
- Liew, K. W., C. K. Kok, and M. N. Ervina Efzan. 2016. "Effect of EDM Dimple Geometry on Friction Reduction under Boundary and Mixed Lubrication." *Tribology International* 101: 1–9. <https://doi.org/10.1016/j.triboint.2016.03.029>.
- Lim, S.C., and M.F. Ashby. 1987. "Overview No. 55 Wear-Mechanism Maps." *Acta Metallurgica* 35 (1): 1–24. [https://doi.org/10.1016/0001-6160\(87\)90209-4](https://doi.org/10.1016/0001-6160(87)90209-4).
- Lu, Xiaobin, and M. M. Khonsari. 2007. "An Experimental Investigation of Dimple Effect on the Stribeck Curve of Journal Bearings." *Tribology Letters* 27 (2): 169–76. <https://doi.org/10.1007/s11249-007-9217-x>.
- Lundberg, Jan. 1995. "Influence of Surface Roughness on Normal-Sliding Lubrication." *Tribology International* 28 (5): 317–22. [https://doi.org/10.1016/0301-679X\(94\)00003-9](https://doi.org/10.1016/0301-679X(94)00003-9).
- Malekian, Mohammad, Simon S. Park, and Martin B.G. Jun. 2009. "Modeling of Dynamic Micro-Milling Cutting Forces." *International Journal of Machine Tools and Manufacture* 49 (7–8): 586–98. <https://doi.org/10.1016/j.ijmachtools.2009.02.006>.
- Mandal, D., B. K. Dutta, and S. C. Panigrahi. 2004. "Wear and Friction Behavior of Stir Cast Aluminium-Base Short Steel Fiber Reinforced Composites." *Wear* 257 (7–8): 654–64. <https://doi.org/10.1016/j.wear.2004.02.006>.
- Mansot, J.L., Y. Bercion, L. Romana, and J.M. Martin. 2009. "Nanolubrication." *Brazilian Journal of Physics* 39 (1a): 186–97. <https://doi.org/10.1590/S0103-97332009000200011>.
- Matsumura, Takashi, and Satoru Takahashi. 2011. "Machining of Micro Dimples in Milling for Functional Surfaces." In *The 14th Int. ESAFORM Conference on Material Forming*, 567–72.
- Meng, Fanming, Rui Zhou, Tiffany Davis, Jian Cao, Q. Jane Wang, Diann Hua, and Jordan Liu. 2010. "Study on Effect of Dimples on Friction of Parallel Surfaces under Different Sliding Conditions." *Applied Surface Science* 256: 2863–75. <https://doi.org/10.1016/j.apsusc.2009.11.041>.
- Mourier, L., D. Mazuyer, a.a. Lubrecht, and C. Donnet. 2006. "Transient Increase of Film Thickness in

- Micro-Textured EHL Contacts.” *Tribology International* 39 (12): 1745–56.
<https://doi.org/10.1016/j.triboint.2006.02.037>.
- Mukaida, Mao, and Jiwang Yan. 2017. “Ductile Machining of Single-Crystal Silicon for Microlens Arrays by Ultraprecision Diamond Turning Using a Slow Tool Servo.” *International Journal of Machine Tools and Manufacture* 115 (November 2016): 2–14.
<https://doi.org/10.1016/j.ijmachtools.2016.11.004>.
- Myant, Connor, Mark Fowell, Hugh a. Spikes, and Jason R. Stokes. 2010. “An Investigation of Lubricant Film Thickness in Sliding Compliant Contacts.” *Tribology Transactions* 53 (5): 684–94.
<https://doi.org/10.1080/10402001003693109>.
- Nakada, Masahiko. 1994. “Trends in Engine Technology and Tribology.” *Tribology International* 27 (1): 3–8. [https://doi.org/10.1016/0301-679X\(94\)90056-6](https://doi.org/10.1016/0301-679X(94)90056-6).
- Nakajima, Akira, Kouki Abe, Kazuhito Hashimoto, and Toshiya Watanabe. 2000. “Preparation of Hard Super-Hydrophobic Films with Visible Light Transmission.” *Thin Solid Films* 376 (1–2): 140–43.
[https://doi.org/10.1016/S0040-6090\(00\)01417-6](https://doi.org/10.1016/S0040-6090(00)01417-6).
- Nakano, Miki, Atsuko Korenaga, Atsushi Korenaga, Koji Miyake, Takashi Murakami, Yasuhisa Ando, Hatsuhiko Usami, and Shinya Sasaki. 2007. “Applying Micro-Texture to Cast Iron Surfaces to Reduce the Friction Coefficient under Lubricated Conditions.” *Tribology Letters* 28 (2): 131–37.
<https://doi.org/10.1007/s11249-007-9257-2>.
- Nakano, Miki, Atsuko Korenaga, Atsushi Korenaga, Koji Miyake, Takashi Murakami, Yasuhisa Ando, Hatsuhiko Usami, and Shinya Sasaki. 2007. “Applying Micro-Texture to Cast Iron Surfaces to Reduce the Friction Coefficient Under Lubricated Conditions.” *Tribology Letters* 28 (2): 131–37.
<https://doi.org/10.1007/s11249-007-9257-2>.
- Nam P. Suh, Mohsen Mosleh, Phillip S. Howard. 1994. “Control of Friction.” *Wear* 175: 151–58.
<https://doi.org/10.1103/PhysRevLett.90.094301>.
- Nosonovsky, Michael, and Bharat Bhushan. 2006. “Wetting of Rough Three-Dimensional Superhydrophobic Surfaces.” *Microsystem Technologies* 12 (3): 273–81.
<https://doi.org/10.1007/s00542-005-0067-x>.
- Nosonovsky, Michael, and Bharat Bhushan. 2007. “Hierarchical Roughness Optimization for Biomimetic Superhydrophobic Surfaces.” *Ultramicroscopy* 107 (10–11): 969–79.
<https://doi.org/10.1016/j.ultramic.2007.04.011>.
- Nowell, D., and D. A. Hills. 1990. “Crack Initiation Criteria in Fretting Fatigue.” *Wear* 136 (2): 329–43.
[https://doi.org/10.1016/0043-1648\(90\)90155-4](https://doi.org/10.1016/0043-1648(90)90155-4).
- Ogawa, H, S Sasaki, A Korenaga, K Miyake, M Nakano, and T Murakami. 2010. “Effects of Surface Texture Size on the Tribological Properties of Slideways” 224: 885–90.
<https://doi.org/10.1243/13506501JET735>.
- Ogletree, D. F., Robert W Carpick, and M. Salmeron. 1996. “Calibration of Frictional Forces in Atomic Force Microscopy.” *Review of Scientific Instruments* 67 (1996): 3298.
<https://doi.org/10.1063/1.1147411>.
- Ohue, Yuji, and Hideki Tanaka. 2013. “Effect of Surface Texturing on Lubricating Condition under Point Contact Using Numerical Analysis.” *Engineering* 5 (April): 379–85.
<https://doi.org/10.4236/eng.2013.54050>.
- Oka, Y. I., K. Okamura, and T. Yoshida. 2005. “Practical Estimation of Erosion Damage Caused by Solid

- Particle Impact: Part 1: Effects of Impact Parameters on a Predictive Equation.” *Wear* 259 (1–6): 95–101. <https://doi.org/10.1016/j.wear.2005.01.039>.
- Pang, Minghua, Xiaojun Liu, and Kun Liu. 2017. “Effect of Wettability on the Friction of a Laser-Textured Cemented Carbide Surface in Dilute Cutting Fluid.” *Advances in Mechanical Engineering* 9 (12): 1–9. <https://doi.org/10.1177/1687814017738154>.
- Park, Dong Sam, Myeong-Woo Cho, and Honghee Lee. 2004. “Effects of the Impact Angle Variations on the Erosion Rate of Glass in Powder Blasting Process.” *The International Journal of Advanced Manufacturing Technology* 23 (5–6): 444–50. <https://doi.org/10.1007/s00170-003-1724-9>.
- Park, Jung-ho, Joo-ho Moon, Hyun-jung Shin, Dake Wang, and Min-seo Park. 2006. “Direct-Write Fabrication of Colloidal Photonic Crystal Microarrays by Ink-Jet Printing.” *Journal of Colloid and Interface Science* 298 (2): 713–19. <https://doi.org/10.1016/j.jcis.2006.01.031>.
- Parreira, J. G., C. A. Gallo, and H. L. Costa. 2012. “New Advances on Maskless Electrochemical Texturing (MECT) for Tribological Purposes.” *Surface and Coatings Technology* 212: 1–13. <https://doi.org/10.1016/j.surfcoat.2012.08.043>.
- Pawlak, Z., W. Urbaniak, and A. Oloyede. 2011. “The Relationship between Friction and Wettability in Aqueous Environment.” *Wear* 271 (9–10): 1745–49. <https://doi.org/10.1016/j.wear.2010.12.084>.
- Pawlus, Pawel, Lidia Galda, Andrzej Dzierwa, and Waldemar Koszela. 2009. “Abrasive Wear Resistance of Textured Steel Rings.” *Wear* 267 (11): 1873–82. <https://doi.org/10.1016/j.wear.2009.03.003>.
- Peiran, Yang, and Wen Shizhu. 1990. “A Generalized Reynolds Equation Based on Non-Newtonian Flow in Lubrication Mechanics” 6 (4).
- Pettersson, Ulrika, and Staffan Jacobson. 2003. “Influence of Surface Texture on Boundary Lubricated Sliding Contacts.” *Tribology International* 36 (11): 857–64. [https://doi.org/10.1016/S0301-679X\(03\)00104-X](https://doi.org/10.1016/S0301-679X(03)00104-X).
- Podgornik, B., L. M. Vilhena, M. Sedlaček, Z. Rek, and I. Žun. 2012. “Effectiveness and Design of Surface Texturing for Different Lubrication Regimes.” *Meccanica* 47 (7): 1613–22. <https://doi.org/10.1007/s11012-012-9540-7>.
- Pratap, Tej, and Karali Patra. 2016. “Fabrication and Surface Characterization of Tool Based Micro-Dimple Texture on Ti-6Al-4V for Biomedical Implants.” *Proceedings of 6th International & 27th All India Manufacturing Technology, Design and Research Conference (AIMTDR-2016)*, no. December: 2050–54.
- Pratap, Tej, and Karali Patra. 2018. “Micro Ball-End Milling—an Emerging Manufacturing Technology for Micro-Feature Patterns.” *International Journal of Advanced Manufacturing Technology* 94 (5–8): 2821–45. <https://doi.org/10.1007/s00170-017-1064-9>.
- Priest, M, and C M Taylor. 2000. “Automobile Engine Tribology—Approaching the Surface.” *Wear* 241 (2): 193–203. [https://doi.org/http://dx.doi.org/10.1016/S0043-1648\(00\)00375-6](https://doi.org/http://dx.doi.org/10.1016/S0043-1648(00)00375-6).
- Prina Mello, A., M. A. Bari, and P. J. Prendergast. 2002. “A Comparison of Excimer Laser Etching and Dry Etching Process for Surface Fabrication of Biomaterials.” *Journal of Materials Processing Technology* 124 (3): 284–92. [https://doi.org/10.1016/S0924-0136\(02\)00198-X](https://doi.org/10.1016/S0924-0136(02)00198-X).
- Profito, Francisco J, Demetrio C Zachariadis, and Eduardo Tomanik. 2011. “One Dimensional Mixed Lubrication Regime Model for Textured Piston Rings.”
- Prófito, Francisco José. 2010. “Modelagem Unidimensional Do Regime Misto De Lubrificação Aplicada a

Superfícies Texturizadas.”

- Qiu, Y., and M. M. Khonsari. 2011. “Experimental Investigation of Tribological Performance of Laser Textured Stainless Steel Rings.” *Tribology International* 44 (5): 635–44. <https://doi.org/10.1016/j.triboint.2011.01.003>.
- Ramesh, Ashwin, Wasim Akram, Surya P. Mishra, Andrew H. Cannon, Andreas a. Polycarpou, and William P. King. 2013. “Friction Characteristics of Microtextured Surfaces under Mixed and Hydrodynamic Lubrication.” *Tribology International* 57: 170–76. <https://doi.org/10.1016/j.triboint.2012.07.020>.
- Resendiz, Jesus, Philip Egberts, and Simon S. Park. 2018. “Tribological Behaviour of Multi-Scaled Patterned Surfaces Machined through Inclined End Milling and Micro Shot Blasting.” *Tribology Letters* 0 (0): under review. <https://doi.org/10.1007/s11249-018-1086-y>.
- Resendiz, Jesus, Eldon Graham, Philip Egberts, and Simon S Park. 2015. “Tribology International Directional Friction Surfaces through Asymmetrically Shaped Dimpled Surfaces Patterned Using Inclined Fl at End Milling” 91: 67–73.
- Ronen, Aviram, Izhak Etsion, and Yuri Kligerman. 2001. “Friction-Reducing Surface-Texturing in Reciprocating Automotive Components.” *Tribology Transactions* 44 (3): 359–66. <https://doi.org/10.1080/10402000108982468>.
- Ruff, A.W., and S.M. Wiederhorn. 1979. “Erosion By Solid Particle Impact.” *Treaties of Materials Science and Technology* 16.
- Rupert, Timothy J., and Christopher A. Schuh. 2010. “Sliding Wear of Nanocrystalline Ni-W: Structural Evolution and the Apparent Breakdown of Archard Scaling.” *Acta Materialia* 58 (12): 4137–48. <https://doi.org/10.1016/j.actamat.2010.04.005>.
- Ryk, G., and I. Etsion. 2006. “Testing Piston Rings with Partial Laser Surface Texturing for Friction Reduction.” *Wear* 261 (7–8): 792–96. <https://doi.org/10.1016/j.wear.2006.01.031>.
- Ryk, G., Y. Kligerman, and I. Etsion. 2002. “Experimental Investigation of Laser Surface Texturing for Reciprocating Automotive Components.” *Tribology Transactions* 45 (4): 444–49. <https://doi.org/10.1080/10402000208982572>.
- Sahin, Mumin, Cem S. Çetinarslan, and H. Erol Akata. 2007. “Effect of Surface Roughness on Friction Coefficients during Upsetting Processes for Different Materials.” *Materials & Design* 28 (2): 633–40. <https://doi.org/10.1016/j.matdes.2005.07.019>.
- Sahlin, F, S B Glavatskih, T Almqvist, and R Larsson. 2005. “Two-Dimensional CFD-Analysis of Micro-Patterned Surfaces in Hydrodynamic Lubrication.” *Journal of Tribology-Transactions of the Asme* 127 (1): 96–102. <https://doi.org/Doi 10.1115/1.1828067>.
- Samuel Cupillard, Michael J. Cervantes, Sergei Glavatskih. 2008. “Pressure Build-up Mechanism in a Textured Inlet of Hydrodynamic Contact.” *Journal of Tribology* 130 (2). <https://doi.org/10.1115/1.2805426>.
- Scaraggi, Michele, Giuseppe Carbone, Bo N J Persson, and Daniele Dini. 2011. “Lubrication in Soft Rough Contacts: A Novel Homogenized Approach. Part i - Theory.” *Soft Matter* 7 (21): 10395–406. <https://doi.org/10.1039/c1sm05128h>.
- Scaraggi, Michele, Francesco P. Mezzapesa, Giuseppe Carbone, Antonio Ancona, Donato Sorgente, and Pietro Mario Lugarà. 2014. “Minimize Friction of Lubricated Laser-Microtextured-Surfaces by Tuning Microholes Depth.” *Tribology International* 75: 123–27.

<https://doi.org/10.1016/j.triboint.2014.03.014>.

- Scaraggi, Michele, Francesco P. Mezzapesa, Giuseppe Carbone, Antonio Ancona, and Luigi Tricarico. 2013. "Friction Properties of Lubricated Laser-Micro-Textured-Surfaces: An Experimental Study from Boundary to Hydrodynamic Lubrication." *Tribology Letters* 49 (1): 117–25. <https://doi.org/10.1007/s1124901200452>.
- Schneider, Yu G. 1984. "Formation of Surfaces with Uniform Micropatterns on Precision Machine and Instruments Parts." *Precision Engineering* 6 (4): 219–25. [https://doi.org/10.1016/0141-6359\(84\)90007-2](https://doi.org/10.1016/0141-6359(84)90007-2).
- Schweikart, Alexandra, Anne Horn, Alexander Böker, and Andreas Fery. 2010. "Controlled Wrinkling as a Novel Method for the Fabrication of Patterned Surfaces." *Advances in Polymer Science* 227 (1): 75–99. <https://doi.org/10.1007/12-2009-22>.
- Sedlaček, Marko, Peter Gregorčič, and Bojan Podgornik. 2017. "Use of the Roughness Parameters Ssk and Skuto Control Friction—A Method for Designing Surface Texturing." *Tribology Transactions* 60 (2): 260–66. <https://doi.org/10.1080/10402004.2016.1159358>.
- Stribeck, Richard. 1902. "Die Wesentlichen Eigenschaften Der Gleit- Und Rollenlager." *Zeitschrift Des Vereins Deutscher Ingenieure* 36: 1341–48.
- Tang, Wei, Yuankai Zhou, Hua Zhu, and Haifeng Yang. 2013. "The Effect of Surface Texturing on Reducing the Friction and Wear of Steel under Lubricated Sliding Contact." *Applied Surface Science* 273: 199–204. <https://doi.org/10.1016/j.apsusc.2013.02.013>.
- Tay, Nam Beng, Myo Minn, and Sujeet K. Sinha. 2011. "Polymer Jet Printing of SU-8 Micro-Dot Patterns on Si Surface: Optimization of Tribological Properties." *Tribology Letters* 42 (2): 215–22. <https://doi.org/10.1007/s11249-011-9765-y>.
- "Technical Data/Properties Synthetic Sapphire & Ruby." n.d. Accessed May 27, 2015. <http://www.mosercompany.com/saphirespec.htm>.
- Tønder, K. 1996. "Dynamics of Rough Slider Bearings: Effects of One-Sided Roughness/Waviness." *Tribology International* 29 (2): 117–22. [https://doi.org/10.1016/0301-679X\(95\)00095-L](https://doi.org/10.1016/0301-679X(95)00095-L).
- Tønder, K. 2004. "Hydrodynamic Effects of Tailored Inlet Roughnesses: Extended Theory." *Tribology International* 37 (2): 137–42. [https://doi.org/10.1016/S0301-679X\(03\)00043-4](https://doi.org/10.1016/S0301-679X(03)00043-4).
- Totten, George E. 2012. *Handbook of Hydraulic Fluid Technology*. 2nd ed. CRC.
- Uehara, Y., M. Wakuda, Y. Yamauchi, S. Kanzaki, and S. Sakaguchi. 2004. "Tribological Properties of Dimpled Silicon Nitride under Oil Lubrication." *Journal of the European Ceramic Society* 24 (2): 369–73. [https://doi.org/10.1016/S0955-2219\(03\)00220-6](https://doi.org/10.1016/S0955-2219(03)00220-6).
- Venner, C.H., and A.A. Lubrecht. 2000. *Multilevel Methods in Lubrication*. Edited by D. Dowson. 1st ed. Elsevier.
- Vilhena, L. M., B. Podgornik, J. Vižintin, and J. Možina. 2011. "Influence of Texturing Parameters and Contact Conditions on Tribological Behaviour of Laser Textured Surfaces." *Meccanica* 46 (3): 567–75. <https://doi.org/10.1007/s11012-010-9316-x>.
- Vilhena, L. M., M. Sedlaček, B. Podgornik, J. Vižintin, A. Babnik, and J. Možina. 2009. "Surface Texturing by Pulsed Nd:YAG Laser." *Tribology International* 42 (10): 1496–1504. <https://doi.org/10.1016/j.triboint.2009.06.003>.
- Vite-Torres, M., J. R. Laguna-Camacho, R. E. Baldenebro-Castillo, E. A. Gallardo-Hernández, E. E. Vera-

- Cárdenas, and J. Vite-Torres. 2013. "Study of Solid Particle Erosion on AISI 420 Stainless Steel Using Angular Silicon Carbide and Steel Round Grit Particles." *Wear* 301 (1–2): 383–89. <https://doi.org/10.1016/j.wear.2013.01.071>.
- Vladescu, Sorin Cristian, Andrew V. Olver, Ian G. Pegg, and Tom Reddyhoff. 2015. "The Effects of Surface Texture in Reciprocating Contacts - An Experimental Study." *Tribology International* 82 (PA): 28–42. <https://doi.org/10.1016/j.triboint.2014.09.015>.
- Wakuda, Manabu, Yukihiko Yamauchi, Shuzo Kanzaki, and Yoshiteru Yasuda. 2003. "Effect of Surface Texturing on Friction Reduction between Ceramic and Steel Materials under Lubricated Sliding Contact." *Wear* 254 (3–4): 356–63. [https://doi.org/10.1016/S0043-1648\(03\)00004-8](https://doi.org/10.1016/S0043-1648(03)00004-8).
- Wang, Q. Jane, Dong Zhu, Raosheng Zhou, and Fukuo Hashimoto. 2008. "Investigating the Effect of Surface Finish on Mixed EHL in Rolling and Rolling-Sliding Contacts." *Tribology Transactions* 51 (6): 748–61. <https://doi.org/10.1080/10402000801888937>.
- Wang, Xiaolei, Koji Kato, and Koshi Adachi. 2002. "The Lubrication Effect of Micro-Pits on Parallel Sliding Faces of SiC in Water." *Tribology Transactions* 45 (3): 294–301. <https://doi.org/10.1080/10402000208982552>.
- Wang, Xiaolei, Koji Kato, Koshi Adachi, and Kohji Aizawa. 2003. "Loads Carrying Capacity Map for the Surface Texture Design of SiC Thrust Bearing Sliding in Water." *Tribology International* 36 (3): 189–97. [https://doi.org/10.1016/S0301-679X\(02\)00145-7](https://doi.org/10.1016/S0301-679X(02)00145-7).
- Wang, Xiaolei, Koji Kato, Koshi Adachi, and Kohji Aizawa. 2001. "The Effect of Laser Texturing of SiC Surface on the Critical Load for the Transition of Water Lubrication Mode from Hydrodynamic to Mixed." *Tribology International* 34 (10): 703–11. [https://doi.org/10.1016/S0301-679X\(01\)00063-9](https://doi.org/10.1016/S0301-679X(01)00063-9).
- Wang, Xiaolei, Wei Liu, Fei Zhou, and Di Zhu. 2009. "Preliminary Investigation of the Effect of Dimple Size on Friction in Line Contacts." *Tribology International* 42 (7): 1118–23. <https://doi.org/10.1016/j.triboint.2009.03.012>.
- Wang, Yumo, Charles Dhong, and Joelle Frechette. 2015. "Out-of-Contact Elastohydrodynamic Deformation Due to Lubrication Forces." *Physical Review Letters* 115 (24): 1–5. <https://doi.org/10.1103/PhysRevLett.115.248302>.
- Waterhouse, R. B., and A. J. Trowsdale. 1992. "Residual Stress and Surface Roughness in Fretting Fatigue." *Journal of Physics D: Applied Physics* 25 (1): A236–37. <https://doi.org/10.1088/0022-3727/25/1A/036>.
- Xing, Youqiang, Jianxin Deng, Ze Wu, and Hongwei Cheng. 2013. "Effect of Regular Surface Textures Generated by Laser on Tribological Behavior of Si₃N₄/TiC Ceramic." *Applied Surface Science* 265: 823–32. <https://doi.org/10.1016/j.apsusc.2012.11.127>.
- Yan, Dongsheng, Ningsong Qu, Hansong Li, and Xiaolei Wang. 2010. "Significance of Dimple Parameters on the Friction of Sliding Surfaces Investigated by Orthogonal Experiments." *Tribology Transactions* 53 (5): 703–12. <https://doi.org/10.1080/10402001003728889>.
- Yan, Jiwang, Zhiyu Zhang, Tsunemoto Kuriyagawa, and Hidenobu Gonda. 2010. "Fabricating Micro-Structured Surface by Using Single-Crystalline Diamond Endmill." *The International Journal of Advanced Manufacturing Technology* 51 (9–12): 957–64. <https://doi.org/10.1007/s00170-010-2695-2>.
- Yong, Hu, and Raj Balendra. 2009. "CFD Analysis on the Lubrication Behaviours of Journal Bearing with Dimples." *2009 IEEE International Conference on Mechatronics and Automation, ICMA 2009*, 1279–84. <https://doi.org/10.1109/ICMA.2009.5246697>.

- Yu, H., H. Deng, W. Huang, and X. Wang. 2011. "The Effect of Dimple Shapes on Friction of Parallel Surfaces." *Proceedings of the Institution of Mechanical Engineers, Part J: Journal of Engineering Tribology* 225: 693–703. <https://doi.org/10.1177/1350650111406045>.
- Yu, Haiwu, Xiaolei Wang, and Fei Zhou. 2010. "Geometric Shape Effects of Surface Texture on the Generation of Hydrodynamic Pressure Between Conformal Contacting Surfaces." *Tribology Letters* 37 (2): 123–30. <https://doi.org/10.1007/s11249-009-9497-4>.
- Yu, X. Q., S. He, and R. L. Cai. 2002. "Frictional Characteristics of Mechanical Seals with a Laser-Textured Seal Face." *Journal of Materials Processing Technology* 129 (1–3): 463–66. [https://doi.org/10.1016/S0924-0136\(02\)00611-8](https://doi.org/10.1016/S0924-0136(02)00611-8).
- Yuan, Z J, M Zhou, and S Dong. 1996. "Effect of Diamond Tool Sharpness on Minimum Cutting Thckness and Cutting Surface," no. 4. [https://doi.org/10.1016/S0924-0136\(96\)02429-6](https://doi.org/10.1016/S0924-0136(96)02429-6).
- Zhang, Bo, Wei Huang, Jingqiu Wang, and Xiaolei Wang. 2013. "Comparison of the Effects of Surface Texture on the Surfaces of Steel and UHMWPE." *Tribology International* 65: 138–45. <https://doi.org/10.1016/j.triboint.2013.01.004>.
- Zhang, H., D. Y. Zhang, M. Hua, G. N. Dong, and K. S. Chin. 2014. "A Study on the Tribological Behavior of Surface Texturing on Babbitt Alloy under Mixed or Starved Lubrication." *Tribology Letters* 56 (2): 305–15. <https://doi.org/10.1007/s11249-014-0410-4>.
- Zhang, Jinyu, and Yonggang Meng. 2012. "Direct Observation of Cavitation Phenomenon and Hydrodynamic Lubrication Analysis of Textured Surfaces." *Tribology Letters* 46 (2): 147–58. <https://doi.org/10.1007/s11249-012-9935-6>.
- Zhang, Yuanyuan, Huaiju Liu, Caichao Zhu, Mingyong Liu, and Chaosheng Song. 2016. "Oil Film Stiffness and Damping in an Elastohydrodynamic Lubrication Line Contact-Vibration." *Journal of Mechanical Science and Technology* 30 (7): 3031–39. <https://doi.org/10.1007/s12206-016-0611-x>.
- Zhang, Z. M., Q. An, W. J. Zhang, Q. Yang, Y. J. Tang, and X. B. Chen. 2011. "Modeling of Directional Friction on a Fully Lubricated Surface with Regular Anisotropic Asperities." *Meccanica* 46 (3): 535–45. <https://doi.org/10.1007/s11012-010-9303-2>.
- Zhou, Changjiang, and Zeliang Xiao. 2018. "Stiffness and Damping Models for the Oil Film in Line Contact Elastohydrodynamic Lubrication and Applications in the Gear Drive." *Applied Mathematical Modelling* 61: 634–49. <https://doi.org/10.1016/j.apm.2018.05.012>.
- Zhu, Dong, and Yuan-Zhong Hu. 2001. "A Computer Program Package for the Prediction of EHL and Mixed Lubrication Characteristics, Friction, Subsurface Stresses and Flash Temperatures Based on Measured 3-D Surface Roughness." *Tribology Transactions* 44 (3): 383–90. <https://doi.org/10.1080/10402000108982471>.

LIST OF PUBLICATIONS

Journal papers

- 1- **Resendiz, J.**, Egberts, P. and Park, S. Tribological Behaviour of Multi-Scaled Patterned Surfaces Machined through Inclined End Milling and Micro Shot Blasting. *Tribology Letters*. (2018) 66:132.
- 2- Wong, D., **Resendiz, J.**, Egberts, P. and Park, S. Electrospinning of Composite Microbeads for Tribological Improvements. *Journal of Manufacturing Processes*. 34 (2018) 264–273.
- 3- **Resendiz, J.**, Graham, E., Egberts, P. and Park, S. Directional Friction Surfaces through Asymmetrically Shaped Dimpled Surfaces Patterned Using Inclined Flat End Milling. *Tribology International*. 91 (2015) 67–73.

Conference Papers

- 1- Wong, D., **Resendiz, J.**, Egberts, P. and Park, S. Reduction of Friction Using Electrospun Polymer Composite Microbeads Emulsified in Mineral Oil. 45th SME North American Manufacturing Research Conference, NAMRC 45, LA, USA. *Procedia Manufacturing* 10 (2017) 339 – 350.
- 2- Wei, Y., **Resendiz, J.**, Allen, S., and Park, S. Investigation of Effects of Micro Textured Sapphire Tool in Turning Operations. 11th International Conference on Micro-Manufacturing, ICOMM. Orange County, California, USA, March 2016.